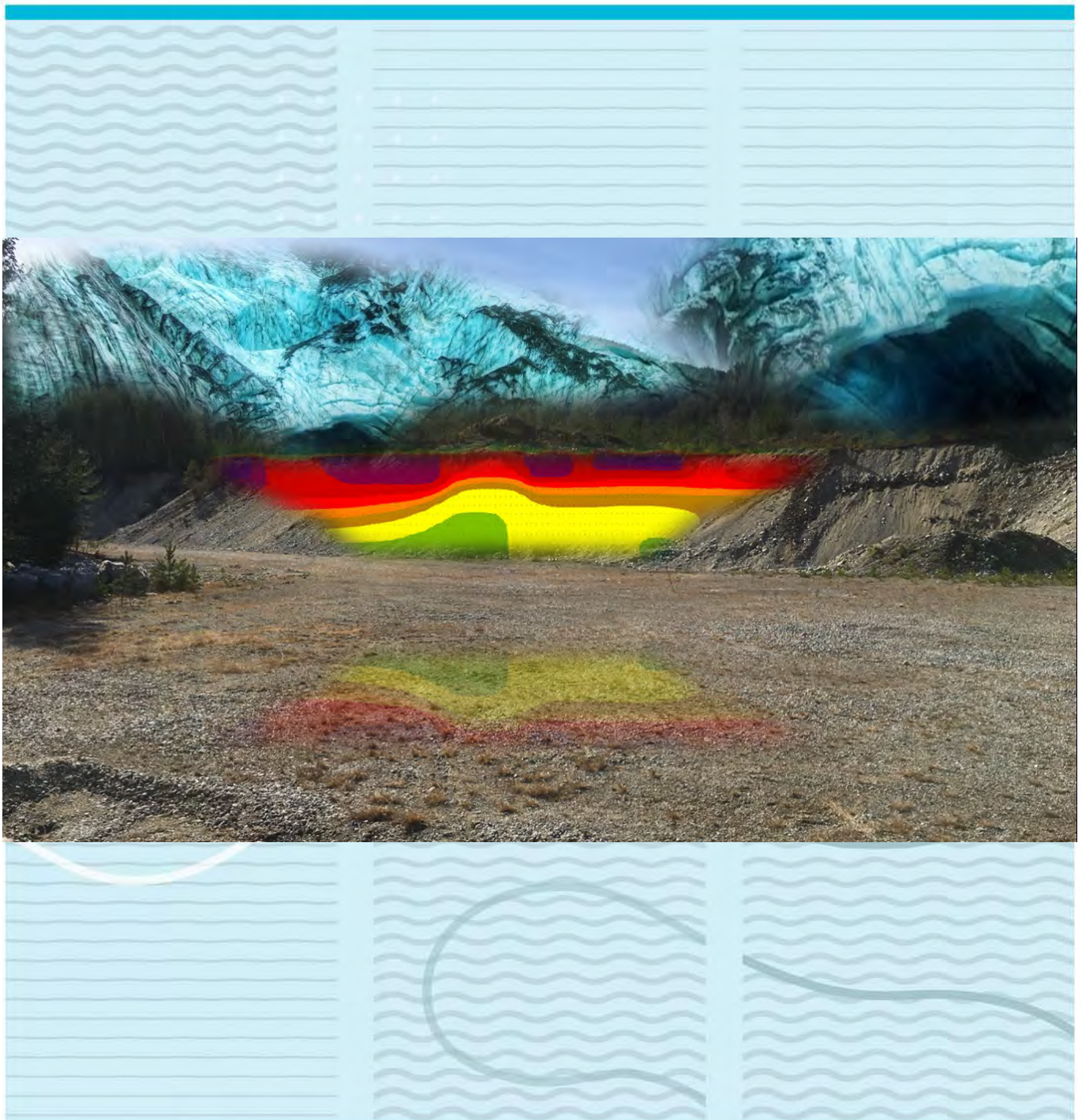Viktor Lavik

Subsurface mapping of Øverbømoen and locating optimal aquifers for drinking water supply

A hydrogeological survey using geophysical methods

This thesis is worth 60 study points

Sammendrag

Denne masteroppgaven undersøkte potensielle akviferer i forhold til drikkevannforsyning ved Øverbømoen i Bø kommune. Øverbømoen er del av en glasifluvial delta-avsetning, hvilket anses å være en god kilde til grunnvann. Det ble derfor antydet at studieområdet ville inneholde akviferer med egnede forhold når det gjelder drikkevannstilførsel. Undergrunnen ble kartlagt ved hjelp av elektrisk resistivitetstomografi (ERT), georadar (GPR) og sondeboring. De innsamlede dataene fra de forskjellige metodene ble koblet sammen og sammenlignet med hverandre, og med tidligere forskningsdata. Resultatene fremstilt av de forskjellige metodene hadde en verifiserende effekt på hverandre og forbedret dermed tolkningsprosessen. Basert på tolkningene ble fire profiler funnet potensielt egnet i forhold til drikkevannsforsyning.

Abstract

This master thesis investigated potential aquifers in terms of drinking water supply at Øverbømoen in Bø municipality. Øverbømoen is part of a glaciofluvial delta deposit, which is considered a good source of groundwater. Hence, it was hypothesized that the study area would contain aquifers with suitable conditions in terms of drinking water supply. The subsurface was mapped using Electrical Resistivity Tomography (ERT), Ground Penetrating Radar (GPR) and probe drilling. The acquired data from the different methods was connected and compared with each other, and with previous research data. The results produced by the different methods had a verifying effect on each other, and thus enhanced the interpretation process. Based on the interpretations, four profiles were found to contain conditions potentially suitable for drinking water supply.

Contents

.

Foreword

Water is what makes planet earth unique and is the reason why our planet is teeming with life. When I observe communities that must endure horrifying conditions in terms of water supply and -quality, I realize how important the field of water science is. Hydrogeology is an exciting discipline where no project is equal. Nobody can know exactly what occurs under the surface, and thus, every fieldwork feels like a treasure hunt.

What this thesis taught me more than anything is the value of teamwork. The fieldwork was demanding, and would have been practically impossible without help from my companions. It was a rough period in November, when we discovered that the first four measurements were biased due to incorrect wiring. They all had to be redone, and going from "comfortably on schedule" to "hurry up, winter is coming" was not a pleasant feeling.

Here I must take time to express an enormous gratitude to my main companion, Jonas Dahl Torp, who was not discouraged by the unexpected challenges and sincerely helped me back on my feet. With a developed routine and efficiency, we managed to correct the error and conduct all the fieldwork within a surprisingly short time.

I would like to express a warm gratitude towards all my companions; Jonas Dahl Torp, Jonas Haugen, Frode Bergan & Tom Aage Aarnes for assisting me in the field. This thesis is fundamentally built on your invaluable efforts. A big thanks to Rasmus Arvidson for instructing me in 2D-resistivity field methods. Thanks also to Svenja Doreen for a much-appreciated proofreading.

I wish to thank my close supervisor Harald Klempe, for a superb student-mentor relationship. I have enjoyed all our discussions and I see you as an inspiration. I sincerely could not have asked for a more compatible supervisor.

Finally, I wish to thank my family for their unconditional love and support through my journey.

Bø I Telemark / 04.05.2017

Viktor Lavik

1 Introduction

Water is the natural resource that sustain all living things on planet earth. Whether previous civilizations prospered or collapsed was highly dependent on the reliability of the water supply (Fetter, 2001). An example is Henry Darcy, who radically enhanced the water supply of Dijon, which had the worst water quality in Europe at the time (Brown, 2002). By locating an excellent quality spring at a higher altitude outside the city, he developed an enclosed system which was entirely gravity driven (Brown, 2002). Hence, Dijon went from misery to prosperity as a consequence of Darcy's ability to assess the surrounding environment.

Freshwater is a limited resource that constitutes 2.8% of the world's water supply (Fetter, 2001). Glaciers and ice caps hold 2.14%, groundwater 0.61%, while lakes and rivers combined, constitute 0.0091%. Only a tiny fraction is available for human consumption, and groundwater constitutes more than 98% of it (Fetter, 2001).

While ground water is an exploited resource in many countries, the utilization is modest in Norway (From, 2010). Firm and dense bedrocks characterize Norway's geology, and the soils often consist of clay and silt with low permeability. Hence, easily accessible surface waters dominate the Norwegian water supply (table 1-1) (From, 2010).

Table 1-1. The total distribution of Norway's water supply expressed in percentage (From, 2010).

Surface water (85%)	Ground water (15%)
Lakes & ponds: 60%	Unconsolidated aquifers: 5%
Rivers & streams: 25%	Bedrocks: 10%

This thesis investigated unconsolidated aquifers as potential sources of water supply at Øverbømoen in Bø municipality. Bø municipality is one of the few places in Norway, where the source of water supply is groundwater from an unconsolidated aquifer. The water is of excellent quality with all parameters well within the limits (Klempe, 2011). The outtake is located northwest at Herremoen, which is part of a large glaciofluvial delta deposit. The delta formed

on top of a granitic gneiss bedrock approximately 9.500 years ago, when the glacier made a brief stay in a constricted part of the Bø valley (figure 1-1) (Jansen, 1983). The Bø River sliced through the delta deposit after the glacier retreated, dividing it in the two parts known today as Øverbømoen and Herremoen (figure 1-2).
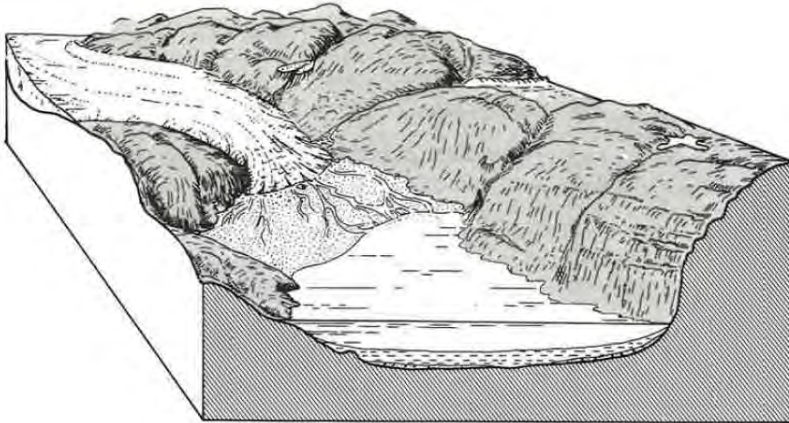
Figure 1-1. The glacier making a brief stay on its retreat through the Bø Valley. The ocean is following closely (Jansen 1983).
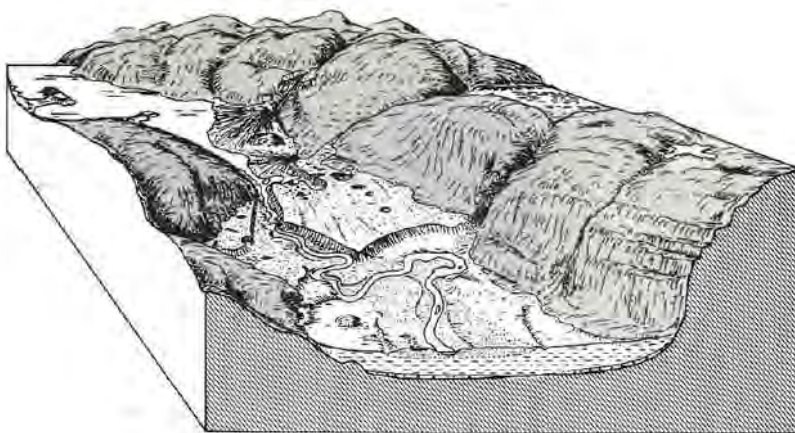
Figure 1-2. The currently known landscape. The ocean has retreated, and the Bø river has sliced the glaciofluvial delta deposit in two parts. Øverbømoen is located to the left and Herremoen to the right (Jansen 1983).

Both the glaciofluvial and fluvial deposits take the shape of terraces (figure 1-3). Drought resistant pine forest dominate the glaciofluvial terrain, which indicate a thick vadose zone with highly drained deposits (Weight, 2008; Jansen, 1983). Elements of spruce occur at the lower fluvial terraces, where the vadose zone is decreasing (Jansen, 1983). Glaciated terranes, such

as kettle holes and drainage channels, frequently cover parts of the glaciofluvial terraces. The only visible esker however, is located at Øverbømoen. Sand, gravel and rocks in podzol profiles constitute the surfaces (Jansen, 1983).
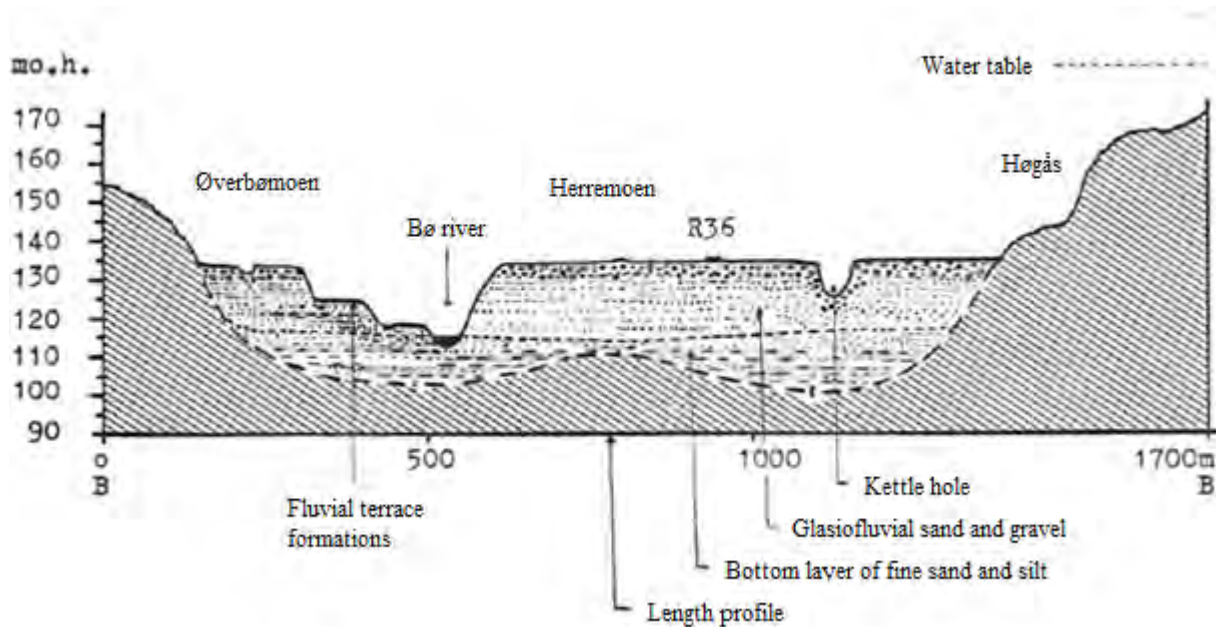
Figure 1-3. A cross section of the glaciofluvial and fluvial deposits, revealing the terrace formations, estimated water table and sediment distribution (Jansen, 1983).

A glaciofluvial deposit is a valuable resource that is often extracted by quarries for various purposes, such as road construction and concrete aggregates (Jansen, 1983). However, with its coarse sorted material it could also be a potential aquifer for water supply (Fetter, 2001).

1.1 Area description

Øverbømoen is located in Bø municipality, southeast of Norway. It lies just below the marine limit 11.6 km west of the Bø center, close to the border between Bø and Seljord (figure 1-4).

Figure 1-4. Øverbømoen (red circle), located 11.6 km west of Bø.

Øverbømoen constitutes a lesser part of the glaciofluvial delta deposit, and lies opposite of Herremoen, which constitutes the bulk of the delta (figure 1-5).
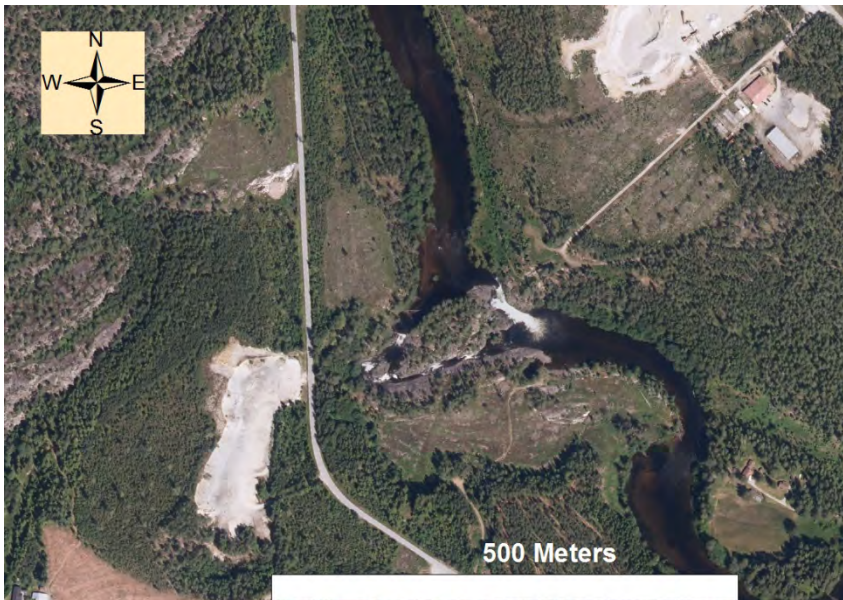

Figure 1-5. Øverbømoen located to the left of the Bø river, while a part of Herremoen is visible to the right of the river.

A digital elevation model (DEM) of the area greatly assists the ability to distinguish geologic features (Figure 1-6). The terraces become clearly defined, and an esker and a kettle hole are clearly visible at the upper terrace. The topography surrounding the esker takes the shape of a delta, emanating from the west. If this is the case, then the glacier had a more surrounding presence than what Jansen (1983) depicts (Figure 1-1). Also notice how the elevation of the river rapidly drops 10 meters at the middle where the waterfall (Herrefoss) is located. In this area, the bedrock becomes exposed as it crosses the river, revealing hints of the subsurface conditions.
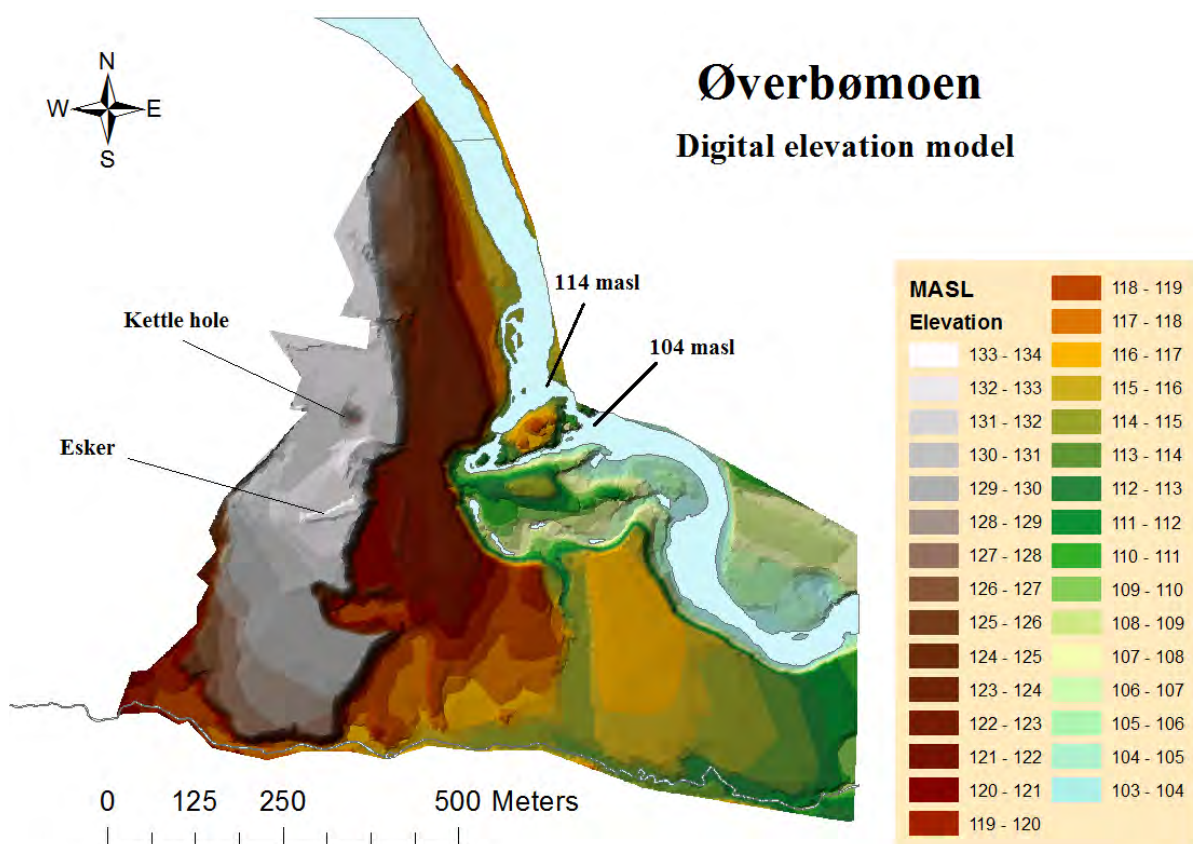
Figure 1-6. A digital elevation model (DEM) of Øverbømoen with one-meter contours.

The sediment deposition of Øverbømoen consists mainly of glaciofluvial and fluvial deposits, but there are also elements of exposed bedrock and bog (figure 1-7).
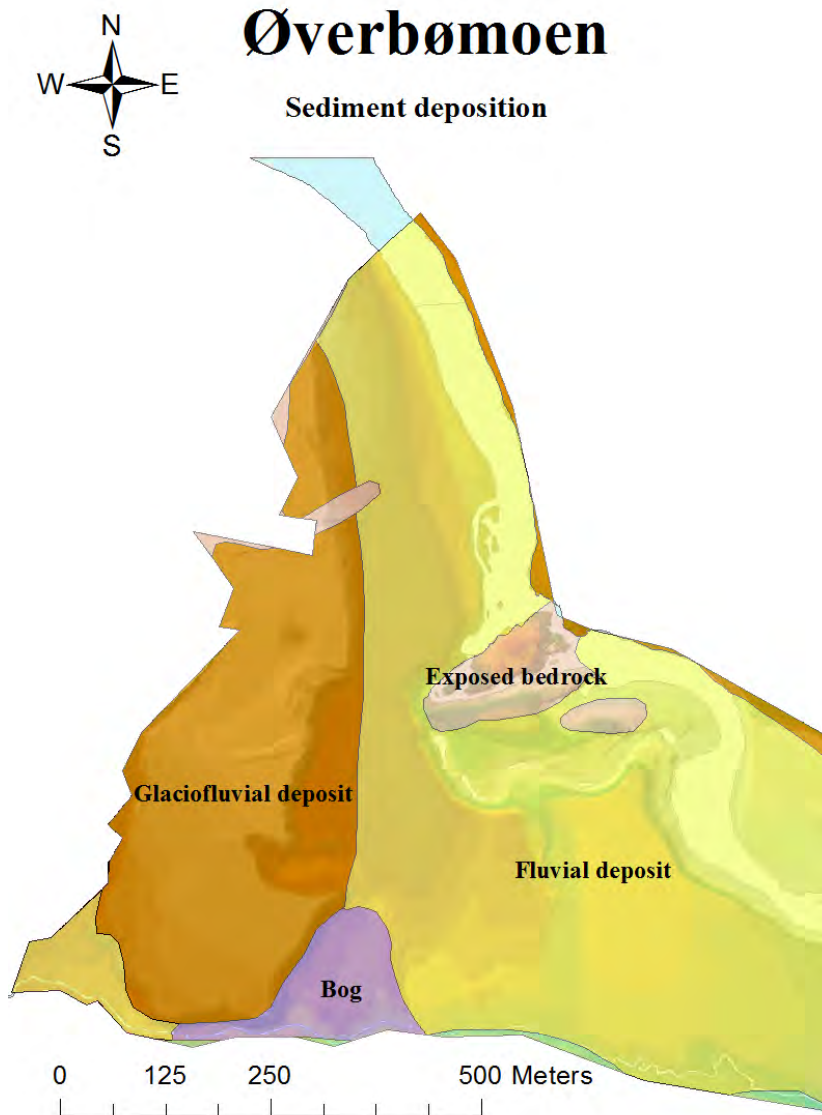
Figure 1-7. The sediment deposition at Øverbømoen. Modified from Jansen (1983).

1.2 Properties of ideal aquifers

The ability of an aquifer to supply water is primarily determined by the porosity and permeability of the aquifer (Weight, 2008). Porosity and permeability controls specific yield, which decides the quantity of water an aquifer can discharge. Porosity (total pore space) determines the storability of an aquifer, and is a function of grain size, shape and packing (Weight, 2008). A decrease in grain size increases both the total porosity and the specific retention, resulting in a higher storage capacity but a smaller specific yield (figure 1-8) (Weight,

2008; Fetter, 2001). E.g. clay has the highest porosity (50%), but also the highest specific retention (48%).
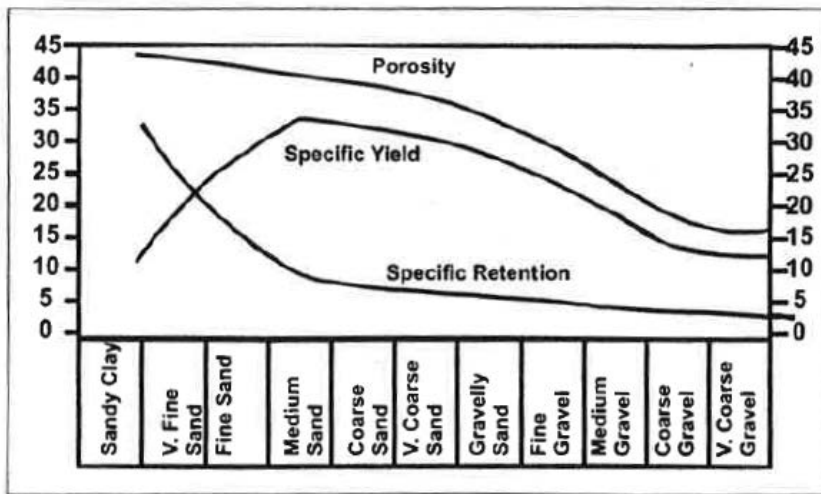
Figure 1-8. How grain size relates to porosity, specific yield, and specific retention (expressed in percentage) (Weight, 2008).

The packing is a function of the size, shape and arrangement of the grains (Weight, 2008). A homogenous aquifer that consists of round grains of equal diameters has two packing arrangements that represent the extremes of porosity (figure 1-9). The most porous is cubic packing, where grains are stacked vertically on top of each other, yielding a porosity of 47.6%. The least porous is rhombohedral packing, where grains are compressed in their most compact form, yielding a porosity of 25.9%. A mixture of grain sizes will also reduce the overall porosity, as smaller grains fit between larger ones (Table 1-2) (Weight, 2008).

Side View   Top View

$V_T = (2r)^2 = 8r^3$

$V_S = 4/3\pi r^3$

$V_v = \dfrac{V_T - V_S}{V_S} = \dfrac{8r^3 - \frac{4}{3}\pi r^3}{8r^3}$

Cubic Packing $\theta = 90°$ $V_v = 0.476 = 47.6\%$

$V_T = (2r)^2 \times 2r\sin\theta = 8r^3/2^{0.5}$

$V_S = 4/3\pi r^3$

$V_v = \dfrac{8\dfrac{r^3}{\sqrt{2}} - \dfrac{4}{3}\pi r^3}{8\dfrac{r^3}{\sqrt{2}}}$

$\theta = 45°$

Rhombohedral Packing $\theta = 60°$

$V_v = 0.259 = 25.9\%$

Figure 1-9. Cubic and rhombohedral packing with determination of porosity. (V_T = Total volume, V_S = Solid volume, V_V = void volume) (Weight, 2008).
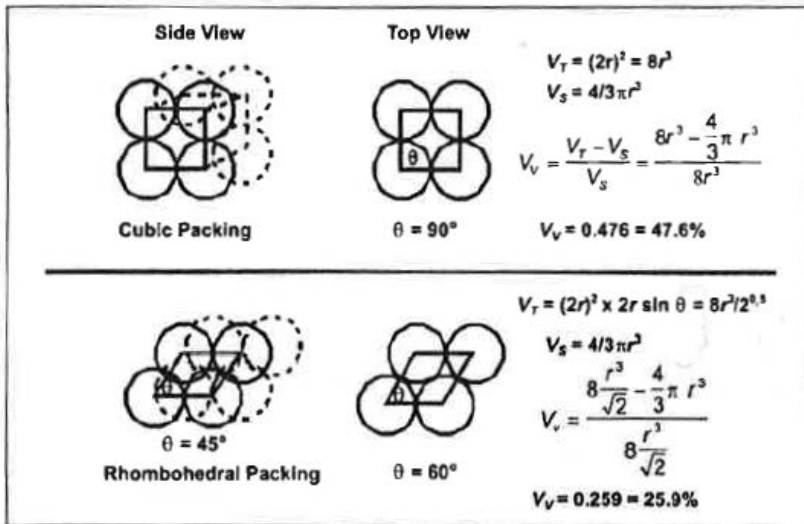
Table 1-2. Ranges of porosities in typical geologic materials. Note that the porosity of a mixture of sand and gravel is less than each material separately (Weight, 2008).

Unconsolidated materials	$\eta\%$	Consolidated rock	$\eta\%$
Clay	40–70	Sandstone	5–35
Silt	35–50	Limestone/dolomite	<1–20
Sand	25–50	Shale	<1–10
Gravel	20–40	Crystalline rock (fractured)	<1–5
Sand and gravel	15–35	Vesicular basalt	5–50

However, the storability of an aquifer is of no significance unless it possesses the ability to conduct fluids. Clay can hold the highest amount of water, but the small grains create a larger surface area that causes tremendous frictional flow resistance, making it an aquitard (confining layer) (Fetter, 2001). An ideal aquifer possesses an interconnectedness that allows sufficient water circulation between the pores. The most prolific producers of groundwater are the unconsolidated coarse-grained sediments with high intrinsic permeability. Intrinsic permeability is a function of the pore size opening (Fetter, 2001). The larger the pore opening, the larger the intrinsic permeability (Weight, 2008). Well-sorted sediments possess greater permeability than poorly sorted sediments, where finer material fill the voids between coarser

materials (Fetter, 2001). If sediments are well sorted, the intrinsic permeability increases proportionally with the grain size (table 1-3) (Fetter, 2001).

Table 1-3. Ranges of intrinsic permeabilities and hydraulic conductivities for unconsolidated sediments (Fetter, 2001).

Material	Intrinsic Permeability (darcys)	Hydraulic Conductivity (cm/s)
Clay	$10^{-6} - 10^{-3}$	$10^{-9} - 10^{-6}$
Silt, sandy silts, clayey sands, till	$10^{-3} - 10^{-1}$	$10^{-6} - 10^{-4}$
Silty sands, fine sands	$10^{-2} - 1$	$10^{-5} - 10^{-3}$
Well-sorted sands, glacial outwash	$1 - 10^{2}$	$10^{-3} - 10^{-1}$
Well-sorted gravel	$10 - 10^{3}$	$10^{-2} - 1$

Sorted layers of sand and gravel constitute the optimal aquifers for water supply, as they possess a sufficient combination of porosity and intrinsic permeability, resulting in a satisfactory specific yield (figure 1-8 and table 1-3). Glaciofluvial deposits (Kames, eskers and outwash deposits) are excellent examples of well-sorted, stratified sediments (Weight, 2008). The thickness of surface casing should also be considered when investigating potential aquifers. Fetter (2001) recommends at least 10 meters of surface casing to prevent detrimental interaction with surface waters.

1.3 Geophysics of the subsurface

The mining and petroleum industries were among the first to utilize geophysical instruments, but hydrogeologists soon caught up when they realized the efficiency provided by geophysical surveys (Fetter, 2001). Geophysical techniques are extensively used for shallow subsurface explorations, yielding valuable information about suitable groundwater sources (Reynolds, 2011). Geophysical instruments can indirectly determine the extent and the identity of the geologic materials beneath the ground (Fetter, 2001). Attributes such as thickness, angels, depth to water table, depth to bedrock, and location of subsurface faults can all be identified.

However, in order to achieve reliability of the measurements, it is necessary to correlate geophysical data with well logs or test-boring data (Fetter, 2001).

1.3.1 Electrical resistivity tomography (ERT)

Electrical resistivity is the inverse of conductivity, and is a fundamental physical property that can be used diagnostically (Reynolds, 2011; Weight, 2008). Resistivity is defined as the ratio between electric field strength and current density, which is a local form of Ohm's law (Jeppson & Dahlin, 2016). It is possible to measure resistivity in the earth by generating direct or low-frequency alternating current at the surface, and measure the voltage (potential difference) between two potential electrodes (Figure 1-10) (Fetter, 2001).
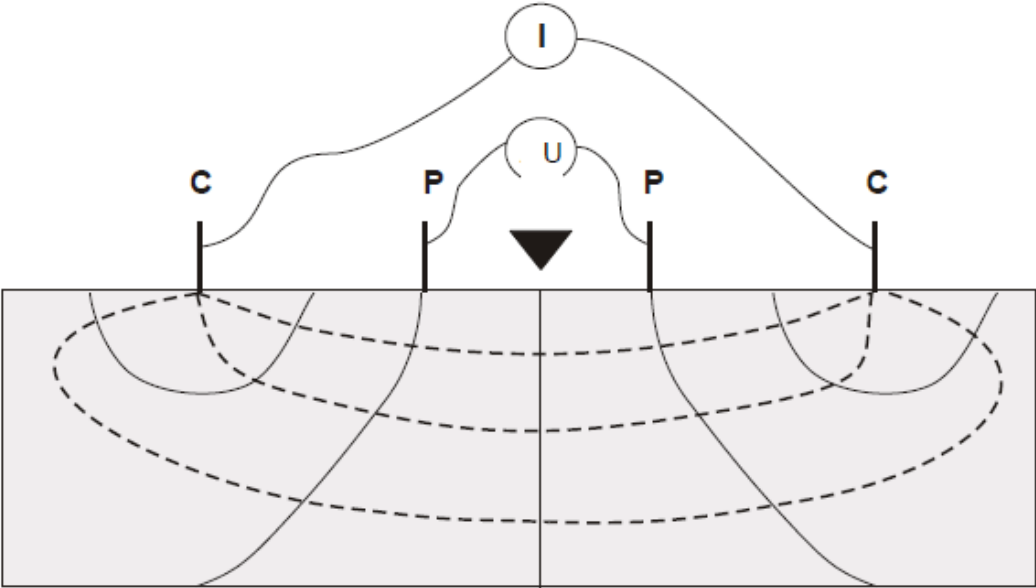

Figure 1-10. The principle for resistivity measurements. C = current electrodes, P = potential electrodes, I = current intensity, U = voltage (potential difference), solid lines = potential lines, dotted lines = current lines, triangle = measuring points (Jeppson & Dahlin, 2016).

Knowing the specific current and the difference in voltage makes it possible to calculate an apparent resistivity (p_a) (Loke, 2015). The apparent resistivity is a product of the resistance (Ω) and a geometric factor determined by the electrode spacing (Solberg et al., 2011; Loke, 2015). Resistivity is thus expressed in ohm-meters (Ωm). Apparent resistivity is the weighted average

of all resistivity values within the volume of each individual measurement (Solberg, 2011). All the apparent resistivities from the raw data assembles into a psuedosection, which gives an estimation of the subsurface conditions (Solberg et al., 2011). The apparent resistivity will only equal the true resistivity (p) if the subsurface is homogenous, which is rarely the case (Loke, 2015). The true resistivity of the subsurface is found by converting the apparent resistivity in an inversion program. Inversion is a process that reduces the difference between the calculated and measured apparent resistivities, represented by a root-mean-square value (RMS) (Loke, 2015). The inversion attempts to find a response model that agrees with the measured field data. The model is only reliable when the difference (RMS) is sufficiently small (Loke, 2015). The result is a 2D-model divided into blocks, where each block has been assigned its true resistivity (Solberg et al., 2011). The top layer has the best resolution with a block thickness half the size of the electrode distance. The block thickness for each successive layer thereafter normally increases by 10%. Hence, shorter electrode distances yield better resolutions (Solberg et al., 2011).

1.3.1.1 *Resistivity properties*

The detectability of geologic targets depends on sufficient contrasts in physical properties, and convenient factors of scale, shape, and depth of the target (Weight, 2008). Detailed information can be interpreted from heterogeneous areas with reasonable resistivity contrasts. The resolution (determined by electrode spacing) is also important as it complements the detectability (Weight, 2008).

Resistivity is highly dependent on porosity and permeability, which is why igneous and metamorphic rocks tend to have the highest resistivity while sedimentary rocks are the most conductive (Reynolds, 2011). The age of a rock is also important as older rocks have lower porosity and permeability due to secondary infilling of interstices by mineralization (Reynolds, 2011). Jeppson & Dahlin (2016) lists porosity, degree of saturation, and the resistivity of the pore fluid as the most important factors affecting the resistivity. Other factors are mineral composition and mineral structure. They also mention three main pathways electric current take in porous materials. It may flow through the pore fluid (electrolytic conduction), the mineral grains (electronic conduction), or the adsorbed ions surrounding the material (figure 1-11).
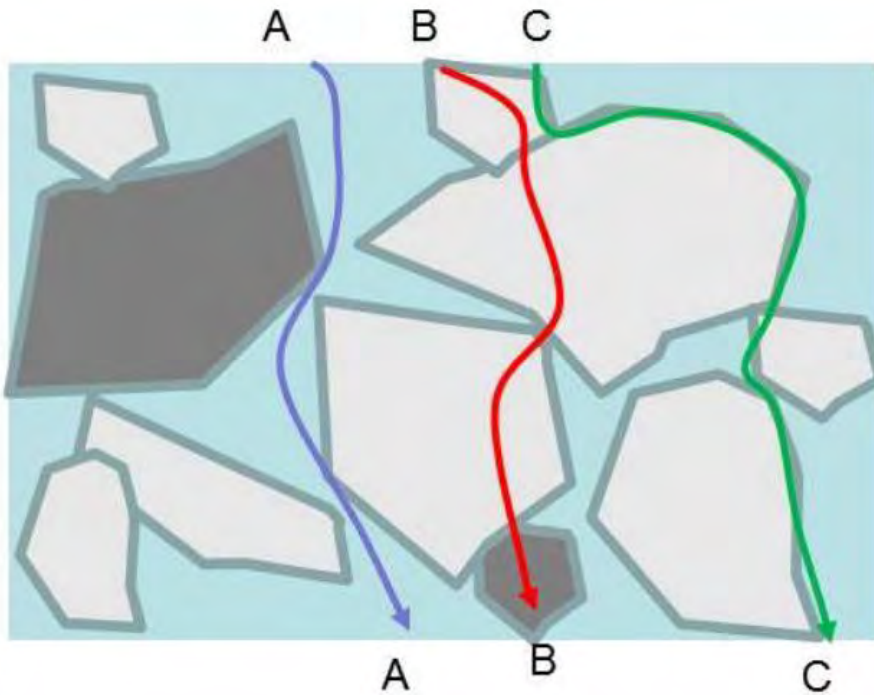
Figure 1-11. Pathways for electric current in a geologic material. A is through pore fluid, B is through mineral grains, and C is through adsorbed ions (Jeppson & Dahlin, 2016).

The pore fluid usually offers the path of least resistance; hence, it is the dominating pathway through porous media such as gravel, sand and moraine. However, if the pores are filled with air or other insulating gases, it will yield high resistivities. Thus, it often appears a significant contrast in resistivity over and below a water table (Jeppson & Dahlin, 2016).

The degree of saturation is often the decisive factor that creates contrasts in resistivity (Reynolds, 2011; Jeppson & Dahlin, 2016). The significance of water content is evident in table 1-4, where three orders of magnitude constitutes the difference between wet and dry granite *porphyry*. In addition, the data shown in table 1-5 reveals that even slight changes in water content can have a colossal effect on the resistivity.

Table 1-4. The effect of water content on the bulk resistivity of rocks (Telford et al., 1990).

Rock type	Resistivity range (Ωm)
Granite porphyry	4.5×10^3 (wet) – 1.3×10^6 (dry)
Feldspar porphyry	4×10^3 (wet)
Syenite	$10^2 - 10^6$
Diorite porphyry	1.9×10^3 (wet) – 2.8×10^4 (dry)
Porphyrite	$10 - 5 \times 10^4$ (wet) – 3.3×10^3 (dry)
Carbonatized porphyry	2.5×10^3 (wet) – 6×10^4 (dry)
Quartz diorite	$2 \times 10^4 - 2 \times 10^6$ (wet) -1.8×10^5 (dry)

Table 1-5. Different rock resistivity with different degrees of water content (Telford et al., 1990). Note that the resistivity in Granite drops seven orders of magnitude with a H_2O increase of 0.31%.

Rock	% H_2O	ρ (Ωm)
Siltstone	0.54	1.5×10^4
Siltstone	0.38	5.6×10^8
Coarse grain SS	0.39	9.6×10^5
Coarse grain SS	0.18	10^8
Medium grain SS	1.0	4.2×10^3
Medium grain SS	0.1	1.4×10^8
Graywacke SS	1.16	4.7×10^3
Graywacke SS	0.45	5.8×10^4
Arkosic SS	1.0	1.4×10^3
Organic limestone	11	0.6×10^3
Dolomite	1.3	6×10^3
Dolomite	0.96	8×10^3
Peridotite	0.1	3×10^3
Peridotite	0	1.8×10^7
Pyrophyllite	0.76	6×10^6
Pyrophyllite	0	10^{11}
Granite	0.31	4.4×10^3
Granite	0.19	1.8×10^6
Granite	0	10^{10}
Diorite	0.02	5.8×10^5
Diorite	0	6×10^6
Basalt	0.95	4×10^4
Basalt	0	1.3×10^8
Olivine-pyrox.	0.028	2×10^4
Olivine-pyrox.	0	5.6×10^7

Temperature may also affect resistivity values significantly. Conductors (resistivity less than 10^{-5} Ωm) vary inversely with temperature and their peak of conductivity is reached at absolute

zero (0 kelvin = -273.15 °C) (Telford et al., 1990). Semi-conductors (10^{-5} – 10^7 Ωm) however, react the opposite way by becoming insulators (> 10^7 Ωm) at low temperatures (Telford et al., 1990).

1.3.1.2 Interpretation

Resistivity values cover an enormous range, and several authors provide tables with resistivity values corresponding to different geologic materials (Table 1-6, 1-7 & figure 1-12).

Table 1-6. Resistivity values corresponding to different materials by Solberg et al. (2011) & Reynolds (2011).

Material	Resistivity interval (Ωm)
Igneous and metmorphic rocks	1000 - 100 000
Sedimentary rocks	7 - 100 000
Wheathered layer	5 - 50 000
Gneiss (various)	6.8×10^4 - 3×10^6
Granite	300 - 1.3×10^6
Granite (wheathered)	30-500
Clays	1 - 100
Clay (saturated)	20
Clay (very dry)	50 - 150
Sand clay/clayey sand	30 - 215
Sand (dry)	80 - 1050
Sand (quaternary/recent)	50 - 100
Sand and gravel (saturated)	< 100
Sand and gravel (dry)	< 1400
Gravel (saturated)	100
Gravel (dry)	1400
Alluvium and sand	10 - 800
Moraine	10 - 5 000
Top soil	250 - 1700
Seawater	0.5 - 1
Freshwater	5 - 100

Table 1-7. Resistivity values corresponding to different materials by Jeppson & Dahlin (2016).

Material	Resistivity interval (Ωm)
Clay	1 - 100
Sand (dry)	800 - 5 000
Sand (wet)	100 - 500
Moraine (clay poor)	300 - 3 000
Moraine (clay rich)	20 - 200
Bedrock (poorly fractured)	2 000 - 50 000
Bedrock (fractured)	200 - 4 000
Sandstone	100 - 20 000
shale	50 - 10 000
Limestone	300 - 3 000
Salt	> 10 000
Ice (glacier)	10^5 - 10^6
Water (sea water - deionized water)	10^{-1} - 10^5
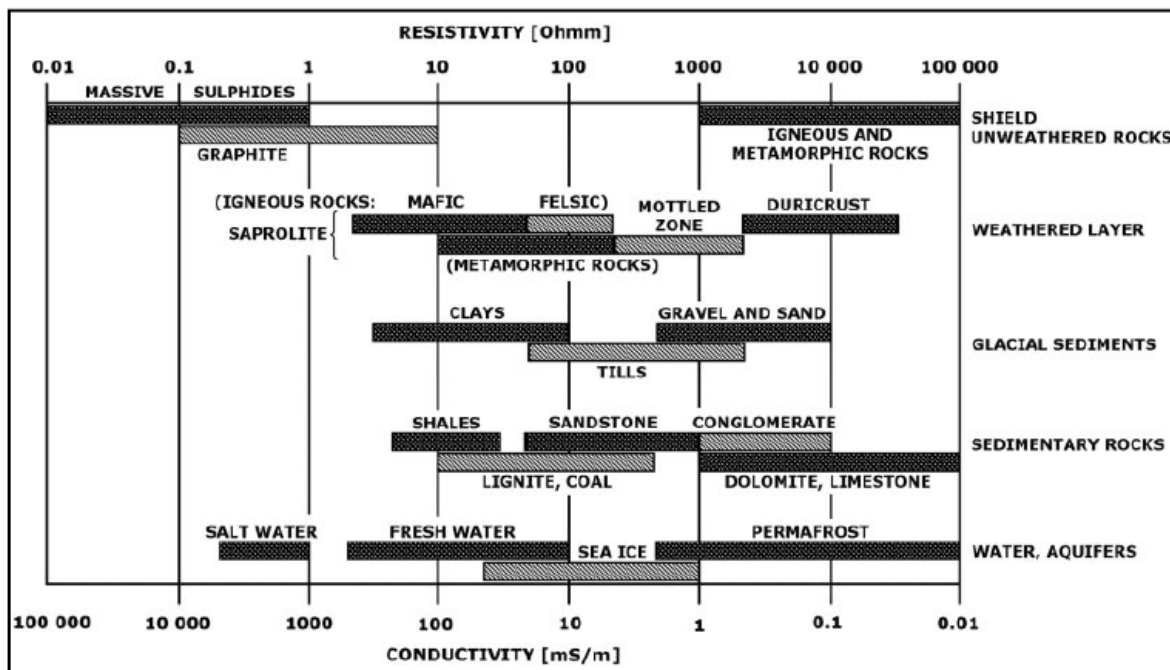
Figure 1-12. Resisitivity ranges for different geologic materials by Palacky (1987).

Not only do the resistivity values vary significantly between the sources, they also have wide intervals that overlap with each other and thus, making the interpretation more challenging. Hence, Jeppson & Dahlin (2016) emphasize that a direct translation of resistivity values into a certain geologic material is virtually impossible. Reliable interpretation must be based on geologic information that reveal what materials are likely to be found in the given area (Jeppson & Dahlin, 2016).

Another important aspect to consider when interpreting resistivity sections is the path of least resistance. Current always prefer the path of least resistance, which may cause a layer of low resistivity to appear thicker on a resistivity profile than what it really is (Solberg et al., 2011). The phenomenon is a 3d-effect, where the current takes a detour around conductive materials before it reaches the layer beneath. Hence, layer boundaries should be carefully interpreted on a resistivity profile (Solberg et al., 2011).

1.3.1.3 Electrode Configurations

The geometry of the electrode array affects the apparent resistivity value (Reynolds, 2011). There are over one hundred array types currently recognized, but the three main configurations: *wenner*, *schlumberger* and *dipole-dipole* have persisted through time (figure 1-13) (Reynolds, 2011; Weight, 2008). *Gradient*, a non-symmetrical form of the *schlumberger*, has also become increasingly popular after the introduction of multi-channel systems (Loke, 2015). Different electrode configurations provide specific advantages, disadvantages and sensitivities; thus, the choice of array is crucial (table 1-8) (Reynolds, 2011).
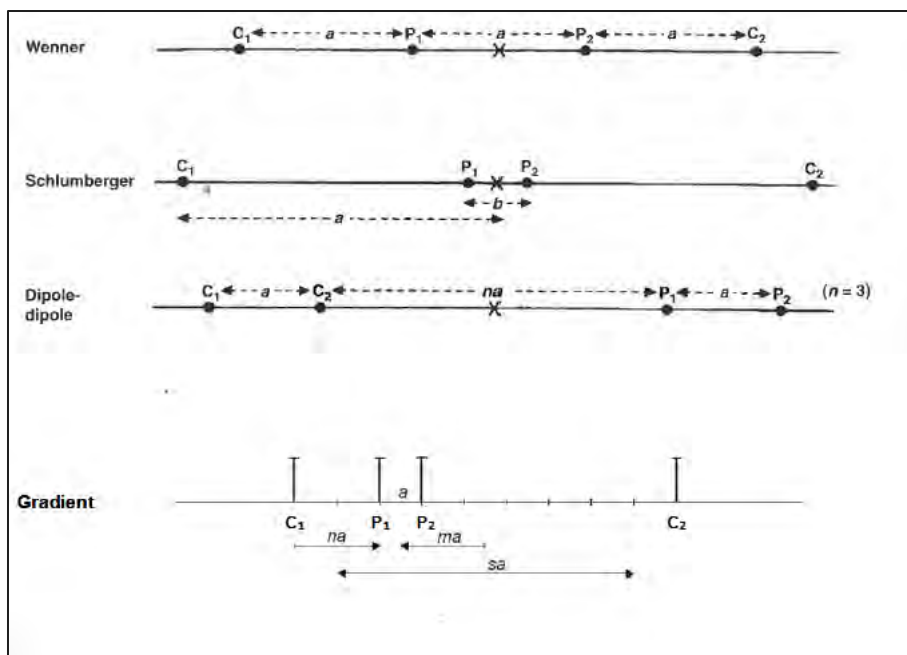
Figure 1-13. The most common electrode configurations in resistivity surveys. "C" denotes current electrodes, "p" denotes potential electrodes, and "a" denotes distances (Reynolds, 2011; Loke 2015).

Table 1-8. Advantages/disadvantages of the main configurations in electrical resistivity surveys. + = poor; ++ = moderate; +++ = good (Reynolds, 2011; Solberg et al., 2011).

	Wenner	Schlumberger	Gradient	Dipol-dipol
Vertical resolution	+ + +	+ +	+ + +	+
Depth of penetration	+	+ +	+ +	+ + +
Convenience for 2D-mapping	+ +	+ + +	+ + +	+
Sensitivity to orientation	Yes	Yes	Yes	Moderate
Sensitivity to lateral inhomogeneities	High	Moderate	High	High

1.3.2 Ground Penetrating Radar (GPR)

Ground penetrating radar (GPR) maps the subsurface by transmitting electromagnetic waves into the ground within the frequency range of 10 MHz to 2 GHz (Annan, 2009; Cassidy, 2009). The frequency determines depth of penetration and resolution (Larsen et al., 2015). High frequencies have low penetration depth and high resolution, while low frequencies have the opposite effect (Larsen et al., 2015). GPR detects reflections from subsurface features by moving a transmitter and a receiver over the surface in a fixed geometry (figure 1-14) (Annan, 2009).
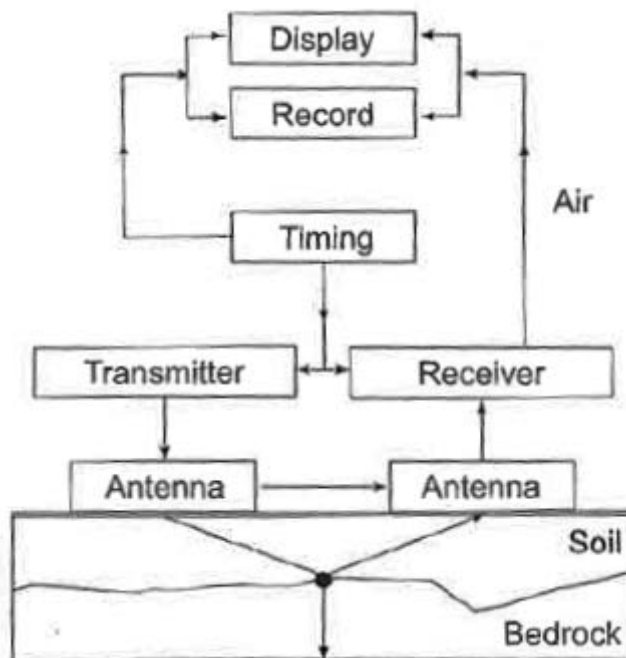
Figure 1-14. A simplified block diagram showing the main components of a GPR system (Annan, 2009).

The transmitter generates a pulse of electromagnetic waves (ca. 50 000/sec), propagating at high velocities in a broad beam (Reynolds, 2011). The velocity through materials depends on the relative dielectric constant, which is the ability to resist the flow of electromagnetic waves (Reynolds, 2011; Cassidy, 2009). The velocity is given by $V = c/\sqrt{\varepsilon_r}$, where c is lightspeed in vacuum and ε_r is the relative dielectric constant (Larsen, Tønnesen and Olsen, 2015). The GPR method is based on variability within the stratigraphy, as it is the contrast in relative dielectric constants between adjacent layers that creates the reflection of electromagnetic radiation

28

(Reynolds, 2011). The greater the velocity contrast, the greater the amount of electromagnetic energy reflected. Materials with low ε_r may appear as transparent (e.g. polar ice) while materials with high ε_r, appear as completely impermeable (e.g. clay and sea water). Significant velocity contrasts reflect signals with amplitudes greater than a given threshold, making differentiation possible (Figure 1-15).

The received signal is a function of the two-way travel time (time between the instant of transmission and the detection by the receiver) and is displayed as a radargram (Figure 1-16) (Reynolds, 2011). A radargram is not directly an image of the subsurface, but rather the time-dependent response of the subsurface materials to the propagated radio waves (Cassidy, 2009). Hence, timing is the essence of a GPR system, recording the generation and detection of signals (Annan, 2009; Reynolds, 2011).
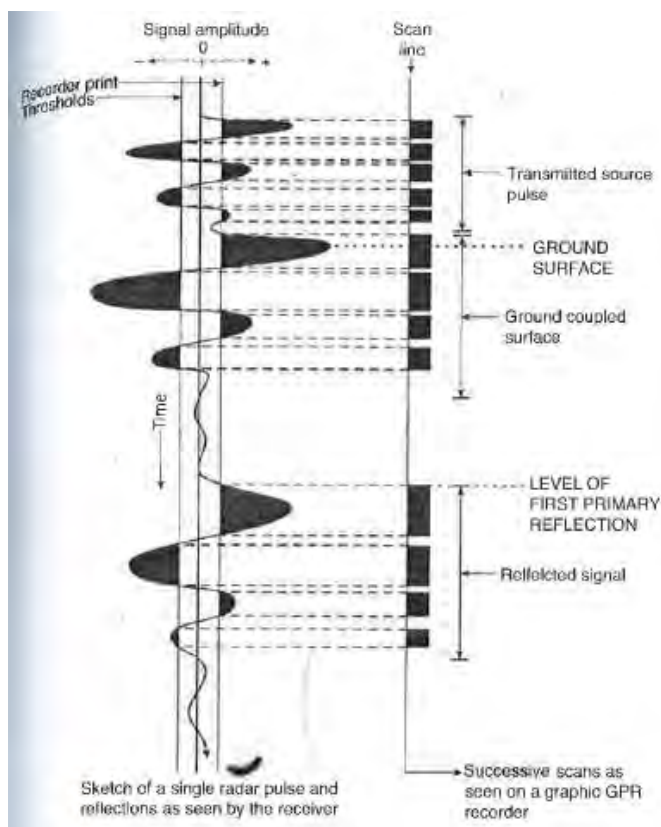
Figure 1-15. Schematic example revealing how wave amplitudes above the threshold limit are translated as dark segments on a graphic recorder output (Reynolds, 2011).
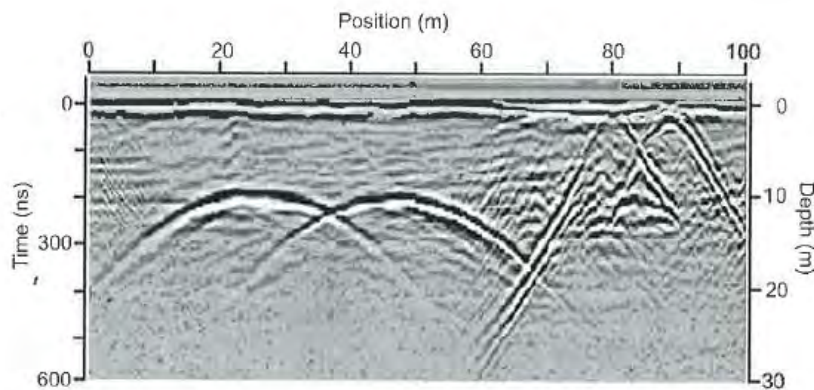
Figure 1-16. A radargram of 50 MHz ground penetrating radar (GPR) across two road tunnels. The radar signal amplitude is a function of position (horizontal axis) and travel time (vertical axis) (Annan, 2009).

1.3.2.1 Interpretation

GPR interpretation is application dependent and may thus be very subjective (Annan, 2003). It is based on deriving a geologic model by recognizing and conjugating reflections and reflection patterns (Koziel et al., 1995). Different textures within a radargram can be identified through zones that inhabit different patterns of reflections (Figure 1-17 & 1-18) (Reynolds, 2011). Different velocities also represent different textures (Table 1-9). Classification occurs by eye of the interpreter (Reynolds, 2011). Éckes & Hickin (2001) however, state that radargrams should not be treated equally to seismic reflection profiles. They emphasize that identifying interference patterns is of higher significance than discrete reflections and diffractions when interpreting radargrams. The reliability of GPR interpretation depends on the experience of the interpreter, and their ability to connect it to other research data (Éckes & Hickin, 2001).
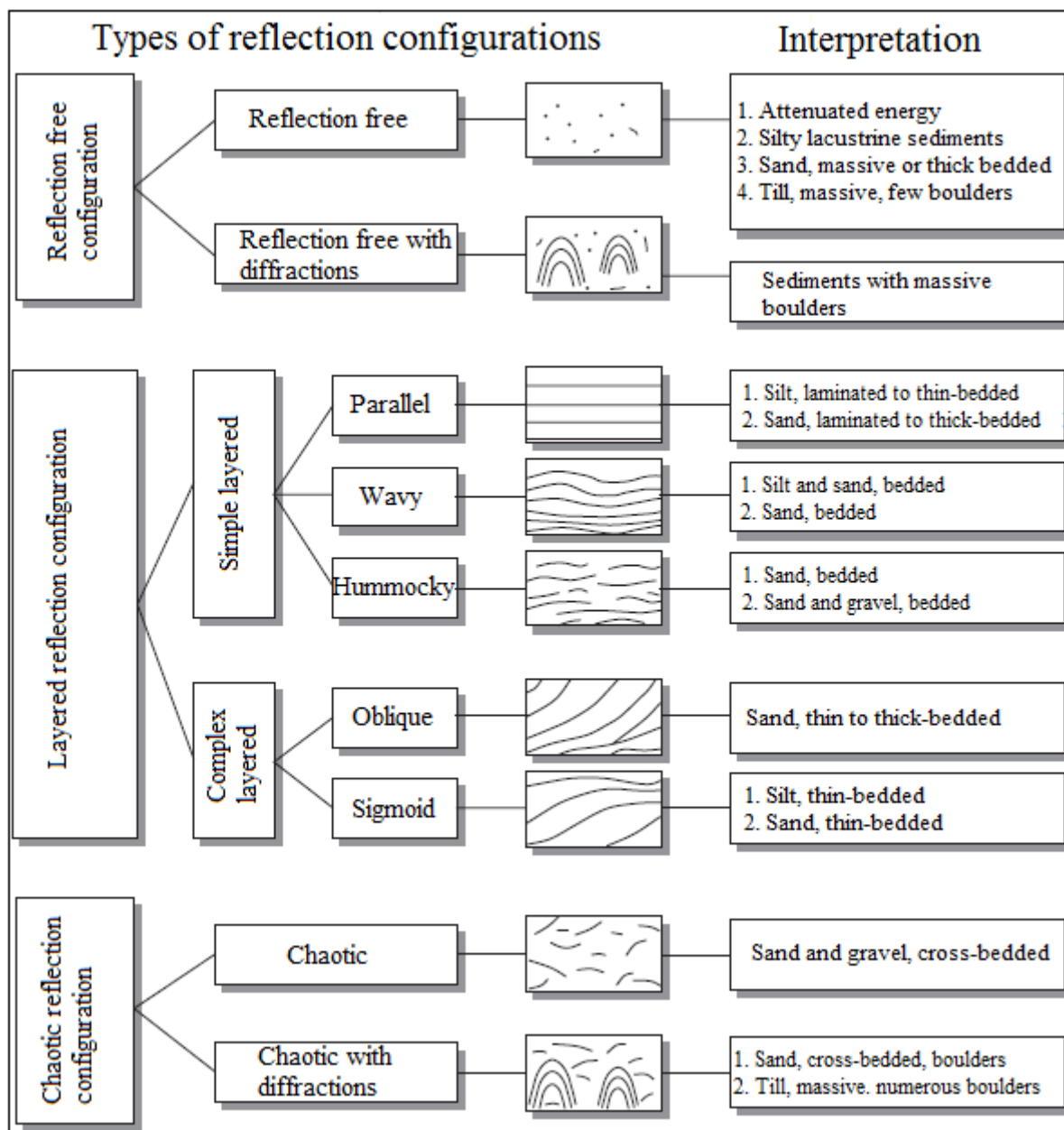
Figure 1-17. Types of reflection configurations with plausible interpretations in terms of the lithologic and stratigraphic properties of the sediments (Beres & Haeni, 1991).

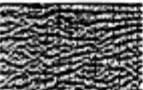|	**GPR FACIES**	**INTERPRETATION**
1	reflection free	1, attenuated energy 2, glacial till
2	hummocky or chaotic with macro scale diffractions	bedrock
3	chaotic with meso scale diffractions	alluvial fan facies 1: fan facies with boulders
4	chaotic, high-frequency with micro scale diffractions	artificial fill, buried utility cables and pipes, trees
5	discontinuous, hummocky, wavy	alluvial fan facies 2: 1, poorly bedded sheetflood sand and gravel; 2, matrix rich debris flow diamicton
6	horizontally continuous, layered, parallel	alluvial fan facies 3: 1, horizontally bedded sheetflood sand and gravel; 2, clast rich debris flow diamicton
7	chaotic or poorly defined	alluvial fan facies 4: thick, matrix rich debris flow diamicton
8	trough shaped	channel fill
9	oblique clinoforms	delta foresets
10	complex sigmoid oblique	modern floodplain: migrating channel bars

Figure 1-18. GPR facies interpreted by Éckes & Hickin (2001). The vertical depth varies between 6 and 12 meters.

Table 1-9. Typical dielectric constants (ε_r), electrical conductivities and velocities (v) observed in common geologic materials (Reynolds, 2011).

Material	ε_r	V (mm/ns)	Conductivity (mS/m)
Air	1	300	0
Water (fresh)	81	33	0.5
Water (sea)	81-88	33	3000
Polar snow[1]	1.4-3	194-252	~0.05
Polar ice[2]	3-3.15	168-172	≤0.06-0.08
Temperate ice	3.2	167	5×10^{-8}
Pure ice	3.2	167	5×10^{-8}
Freshwater lake ice	4	150	$1-10^{-6}$
Sea ice	2.5-8	78-157	10-100
Permafrost	2-8	106-212	0.1-10
Active layer permafrost	25	60	
Gravel	5	134	10
Sand and gravel (unsaturated)	3.5-6.5	118-160	0.007-0.06
Sand and gravel (saturated)	15.5-17.5	72-76	0.7-9
Coastal sand (dry)	5-10	95-134	0.01-10
Sand (dry)	3-6	122-173	$10^{-4}-1$
Sand (coastal, dry)	5-10	95-134	0.01-1
Sand (wet)	10-32	53-95	0.1-10
Sand (golf course)	10-25	60-95	10
Silt (unsaturated)	2.5-5	134-190	1-100
Silt (saturated)	22-30	55-64	≤100
Clay (dry)	2-5	134-212	2-100
Clay (wet)	8-40	47-106	20-1000
Till (unsaturated)	7-21	65-113	2.5-10
Till (saturated)	24-34	51-61	2-5
Moraine	7-14	80-113	$10^{-5}-10^{-7}$
Marsh	12	86	
Peat (freshwater)	57-80	33-40	≤40
Agricultural land	15	77	
Pastoral land	13	83	
Soil (fine-grained)	41-49	43-47	40
Average 'soil'	16	75	5
Granite	5-8	106-120	$10^{-3}-10^{-5}$
Limestone (dry)	4-8	100-113	
Limestone (wet)	6-15	77-122	10-100
Dolomite	6.8-8	106-115	
Basalt (wet)	8	106	

2 Issue

The aim of this thesis was to identify optimal aquifers for drinking water supply at Øverbømoen. Øverbømoen is part of a glaciofluvial delta deposit; hence, it was hypothesized that this area would contain aquifers adequate for drinking water supply. The object of interest was sorted layers of saturated sand and gravel deposits, as they are more likely to provide a satisfactory specific yield for larger populations.

A secondary objective of the thesis was to investigate if a large kettle hole had an impact on the subsurface conditions of profile 5. The kettle hole is located across the river, opposite of the profile.

The exploration of Øverbømoen prior to this hydrogeological survey was modest, so a broad investigation was conducted to acquire a decent overview of the subsurface conditions. Seven main profiles including both GPR and ERT were initially planned, but GPR was excluded for profiles 1, 2 and 3 due to challenging terrain (Figure 2-1 and table 2-1). Supplementary GPR profiles were also made as an addition to the seven main profiles (figure 2-2). The choice of investigation sites was based on previous drillings, geologic features, topography, and desired area coverage.
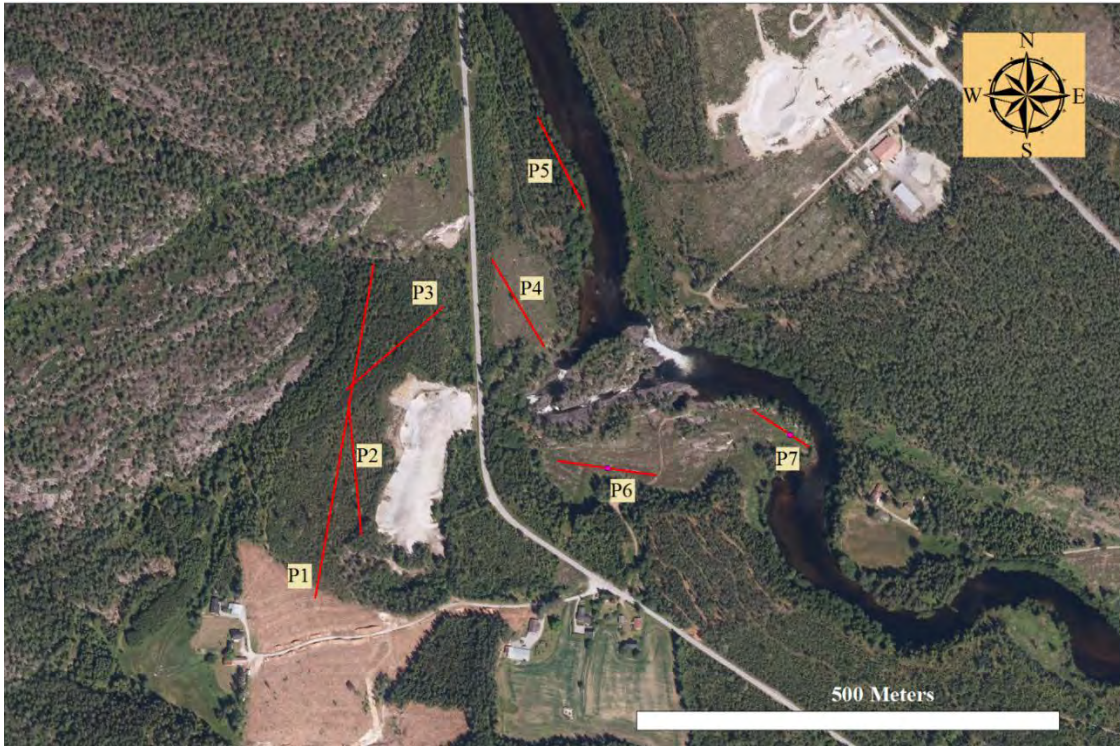
Figure 2-1. Øverbømoen with the seven main profiles investigated (ERT and GPR). The profile order is listed from P1 (profile 1) to P7 (profile 7).
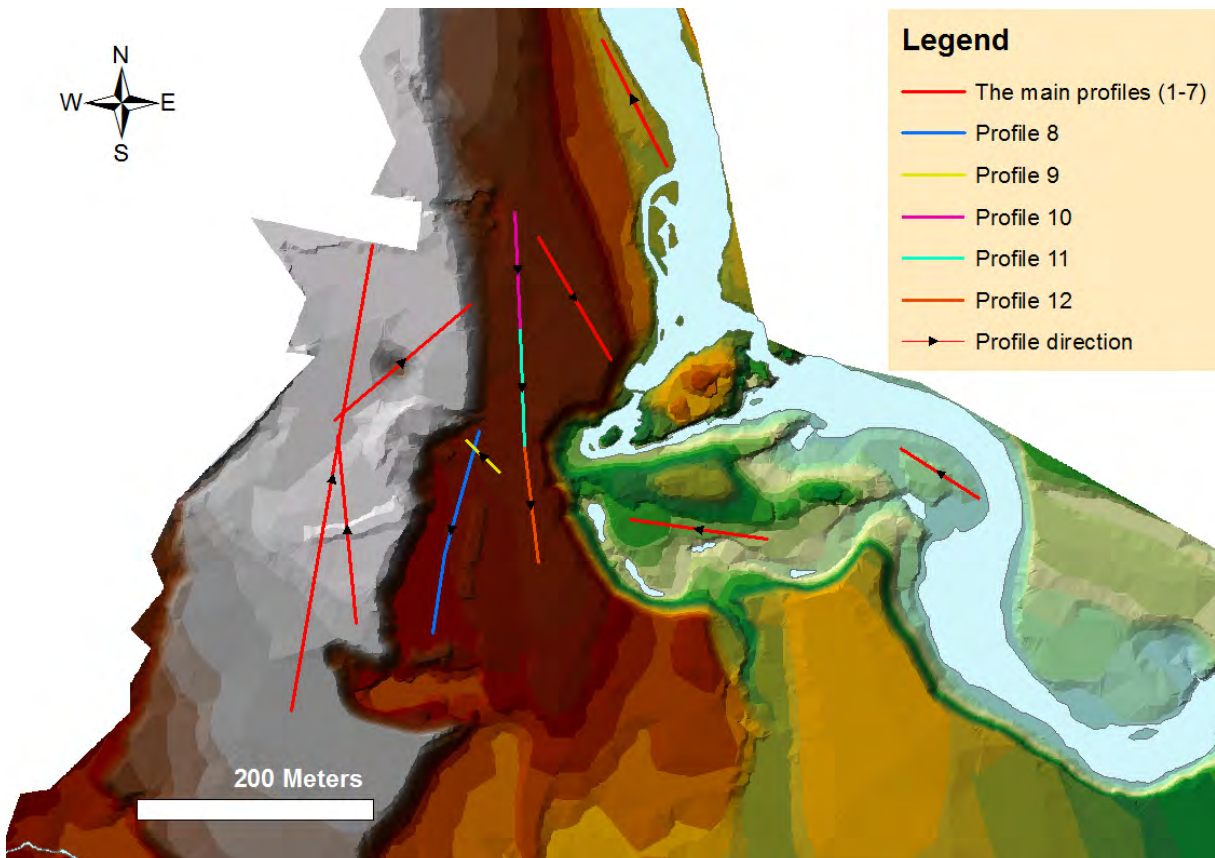
Figure 2-2. The main profiles with supplementary GPR profiles in a DEM of Øverbømoen.

Table 2-1. Information about the investigated profiles.

Profile overview						
Profile	Survey	Date	Electrode distance	Profile length	Start point	End point
1	ERT	24.11.2016	5 m	400 m	32V 492730 6587279 UTM	32V 492799 6587674 UTM
2	ERT	01.12.2016	2 m	160 m	32V 492785 6587354 UTM	32V 492769 6587514 UTM
3	ERT	01.12.2016	2 m	160 m	32V 492767 6587526 UTM	32V 492882 6587625 UTM
4	ERT & GPR	28.11.2016	1.5 m	120 m	32V 492939 6587681 UTM	32V 493001 6587578 UTM
5	ERT & GPR	28.11.2016	1.5 m	120 m	32V 493048 6587742 UTM	32V 492994 6587848 UTM
6	ERT & GPR	29.11.2016	1.5 m	120 m	32V 493133 6587425 UTM	32V 493017 6587442 UTM
7	ERT & GPR	29.11.2016	1 m	80 m	32V 493314 6587459 UTM	32V 493247 6587503 UTM
8	GPR	26.04.2017	not relevant	176 m	32V 492889 6587517 UTM	32V 492850 6587346 UTM
9	GPR	26.04.2017	not relevant	38.5 m	32V 492906 6587482 UTM	32V 492878 6587509 UTM
10	GPR	09.06.2016	not relevant	100 m	32V 492920 6587703 UTM	32V 492924 6587603 UTM
11	GPR	09.06.2016	not relevant	100 m	32V 492924 6587603 UTM	32V 492928 6587503 UTM
12	GPR	09.06.2016	not relevant	100 m	32V 492928 6587503 UTM	32V 492940 6587404 UTM

All the main profiles where measured from south to north except profile 4, which was measured from north to south. All the supplementary GPR profiles was measured from north to south except profile 9, which was measured from south to north.

3   Materials and Methods

This hydrogeological survey was performed using probe drilling, and the two geophysical methods Electrical Resistivity Tomography (ERT) and Ground Penetrating Radar (GPR). ESRI's software programs *ArcMap 10.4* and *ArcScene 10.4* were used to plan the fieldwork, and organize the acquired data.

3.1   Electrical resistivity tomography

The instrument used for ERT, was an ABEM Terrameter LS from Lund Instruments AB. This survey measured 2D-Resistivity. 61 Electrodes were knocked in the ground with two deadblow hammers of polyurethane quality (figure 3-1). Four electrode cables were then rolled out, and connected to the electrodes by 63 cable jumpers (cable 2 and 3 were double jointed). The four electrode cables served as conduits for electrical current, transmitted from the terrameter. The current was led from the electrode cables via the cable jumpers, to the electrodes in the ground. Two external 12V batteries with an external battery cable provided the terrameter with sufficient power supply. Three measurement tapes and a GPS (Garmin Oregon 300), were used to prepare and record the locations of the profiles. Two cable joints were necessary to connect electrode cables 1 & 2, and 3 & 4.

This survey required high vertical resolution and sensitivity to lateral inhomogeneities, thus the protocols used was *gradient* and *wenner*, both with a spread of 4x21. The electrode spacing varied between the investigation sites. The transmitter and receiver settings are shown in table 3-1 and 3-2. The bad electrode setting was adjusted once, to 50 KOhm at profile 1 due to very high resistivity values.

The acquired resistivity data was transferred and processed further in ABEM's *Terrameter LS Toolbox* and Geotomo's *Res2dinv*. Topography was added in *Terrameter LS Toolbox* by reading elevation data from a digital elevation model in *ArcMap*. The resistivity data was inverted in *Res2dinv* by using the least-square inversion method. Cell size was also reduced to half unit spacing when the resistivity values were very high, such as in the glaciofluvial areas.

ESRI's *ArcGIS Explorer Desktop* was used to extract data from the GPS using the "add content" function, and sharing it as a layer package. It could then be stored in the GIS workspace folder, accessible to ArcMap and ArcScene.

Table 3-1. The transmitter settings for 2D-Resistivity measurements.

Minimum current	10 mA
Maximum current	200 mA
Max power	250 W
Max output voltage	600 V
Electrode test	Focus one
Bad electrode	20 KOhm
Fail electrode	300 KOhm
Electrode test current	20 mA
Advanced: Allowed power loss (25w)	25W

Table 3-2. The receiver settings for 2D-Resistivity measurements. Induced polarization (IP) was measured in addition to resistivity for all the profiles. However, it was only used to supplement the interpretation of profile 5 in this thesis.

Measure mode	RES, IP
Minimum # of stackings	1
Maximum # of stackings	1
Error limit	1.0%
Delay time	0.3 s
Acq. time	0.3 s
Number of IP windows	2
Record full wave form	no
Power line frequency	50 Hz

Figure 3-1. Electrodes knocked in the ground by Jonas Haugen at profile 3 (a kettle hole).

For detailed information on the technical aspect of the field work, refer to the user guides for the ABEM terrameter LS (ABEM Instruments AB, 2016; Arvidson & Torp, 2014).

3.2 Ground penetrating radar

GPR surveys was performed using pulseEKKO PRO equipment from Sensors & Software Inc. This survey utilized a digital video logger (DVL, model 1100) for monitoring the process and configuring the settings. A DVL carrier was used for transporting the DVL in the field. A transmitter (100 400V Transmitter) and a receiver (model 1600) were responsible for data acquisition, by sending and recording electromagnetic waves. Two fiber optic cables connected the transmitter and receiver to the DVL. 50 and 100 MHz antennas were used to transmit at different frequencies, which determined depth and resolution of the radargram. A SmartCart was used for transporting the equipment during measurement at the road. A sled replaced the SmartCart at more challenging terrains. A 12V7Ah sealed lead acid rechargeable battery provided power in the field, and was carried in a small shoulder bag. The configurations used are shown in table 7-1 – 7-5 in appendix 1.

The fieldwork consisted of running the GPR on a sled with 50 MHz antennas over the previous 2D-Resisitivity profiles (figure 3-2). 100 MHz antennas were used with a SmartCart along Gvarvikvegen 156 and in the Quarry. The terrain at the glaciofluvial deposit was challenging, and posed a harmful threat to the equipment. Hence, the glaciofluvial profiles (profile 1, 2 and 3) was excluded from GPR measurements.

The acquired data was transferred and processed further in Sensors & Software's *EKKO View* & *EKKO View Deluxe*. Distances were adjusted, and the velocity of hyperbolas (diffractions) were measured before the radargram was extracted.

Figure 3-2. GPR fieldwork with 50MHz antennas on profile 5.

3.3 Probe drilling

Probe drilling was used as a verification for profile 6 and 7. The probe drilling was performed by using a Pioner hammer drill (Atlas Copco) equipped with a drill neck (figure 3-3). Probe rods equipped with a square tip and a drive sleeve, were drilled into the ground. The process was paused every meter, where two wrenches was used to attach a new probe rod and then twist

it. The sound and the motion during the twisting revealed the soil composition at the depth of the square tip (table 3-3). The drilling time was also noted for every meter, as it can reveal the packing of the sediment (table 7-7 and 7-8 in appendix 2). The drilling stopped when an impermeable layer was located. The probe rods were lifted back up by a jack, equipped with a ball joint for clamping.

Table 3-3. Reference scheme by University College of Southeast-Norway (USN) for soil composition when probe drilling.

Clay/silt	No sound. First heavy, then easy to twist
Silt	Weak buzzing
Fine sand	Strong buzzing
Middle sand	Rubbing
Coarse sand	Strong, coarse rubbing
Gravel	Clicking
Rock	Jerky twisting

Figure 3-3. Probe drilling performed at profile 6 by Frode Bergan

4 Results and Discussion

The three first profiles occur on the glaciofluvial terrace, which very likely contain a thick, dry vadose zone. An electric current will not move easily through this area, and high resistivity values are to be expected. The *gradient* configuration gave more detailed results than *wenner*, and is thus chosen to represent most of the 2D-resistivity profiles.

4.1 Profile 1: Glaciofluvial terrace

Profile 1 is 400 meters long, and covers almost the entire glaciofluvial terrace (figure 4-1 and 2-2). The resolution suffers due to the large electrode distance, but the purpose of this profile is not to extract details, but to give a decent overview over the subsurface conditions. Greater electrode distance also increases the penetration depth, which in this case is 60 meters.
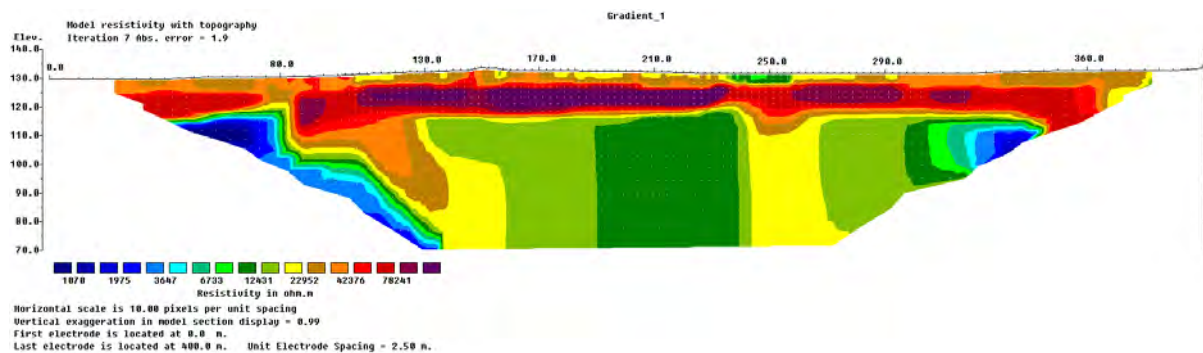
Figure 4-1. Inverted resistivity section of profile 1 (gradient).

This profile consists of enormous resistivities, and it is difficult to connect these values to specific geologic materials from prefixed tables. However, what immediately captures the attention is the highest resistivities at 115-125 masl, spreading like a red belt along the top layer. These values indicate very dry sediments. A glaciofluvial delta usually lacks clay and fine silt, and is dominated by layers of sand, gravel and cobble (jørgensen, Sørensen & Haldorsen, 2014). Topset beds contain the coarsest material (gravel, cobble or boulders), and foreset beds consist mainly of sand with minor amounts of gravel (Sutphin, Drew, Fowler & Goldsmith, 2002). The quarry at Øverbømoen confirms that this is the case for this glaciofluvial terrace.

Figure 4-2 reveals a distinct layer of cobbles and boulders appearing at the top of the terrace. The boundary between this layer and the one beneath, is plausibly the interface that creates the abrupt transition into the belt of immense resistivity values. Hence, what constitutes the belt is most likely the delta foreset bed. The porosity of sorted sand is significantly higher than for cobbles and boulders (Weight, 2008), and certainly much higher than cobbles and boulders mixed with gravel and sand. This glaciofluvial terrace is desiccated and the pores will thus contain air or other insulating gases. The high porosity in the foreset bed is thus likely what causes the pattern observed in the resistivity profile.

Figure 4-2. The quarry at Øverbømoen, revealing the topset bed with a distinct layer of boulders.

The Bø River has its highest altitude at 115 masl. Hence, significant moisture is not expected to occur until around that level. Profile 1 does reveal a massive drop in resistivity at approximately 115 masl along the profile. The intuitive impression is thus that the water table is the causing factor. However, this may not be the case. Previous drillings C3, C4 (Jansen, 1983) and supplementary GPR profiles 8 and 12, reveal bedrock close to the surface declining from north to south (figure 4-3).
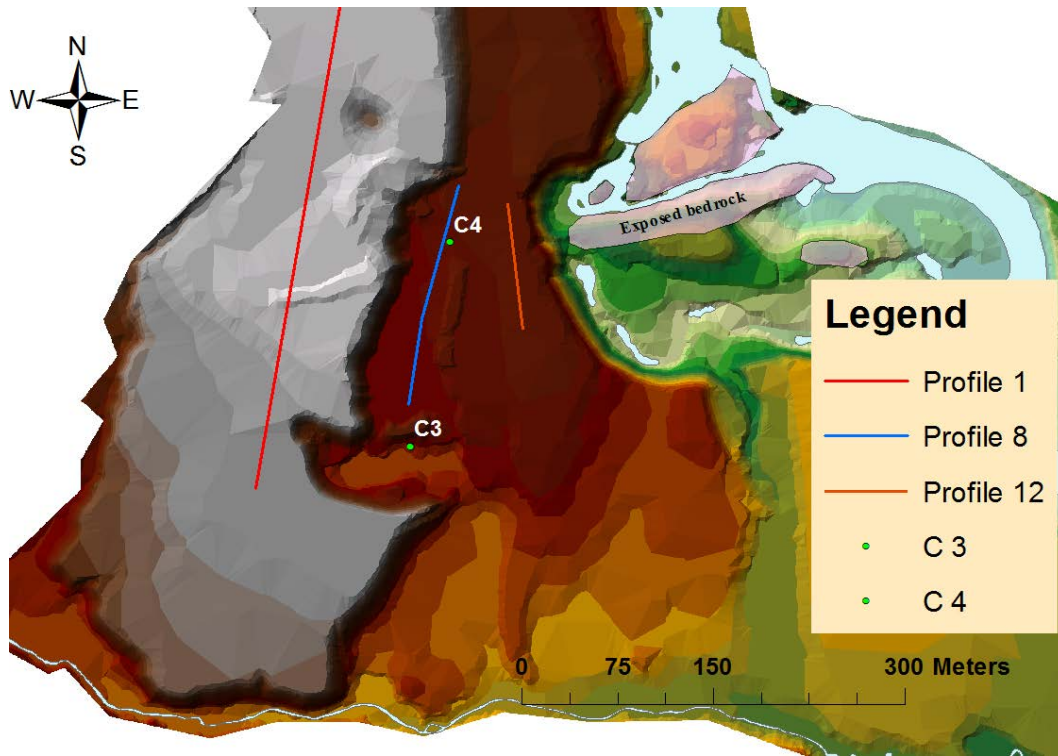
Figure 4-3. DEM of Øverbømoen showing relevant profiles (see text), previous drillings (C3 and C4) and exposed bedrock.

C4 hits bedrock at a depth of 4.5 m (117.4 masl), which matches the altitudes of the less eroded parts of the exposed bedrocks crossing over Herrefoss (the waterfall). Hence, they seem connected as the exposed bedrock is heading in the direction of the C4 drilling. If the direction continues from C4 towards the esker and profile 1, then the mid-section (130-240 m, below 115 masl) of profile 1 is not saturated zone, but granitic gneiss bedrock. The resistivity values of the mid-section range from approximately 7000 to 20 000 Ωm. These values seem too high to assume a water table. However, the values could potentially correspond to granite (table 1-6).

Supplementary GPR profiles 8 and 12 confirms that a bedrock might be the case. C4 is located at a 5.5 m distance perpendicular at approximately 45 m in profile 8 (figure 4-4), where the bedrock appears to be at a depth of 6 m (114 masl) (figure 4-4 and 4-5). While at profile 12, C4 lies at a 48 m distance perpendicular at approximately 25 m, where the bedrock appears to be at a depth of 4.5 m (118.5 masl) (figure 4-6). Previous drilling C3 hits bedrock at a depth of 28.2 m (91.6 masl), which corresponds with the declining bedrocks observed in profile 8 and 12 (figure 4-4 and 4-6).
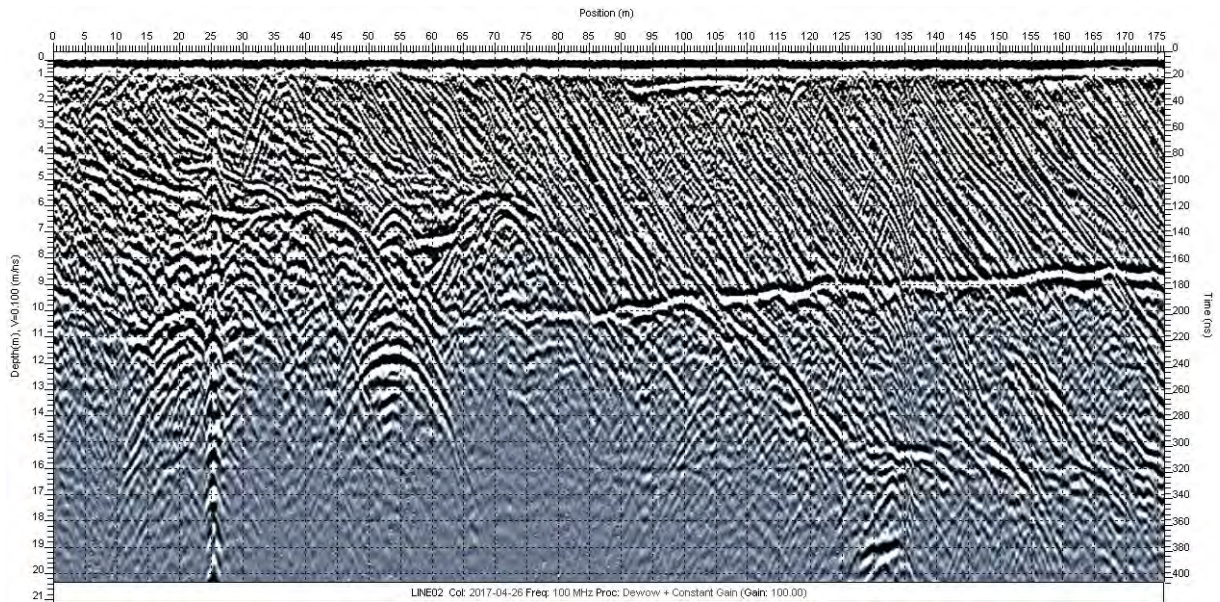
Figure 4-4. 100 MHz Radargram of supplementary profile 8. The longitudinal compression gives the illusion of a steep slope in the delta foreset bed. The angle is 21.8° at 80-90 m, and declines to 16.7° at 164-174 m.
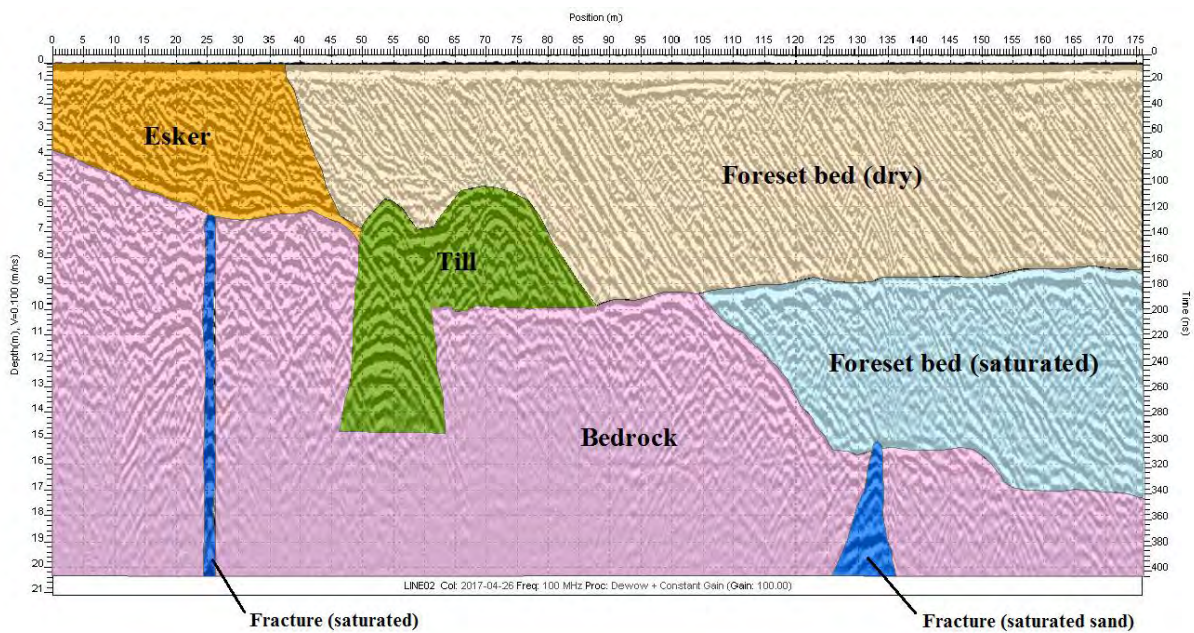

Figure 4-5. Interpreted radargram of profile 8, based on table 1-9 (Reynolds, 2011) and figure 1-17 (Beres & Haeni, 1991). There is uncertainty whether the till is rather a fracture or something else. See table 7-11 in appendix 4 for the velocities of the relevant features.
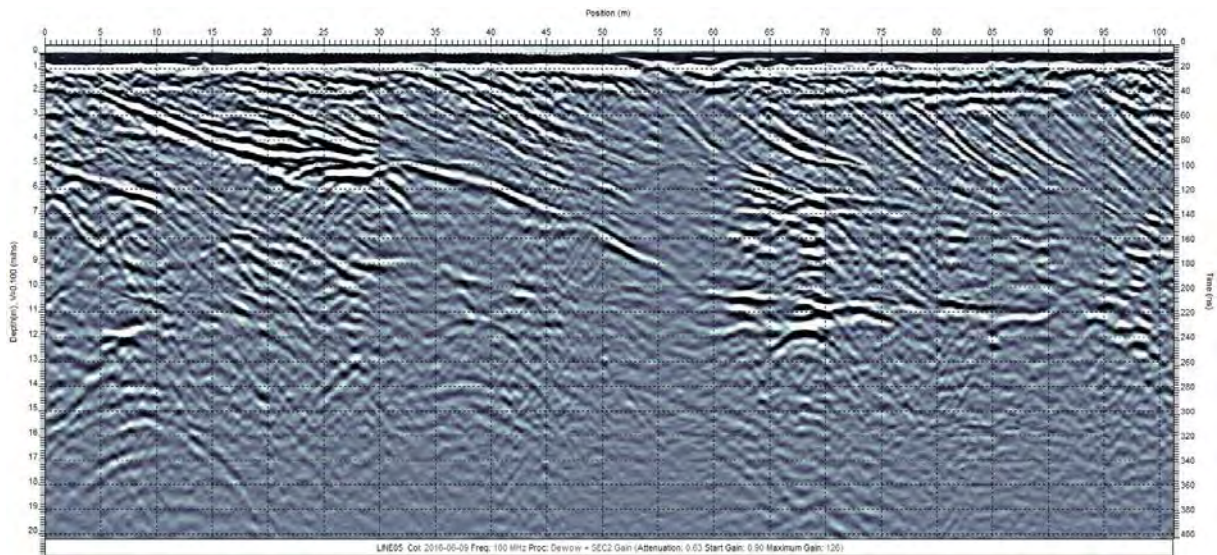
Figure 4-6. 100 MHz radargram of profile 12. The coherent reflection starting at 2 m depth at the beginning, and ending at approximately 11-12 m depth at the end is interpreted to be bedrock.

Hence, it is reasonable to assume the mid-section (130-240 m, below 115 masl) of profile 1 to be the bedrock. In addition, the way the surrounding layers appears to curve around this mid-section also gives the impression of a solid object (figure 4-1). At 250 m, the red belt of high resistivities starts to decline as it moves left, but is "pushed up" again at 240- and 260 m. This also indicates that the right-section (270-350 m, below 115 masl) is bedrock, as its resistivity values equals the mid-section. Hence, it seems to be a fracture occurring at 240-270 m. A fracture like this, moving vertically with a consistent resistivity value, does not indicate the presence of a water table. From 130 to 80 m the red belt of high resistivities start to decline again, which could be a consequence of not being supported by a solid bedrock.

Loke (2011) shares a similar incident from the Bauchi area in Nigeria (figure 4-7). The result is from a survey that mapped fractures with groundwater in a hard-rock environment.
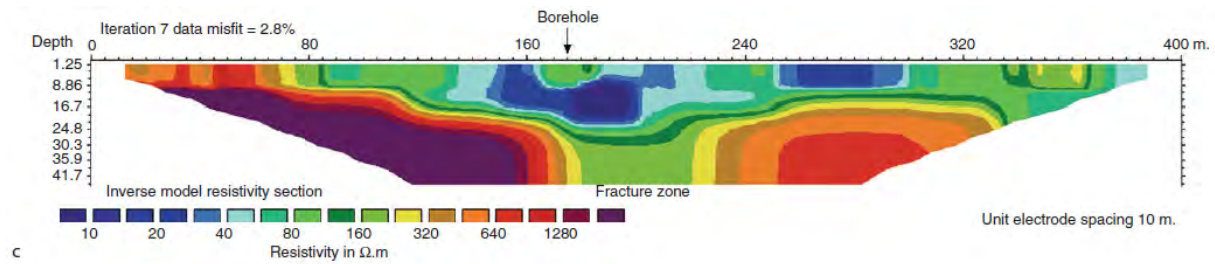
Figure 4-7. Resistivity section of a groundwater survey in the Bauchi area, Nigeria (Loke, 2011). The high resistivity sections at each side of the fracture zone are bedrocks.

Figure 4-7 reveals the firmness of the bedrocks by showing how the surrounding resistivity-sections are "forced" to curve around them. Also, note how the dark green layer (160 Ωm) declines in the fracture zone. Solberg et al. (2011) also show the same phenomenon (figure 4-8), where surrounding layers experience full stop and must curve around the bedrock.
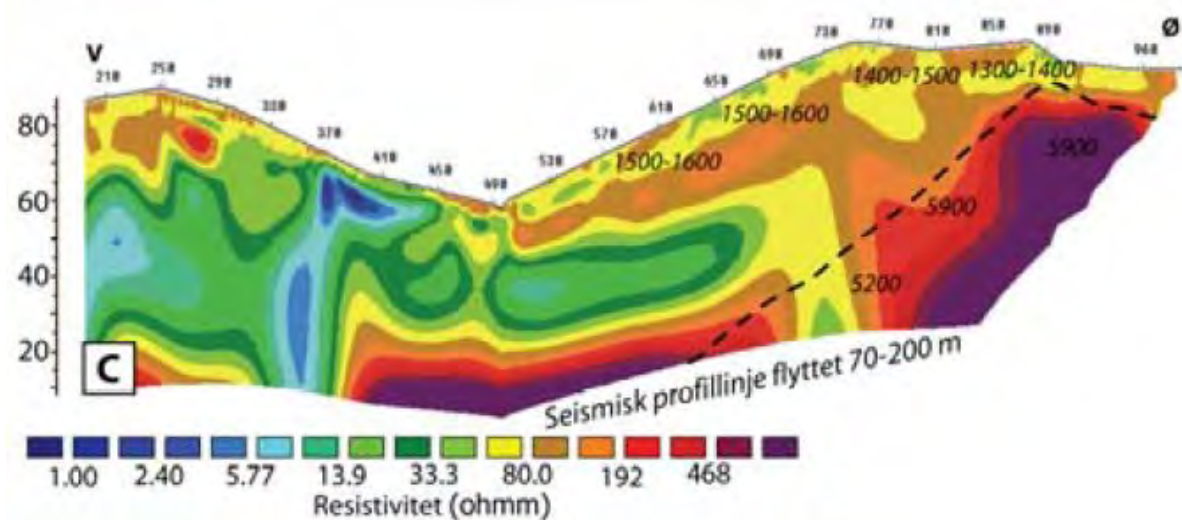
Figure 4-8. Resistivity profile from Rødde, Sør-Trøndelag. Bedrocks are recognized as the high resistivity areas at the bottom mid-section and right-section (Solberg et al. 2011).

At both edges of profile 1 (figure 4-1) there appears low-resistivity-bodies. Whether the body in the right section (330 m) is a fracture in the bedrock is difficult to say as it is at the edge of the model. The body in the left section (40-130 m) is more interesting as it appears to be part of a larger body. At 50 m the resistivity drops from approximately 80 000 Ωm at 120 masl, to 1000 Ωm at 110 masl. This is the largest resistivity contrast in the profile, and is a strong indication of moisture. It could indicate a transition into a saturated zone, but more coverage

47

is necessary in order to conclude on this. Profile 8 (figure 4-5) however, reveals water table hitting the declining bedrock at 105 m at a depth of approximately 10 m (110 masl). This means that the water table covers the first 70 m of profile 8, starting from south (figure 2-2). There seems to be a connection at around 110 masl between profile 1 and profile 8. Hence, the low resistivity body at the left section of profile 1 might be the beginning of an aquifer.

More investigation is necessary in order to determine what is causing the decline in resistivity at around 115 masl of profile 1. Probe drilling and GPR would sufficiently assist the interpretation. More coverage of the southern end of the deposit is also desirable in order to make conclusions about a potential aquifer. However, the saturated foreset bed in profile 8 looks promising, and could potentially be an excellent source of water supply (figure 4-5).

4.2 Profile 2: Esker

Profile 1 contained an esker at 150 m, but it was only visible topographically due to the poor resolution of the profile. Profile 2 is a 160 m-long resistivity section of the same esker at a higher resolution (figure 4-7). Eskers are valuable targets when prospecting for groundwater, as they contain well sorted glacial deposits (Weight, 2008; Fetter, 2001). Unfortunately, they are topographically high and often unsaturated (Fetter, 2001). If they are found buried however, they can be excellent sources of groundwater (Fetter, 2001).
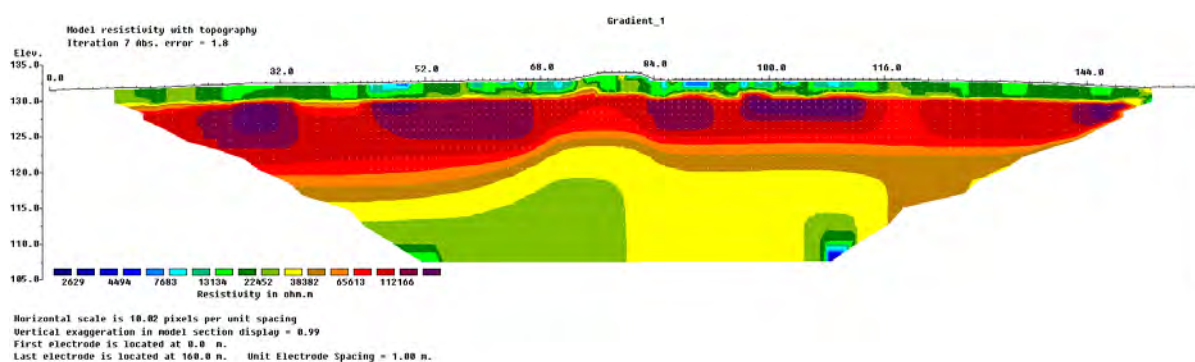

Figure 4-7. Inverted resistivity section of profile 2 (gradient).

This profile is positioned almost parallel to profile 1, hence the same pattern occurs, but with more detail and less depth penetration. The red belt of enormous resistivities appears again, but now even higher resistivity-segments can be distinguished within it. These high resistivity-

segments could be sections of higher porosity, but they could also be sections mixed with boulders of high resistivities. The plausible bedrock appears at 115 masl as in profile 1, but with a higher resolution this time. It is difficult to determine whether it is the yellow- or green layer representing the bedrock. It also might not be bedrock at all.

The esker reveals itself from 68 - 84 m with distinct layers forming a ridge. It is significantly larger than it appears on the surface, with a depth of approximately 17 meters. What is interesting about this ridge is how the layers evenly spread out laterally, aligning with the delta deposit. This reinforces the observation made in figure 1-6, that this part of the glaciofluvial delta emanated from the west, and not north as Jansen (1983) suggests. If so, then the resistivity section of profile 2 (figure 4-7) is heading towards the reader.

If Jansen (1983) is right however, and the delta did emanate from the north, an interesting theory appears regarding the esker. If the green layer right under 115 masl is bedrock, and there is a fracture occurring from 80 m, then the bedrock could be responsible for the formation of the ridge. In this case, the delta is heading left in figure 4-7, and the fracture is filled with delta deposit. The delta deposit must then curve around the shape of the bedrock, creating a ridge form. Successive layers then curves around the layers beneath, enlarging it to the form visible today. If this is the case, then the ridge is not an esker, but an accumulation of successive delta layers. However, his seem unlikely based on how tall and distinct the ridge appear.

An esker is usually formed in subglacial meltwater-tunnels, and its structure is based on the form of the tunnels (Jørgensen et al., 2014). Tall and narrow subglacial tunnels produce eskers with clearly marked ridge forms (Jørgensen et al., 2014), such as the one in this profile. Hence, the theory of western origin seems more plausible in terms the esker formation. However, profile 8 (figure 4-4) clearly indicate a delta foreset bed heading from north to south, making the formation of the esker seem like a process that occurred before the delta-formation.

The purpose of this profile was to get a more detailed image of the esker, and hopefully locate parts of it immersed in saturated zone. But after interpreting profile 1, it appears the esker is not advantageously positioned in terms of groundwater supply. However, more research is necessary to conclude on this. A probe drilling would suffice in order to determine whether it is bedrock at 115 masl or not.

A supplementary GPR profile was taken to investigate the direction of the esker (figure 4-8 and 4-9).
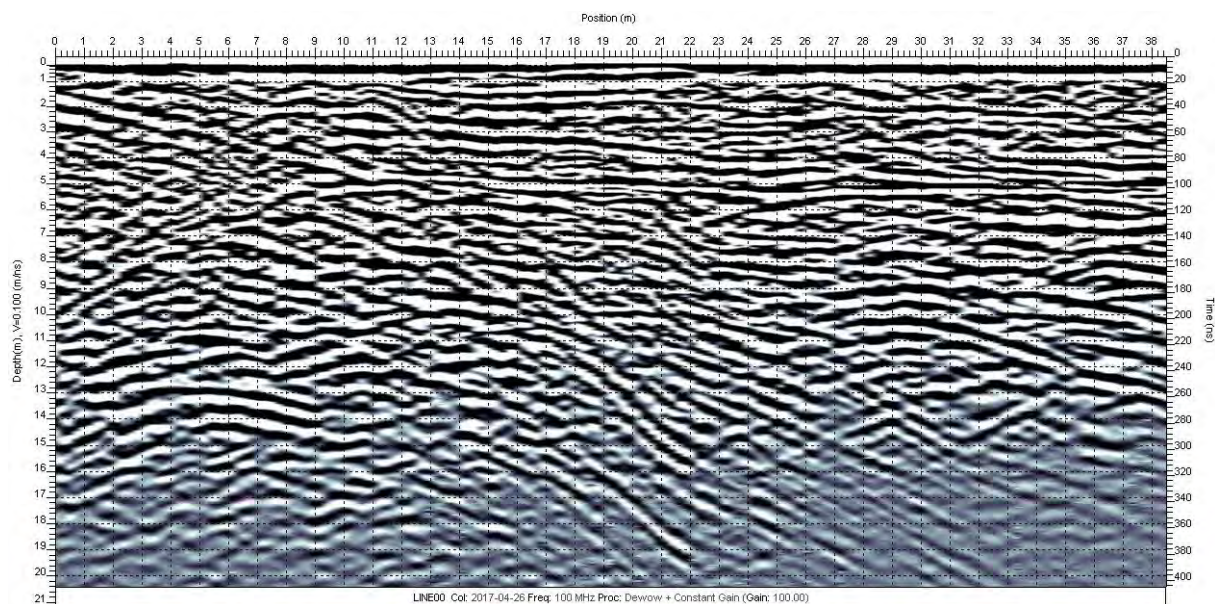

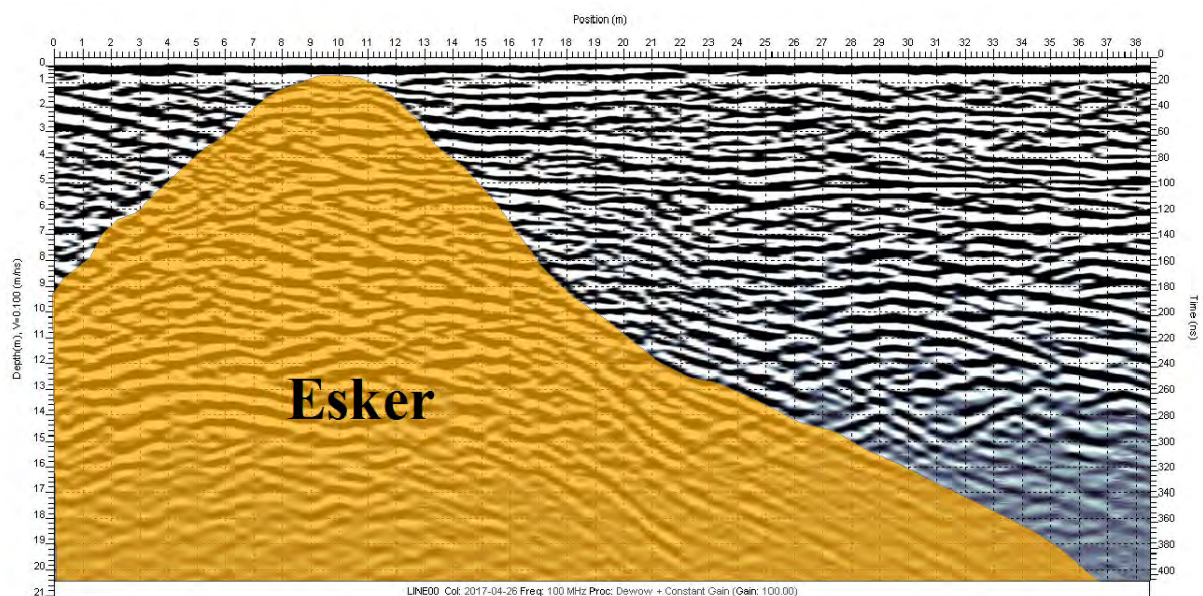*Figure 4-8. 100 MHz radargram of profile 9. A ridge form can be observed to the left.*

Figure 4-9. Interpreted radargram of profile 9. The bedrock boundary has been ignored here, as the purpose was to explore the direction of the esker.

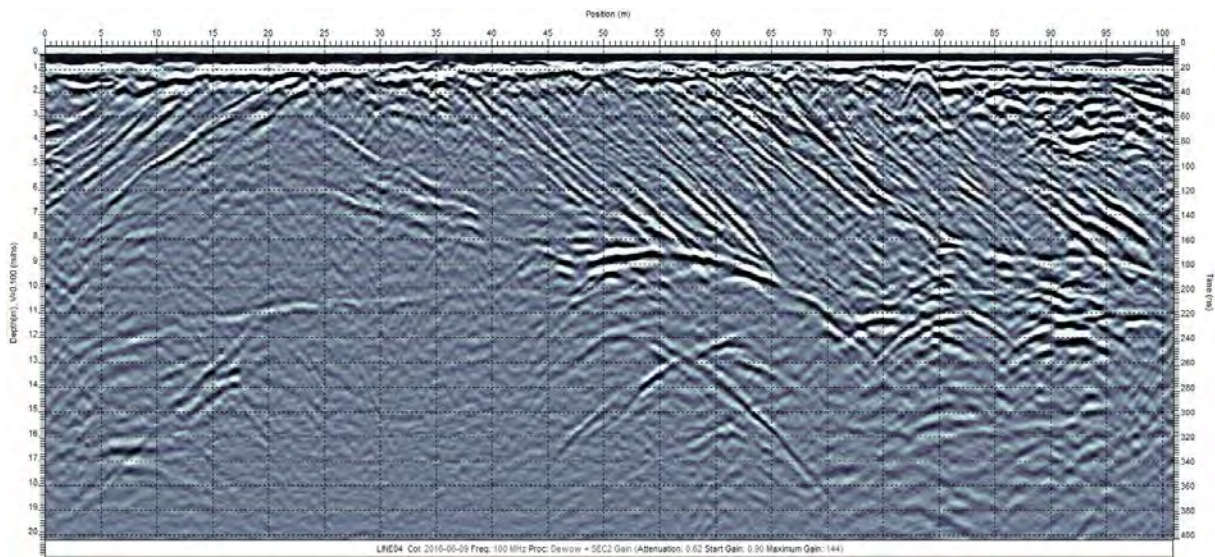Hints of the esker are also observed in supplementary profile 11 (figure 4-10). It seems to have shrunken in size at this point.

Figure 4-10. 100 MHz radargram of supplementary profile 11. Hints of esker visible at 95 m at 2-4 m depth.

Based on the GPR-profiles 8, 9 and 11, it appears the esker heads toward the exposed bedrocks at Herrefoss (figure 4-11).
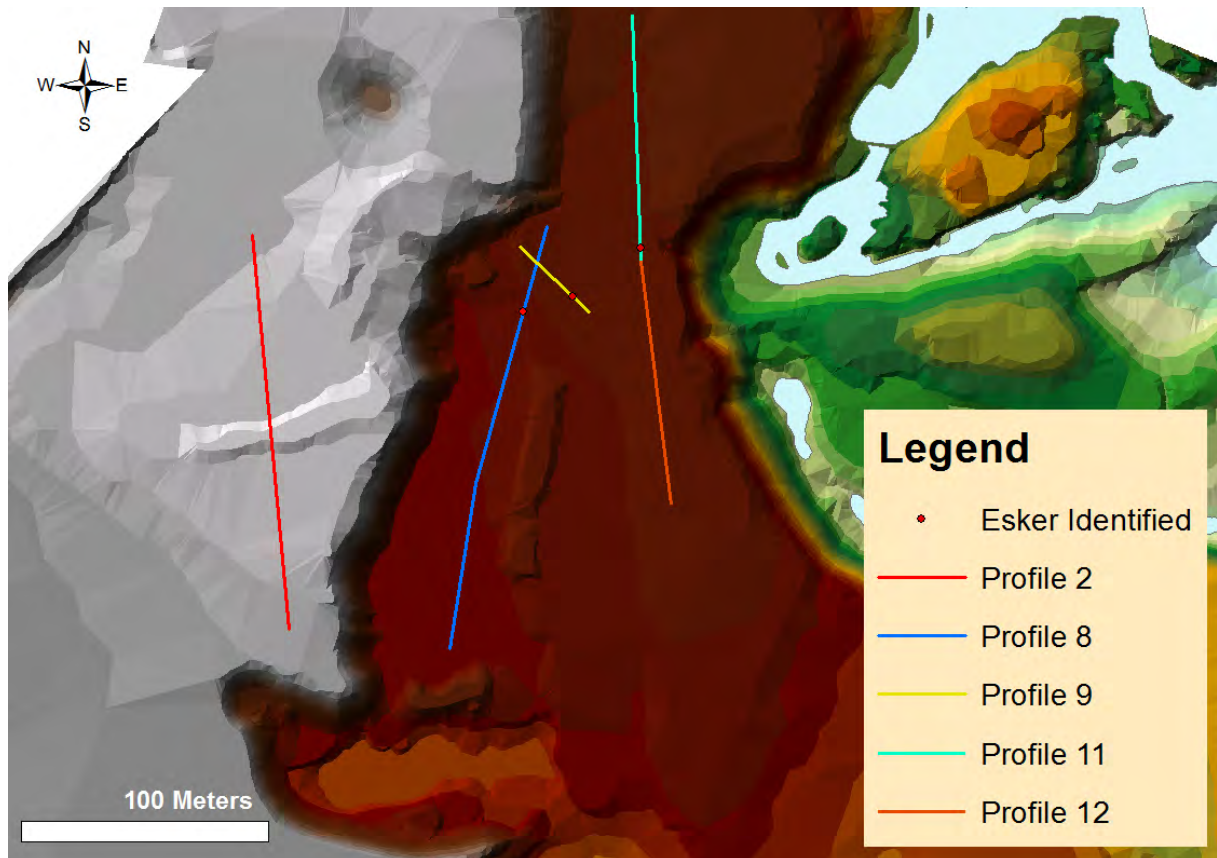
4.3 Profile 3: Kettle hole

Profile 3 is a 160-m resistivity section of a kettle hole. A kettle hole is a large pit that is formed when big ice blocks is left behind and buried in front of a melting glacier (Jørgensen et al., 2014). When the big ice block melts, a large pit is formed (Jørgensen et al., 2014). The kettle hole is topographically outlined in profile 3 and is clearly seen from 52 m to 84 m (figure 4-12).
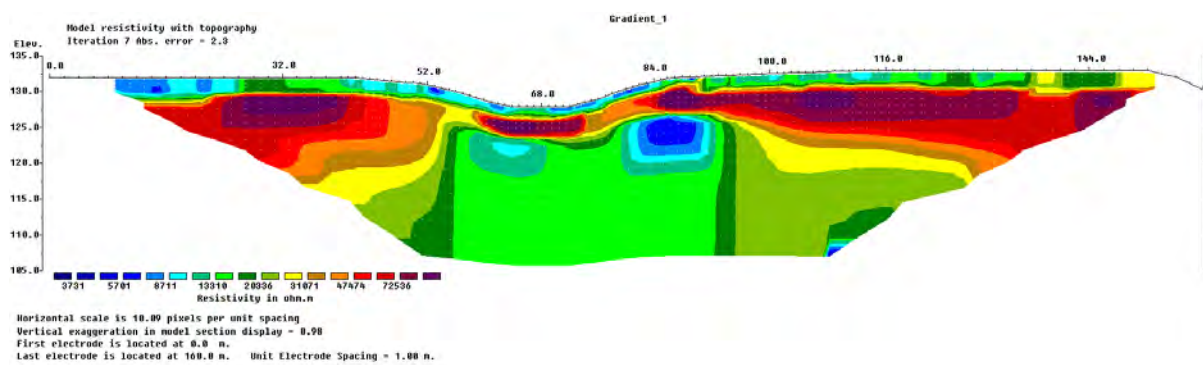

Figure 4-12. Inverted resistivity section of profile 3 (gradient).

The pattern is similar to profile 1 and -2, with the high resistivity belt occurring at the top layer. However, this time the belt does not spread in a straight horizontal line. It spreads obliquely at both sides of the kettle hole, which seems to be caused by what appears to be a bedrock. From 55-92 m right below the kettle hole at 125 masl, is a square structure with a resistivity value (approximately 13 000 – 20 000 Ωm) corresponding to the plausible bedrock in profile 1. The square structure gives off a firm homogenous impression, and the high resistivity belt seems to adapt and curve around it. If the delta originated from the west (left in the profile), it could seem like it collided with the bedrock at 55 m. The bedrock then forced it to curve upwards and around it. If the delta originated from the north then it came towards the reader, engulfing and adapting to the shape of the bedrock. That may seem more reasonable considering how coherent the layers appear across the bedrock.

The bedrock appears to have a significant fracture at 84 m at 125 masl. It may contain moisture as the resistivity drops significantly. Loke (2015) shares an example of fractures filled with

52

groundwater (figure 4-13). The survey took place in a hard-rock environment in the Blue Ridge mountain area in eastern USA.
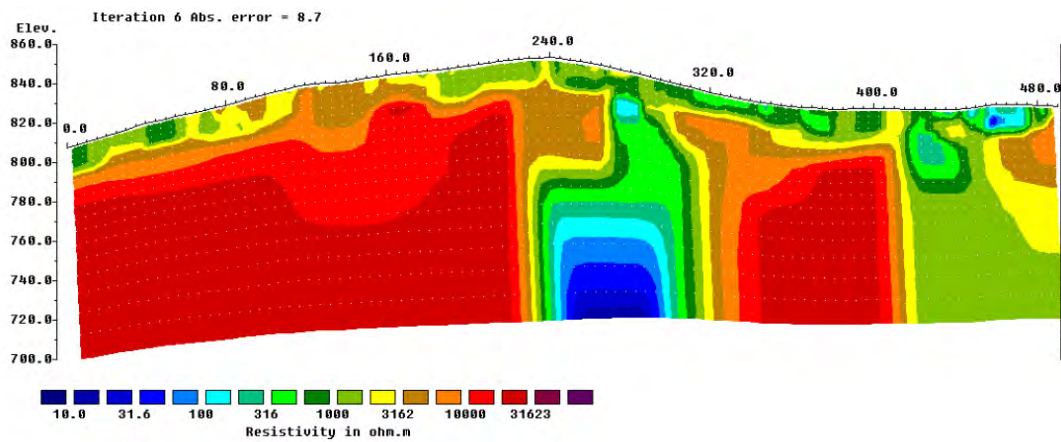

Figure 4-13. A fracture of groundwater (blue segment starting at 240 m) in a hard-rock environment (red sections with high resistivities) (Loke, 2015).

Figure 4-13 displays the fracture in a circular shape of decreasing resistivities, similar to the fracture observed in profile 3 (figure 4-12).

However, there are little signs of saturated zones in this profile. Hence, it does not seem to be an optimal location for groundwater supply. It seems the northern part of the glaciofluvial terrace is highly drained.

4.4 Profile 4: Fluvial terrace

Profile 4 covers 120 m of the fluvial terrace deposit (figure 4-14). Fluvial erosion, transport and sedimentation shape the landscape, and is extensively responsible for the sediment distribution (Jørgensen et al., 2014). Fluvial deposits are important groundwater reservoirs in many valleys in Norway (Jørgensen et al., 2014). Jansen (1983) estimates the thickness of this fluvial deposit to be at least 5 m.
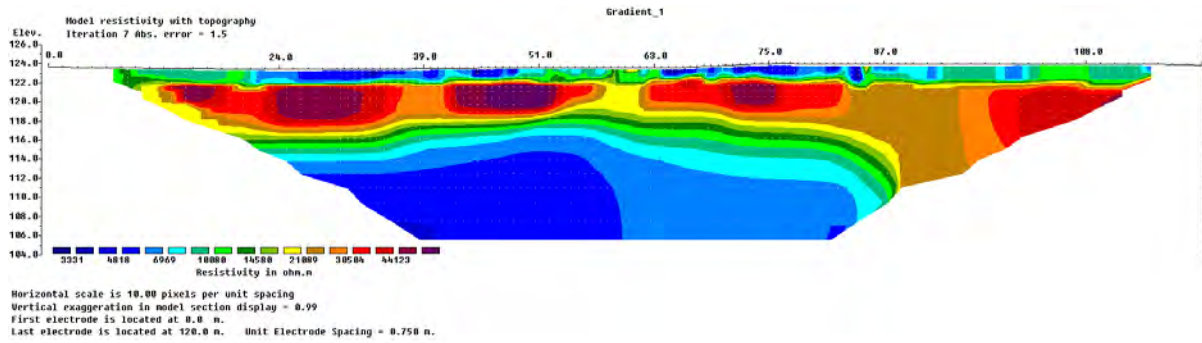
Figure 4-14. Inverted resistivity section of profile 4 (gradient). This profile was measured from north to south. Hence, potential delta structures will likely show a direction from left to right.

The subsurface pattern in this fluvial deposit is similar to the glaciofluvial profiles. A red belt of enormous resistivities appears again at the top section, though not as extreme in its values. The immediate suspicion is thus that a foreset bed is stretching along the profile.

Profile 4 is located closer to the Bø River (figure 2-1), and it appears to be an interaction occurring. The river is situated approximately 60 m east of the profile, at 115 masl. This seems to have a major impact on the resistivity results. At 115-116 masl, the resistivity starts to decrease massively. From 119- to 113 masl at 51 m, the resistivity falls from approximately 50 000- to 3 000 Ωm. That is a massive contrast indicating saturation/moisture. A resistivity value of 3 000 Ωm does not correspond to saturated sediments (Reynolds, 2011; Solberg; 2011; Jeppson & Dahlin, 2016), but as Jeppson & Dahlin (2016) emphasizes, the resistivity must be interpreted according to the surrounding environment, not prefixed tables. In this case, there are no signs of bedrock or other structures that might cause the decrease in resistivity. A previous probe drilling from 1979 (Jansen, 1983) is located at 81 m, and indicates a thickness above 19 m (figure 4-15).
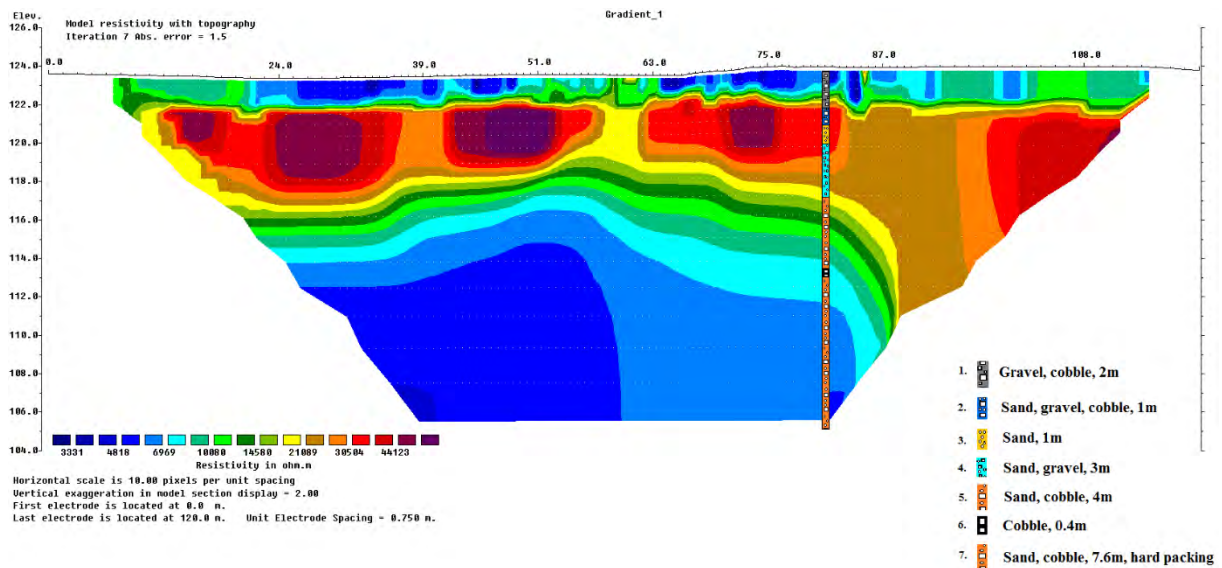
Figure 4-15. Inverted resistivity section of profile 4 with previous probe drilling at 81 m (Jansen,1983).

The sorting of the sediment is not optimal, and contains mostly sections mixed with sand, gravel or cobble. At the bottom is a mix of sand and cobble with hard packing which is not ideal at all. However, the drilling is placed in an area where the resistivity bends, which gives the impression of something confining the moisture. It is plausible that this could be an area of hard packed material. It seems to be better sorting conditions at the left section of the profile.

The radargram of profile 4 clearly supports the idea of saturation, by revealing what appears to be the water table at 114 masl (figure 4-16). The radargram also confirms the suspicion of a delta foreset bed, moving from north towards south.
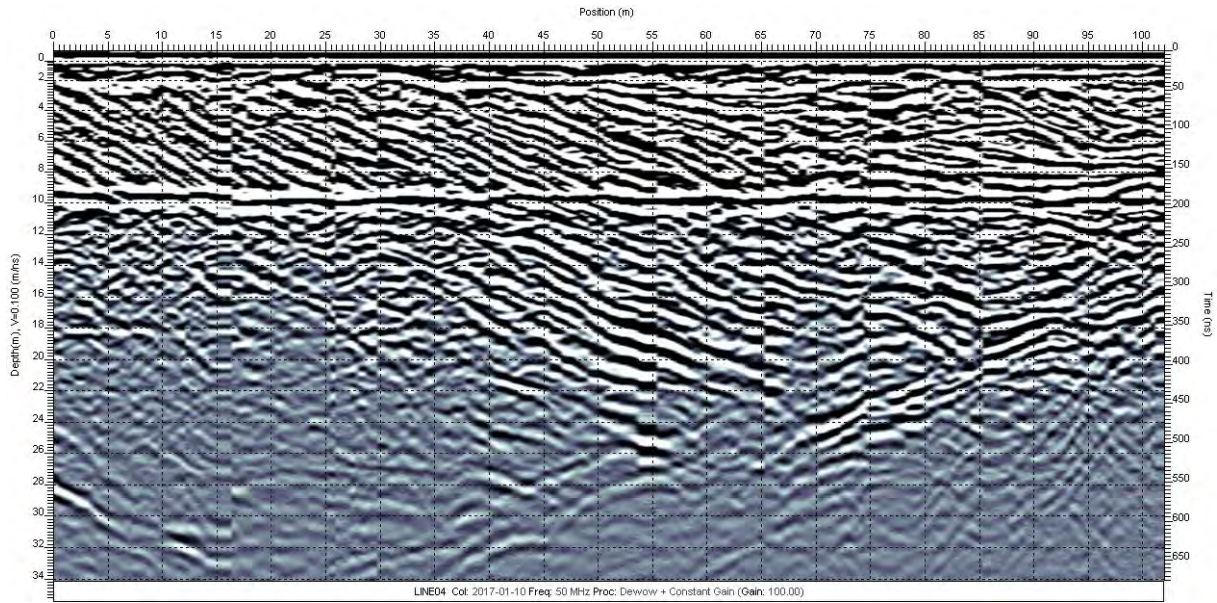
Figure 4-16. 50 MHz radargram of profile 4. The slope of the foreset bed tilts 18.43°. Note the water table at 10 m depth (114 masl).

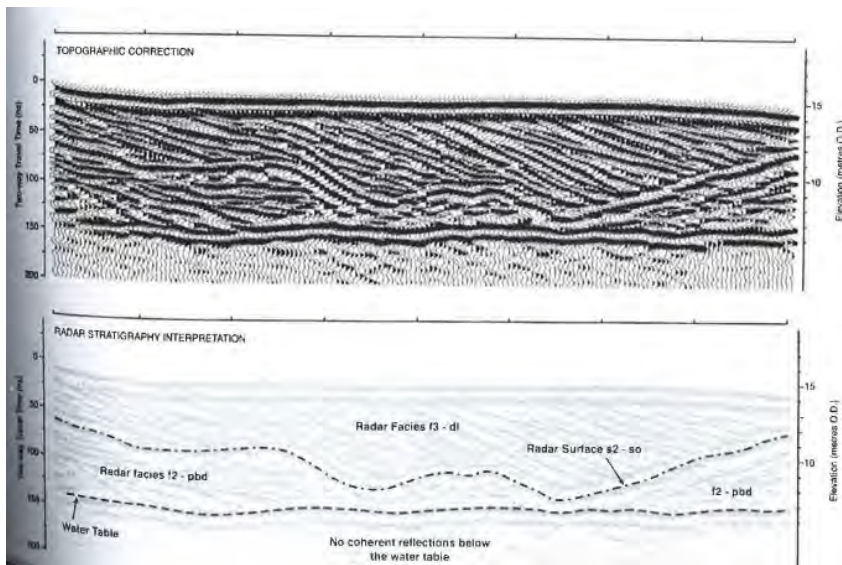Reynolds (2011) shows a radargram that outlines the water table in a similar way (figure 4-17).

Figure 4-17. Radargram and interpretation for a 100 MHz over a large coastal through blowout at Raven Meols, northwest England (Reynolds, 2011). Notice how the water table is reflected.

The water table observed in the radargram of profile 4 corresponds very well with the river elevation (115 masl). Supplementary GPR profile 10 lies approximately 20 meters west of profile 4, and captures the same phenomenon (figure 4-18). Hence, it seems reasonable to assume a water table at 10 m depth in profile 4.
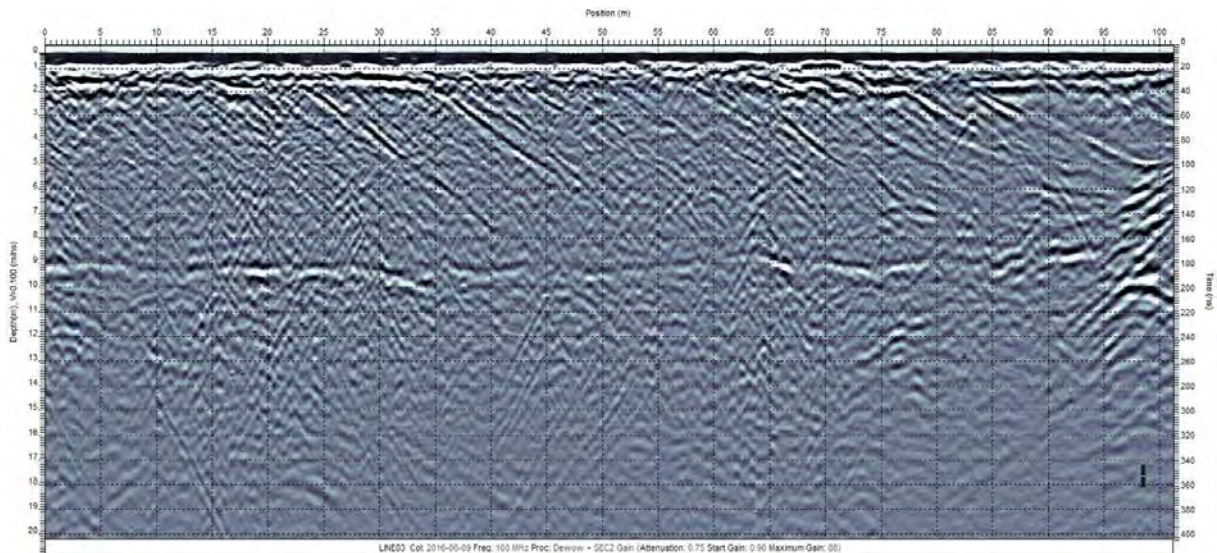

Figure 4-18. 100 MHz radargram of supplementary profile 10. Note the water table at 9 m depth.

The delta foreset bed seems to dominate profile 4 (figure 4-16), which potentially makes it an appealing aquifer. However, there is loss of signal at the bottom section, which indicates the presence of bedrock. Absorption of signals by clay content is unlikely, as this part of the delta is close to the ice contact zone. Besides, the bedrock was partly exposed at the bottom of the terrace, southeast of the profile. The bedrock seems to be causing a deflection at 70 m at 21 m depth. The foreset bed suddenly flattens out and bends in the opposite direction. The previous probe drilling is located right in the middle of this deflection, which may contribute to the hard packing of the sediments (figure 4-19). This deflection could also be connected to the bending at approximately 87 m in the resistivity profile (figure 4-14).
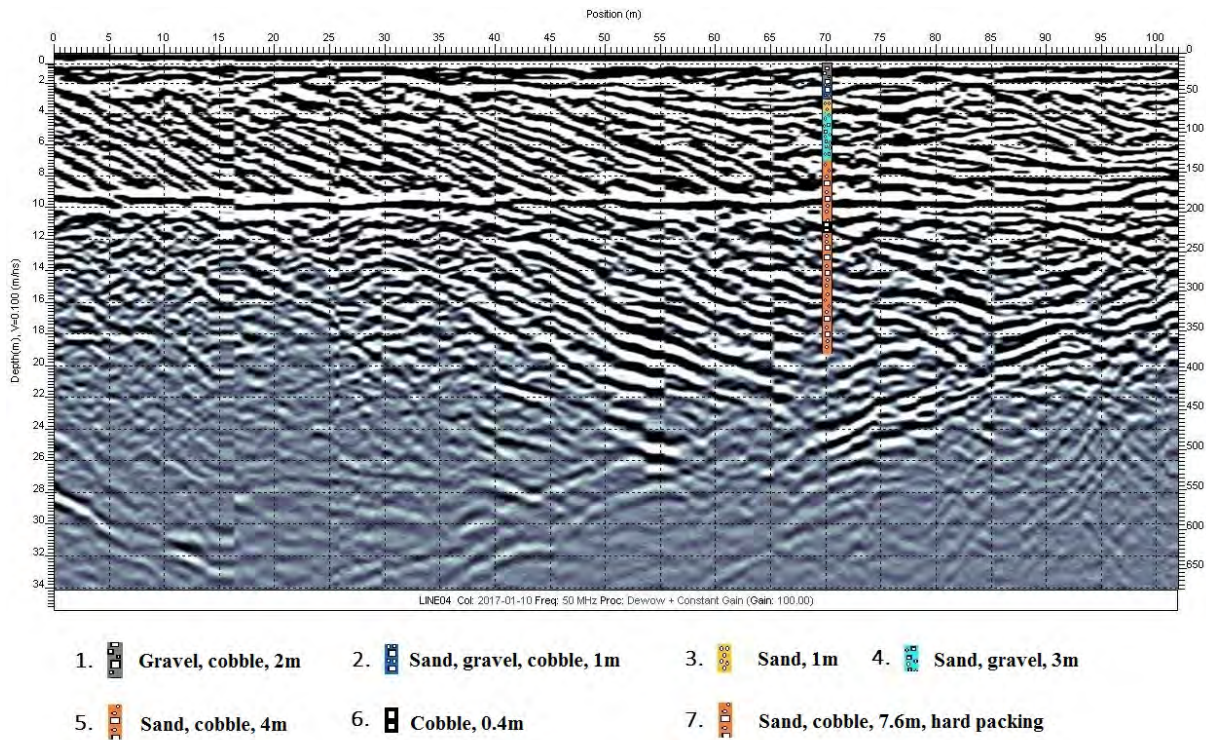
Figure 4-19. 50 MHz radargram of profile 4 with previous probe drilling from Jansen (1983). The drilling point (70 m) does not correspond with the drilling point in the resistivity profile (81 m), because the GPR profile did not cover the entire profile length due to difficult terrain (see appendix 5).

It appears to be some ridge-structures from 5- to approximately 40 m, right under the water table. They possess velocities of 0.081 m/ns and 0.107 m/ns, which correspond to moraine (Reynolds, 2011). However, this is in saturated zone which significantly decreases velocity values of electromagnetic waves (Annan, 2003). Hence, the interpretation of velocity values must be considered with caution.

However, considering the ridges and the deflection, the optimal area for groundwater prospection seems to be between 45 and 65 m (figure 4-20). This area seems to consist of mainly foreset bed, laid out in a sorted manner.
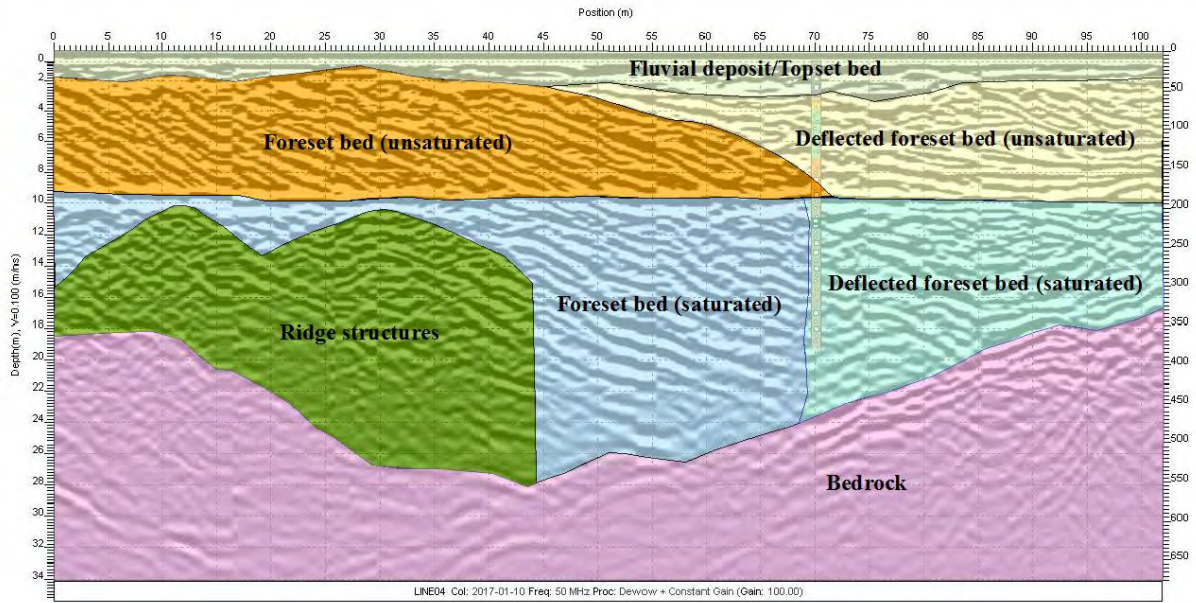
Figure 4-20. Interpreted radargram of profile 4. There is uncertainty regarding the ridges. See table 7-12 in appendix 4 for the velocities of the relevant features.

4.5 Profile 5: Along the river

Profile 5 covers 120 m and is located in fluvial deposits along the Bø river (figure 4-21). Across the river opposite of the profile, is a massive kettle hole that has been cut off by erosion (figure 4-22). Hence, a secondary objective was to observe if there were any traces of this kettle hole in the buried glaciofluvial deposits. Jansen (1983) estimates the thickness of the fluvial deposit to be 1 m in this area.
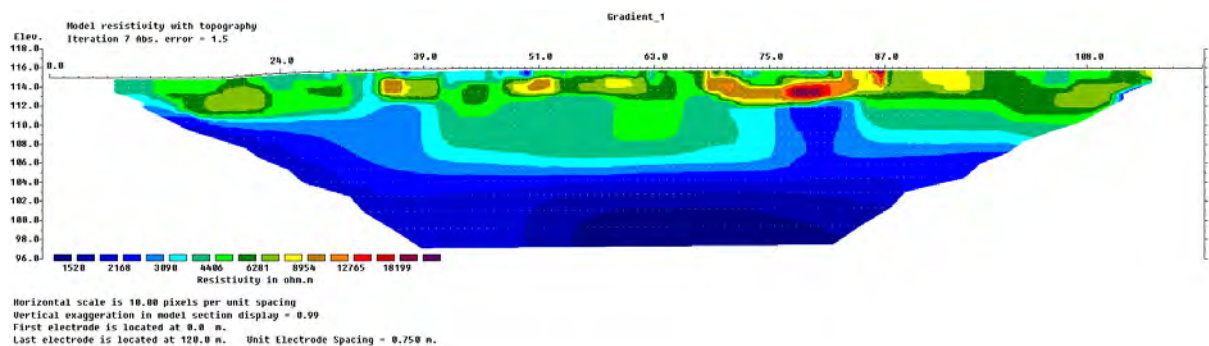

Figure 4-21. Inverted resistivity section of profile 5 (gradient).

Figure 4-22. A massive kettle hole across the river opposite profile 5.

What immediately captures the eye is the pit-form, appearing in the mid-section from 39- to 75 m. Whether this is connected to the kettle hole on the opposite side is uncertain, but it is an indicative pattern. What also captures the attention, is the small segment of high resistivity (ca. 18 000 Ωm) at 78 m. This could be larger materials such as cobbles or boulders, but it could also be underground caves used by animals. Caves will reveal itself as high resistivity sections on a resistivity profile (Loke, 2015).

Profile 5 illustrates Jeppson & Dahlin's (2016) point regarding interpretation of resistivity profiles based on prefixed resistivity tables. Profile 5 shows significantly lower resistivities than all the previous profiles, but the values are still too high to correspond to the features of the observable environment. The river is flowing right next to this profile at approximately 114 masl. Thus, the water table should be about the same elevation in the profile. However, the water table is not apparent, and the resistivity values are too high to correspond to saturated materials. Jeppson & Dahlin (2016) are thus emphasizing that interpretation must be done carefully, and the environment must be given a higher priority than tables with prefixed resisitivity values. Hence, the water table is likely at 114 masl, even though the resistivity profile does not show it.

Induced polarization was also measured for this profile, and gave an interesting pattern (figure 4-23). Induced polarization (IP) is the ability of a material to store electricity, measured in chargeability (milliseconds after the current is turned off) (Weight, 2008). IP could thus be useful in situations where ERT cannot distinguish layers due to materials with similar resistivities, but which might have different chargeabilities (Weight, 2008). Water corresponds

to a chargeability of 0 msec (Jeppson & Dahlin, 2016), thus the closer to zero, the higher the indication of saturation.
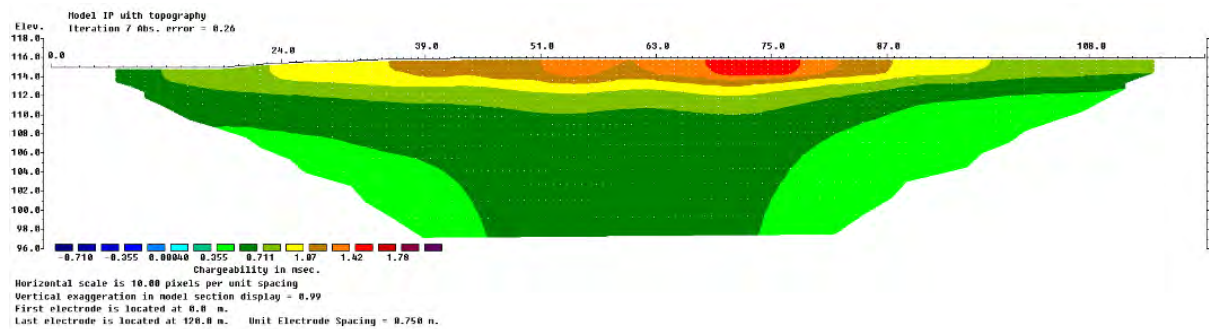

Figure 4-23. Induced polarization of profile 5.

The IP-profile appears to pick up a dark green layer (0.711 msec) that could potentially correspond to the water table. The beginning of the profile was topographically the lowest point, and the first electrodes was approximately at the same elevation as the river. This may explain why the dark green layer is part of the surface at the beginning of the profile.

What is also interesting about the IP-profile is that it reveals a pattern indicative of the presence of a kettle hole. At the same sequence as the resistivity profile shows the pit-form (39- to 75 m), there appear to be a large pit in the IP-profile. If the kettle hole is the cause is uncertain, but both profiles indicate a distinct geologic phenomenon from 39- to 75 m.

The GPR-profile however, does not reveal any structure that could resemble a kettle hole (figure 4-24). It does however; seem to reveal the water table at approximately 1 m depth, which corresponds to the river elevation.
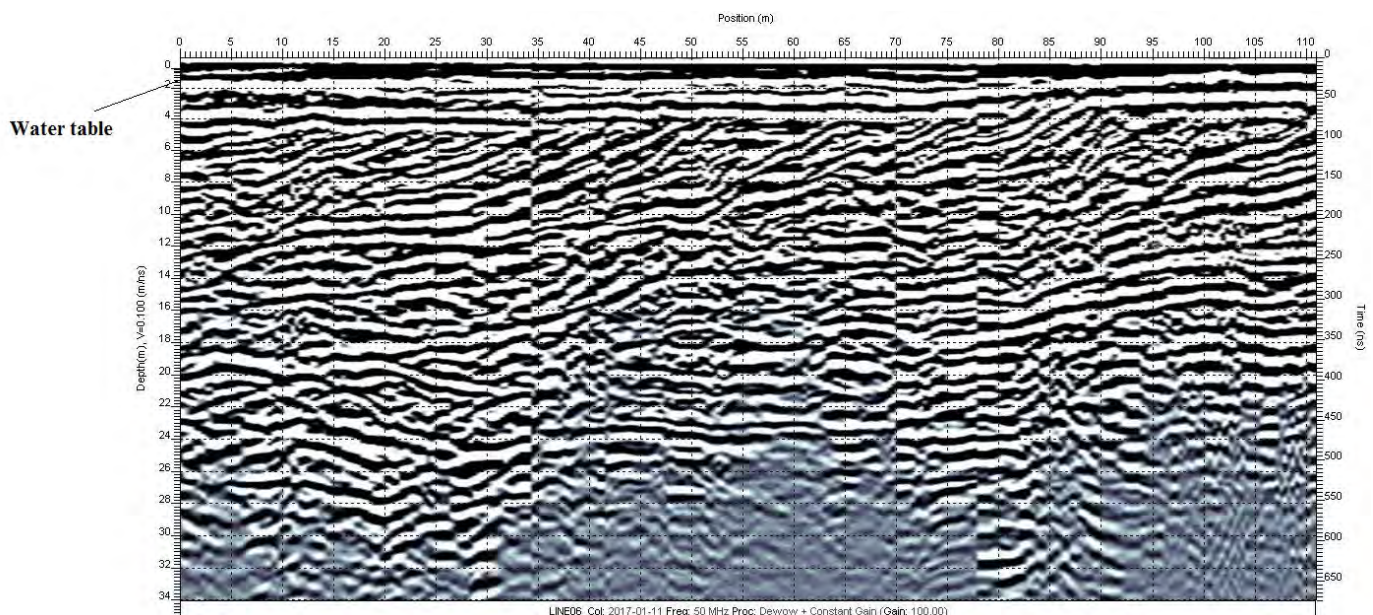
Figure 4-24. 50 MHz radargram of profile 5. It appears delta structures dominate this profile.

The radargram reveals profile 5 to be a thick delta-structure. Hence, this is a promising candidate in terms of water supply, and a probe drilling in this area is desirable. The topset bed/fluvial deposit is clearly defined by a coherent horizontal reflection starting at 4 m depth (111 masl). 111 masl is also approximately where it appears a significant resistivity contrast in figure 4-21. Below 4 m depth is the foreset bed (oblique clinoforms), stretching down to a depth of approximately 18-19 m. From there, the bottomset bed covers the rest down to bedrock, which is approximately where the signals become poor (figure 4-25). Finer material like silt and clay, often constitute bottomset beds (Sutphin et al., 2002). However, that is not likely the case here, as profile 5 is the profile that is closest to the ice contact zone. Previous probe drilling C6 (1975) lies approximately 30 m west of profile 5. It revealed the area to contain mixtures of sand, gravel and cobble down to a depth of 18 m, where it hit cobbles with hard packing (table 7-9, appendix 3). Hence, finer material is not likely contained in profile 5.
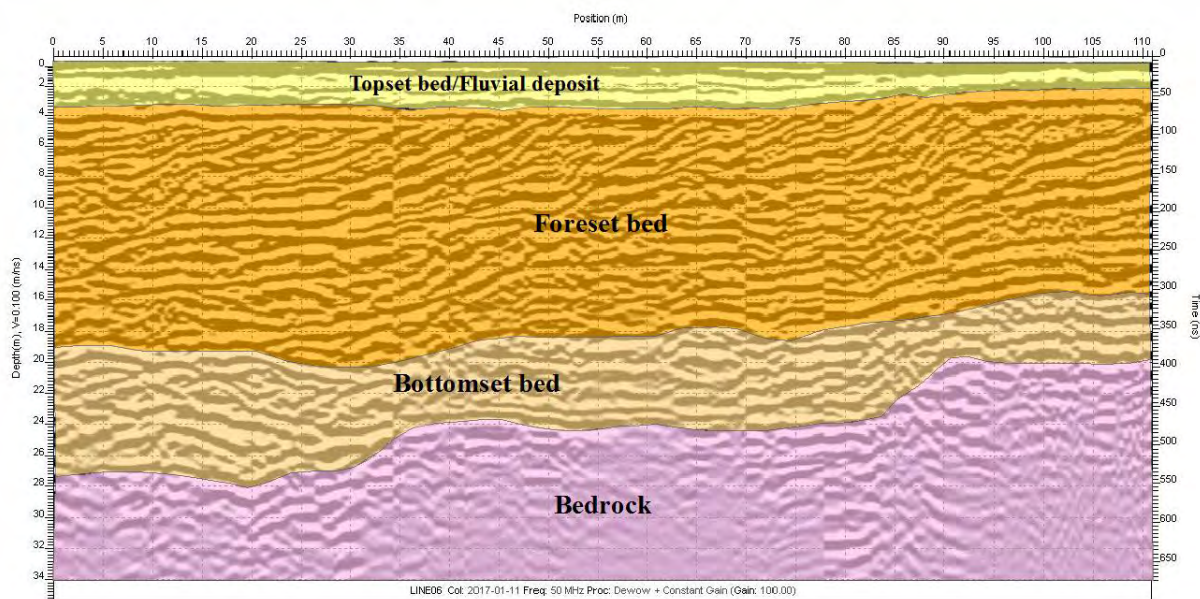

Figure 4-25. Interpreted radargram of profile 5.

Profile 5, consisting only of delta structures, could potentially be an excellent source of groundwater supply, but a probe drilling is necessary to assess the sediment composition of this aquifer. The left section (0-30 m) of the radargram seems like a good spot to perform the drilling, as it covers more depth than the right section.

The IP- and resistivity profiles revealed patterns that could indicate influence from the kettle hole on the opposite side. However, these patterns were not supported by the radargram.

4.6 Profile 6: Exposed bedrock

Profile 6 covers 120 m, and is situated in a fluvial deposit right next to the exposed bedrock at Herrefoss (figure 4-26). This is the only resistivity profile that is represented by the *wenner* configuration. The inversion process was unstable for the *gradient* configuration, hence *wenner* presented the most reliable results.
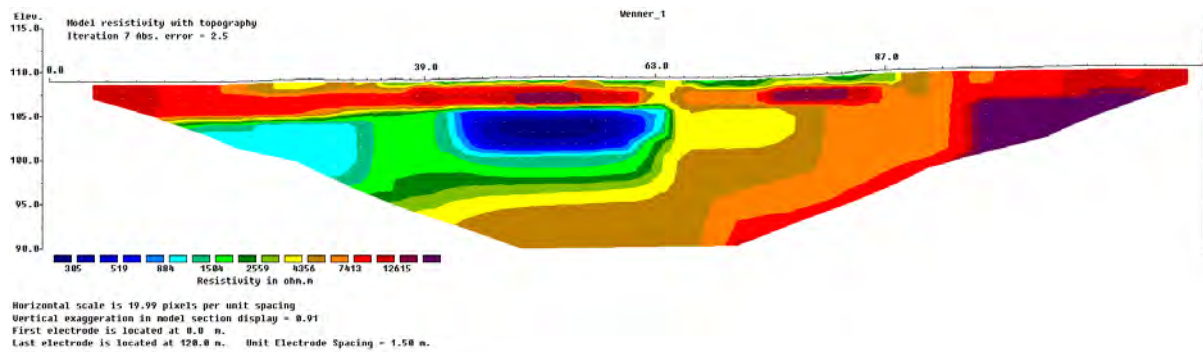

Figure 4-26. Inverted resistivity section of profile 6 (wenner).

Profile 6 clearly bears the character of being deposited in a bedrock environment. The layers seem forced to curve left at 63 m at 98 masl, which indicates a dominating presence of bedrock in the right half of the profile. The extent of the bedrock is uncertain, but there seems to be a solid purple core in the right-section with high resistivities. The decreasing resistivity-layers extending left from this core, still possess values that could correspond to bedrock (4000-7000 Ωm). Perhaps they are weathered layers of the bedrock.

Like the other profiles, profile 6 presents a red belt of high resistivities at the top section. But it is not as thick and coherent, and the resistivity values are much lower, probably due to the lower altitude. Careful consideration is essential before assuming a dry foreset bed, as this is a significantly different environment than the previous profiles. In addition, the profile runs almost perpendicular to the potential foreset bed, making it less detectable.

The lowest resistivities appears in an oval moist body at the mid-section (42-63 m). By going from approximately 12 000 Ωm at 105 masl, to 305 Ωm at 103 masl is a strong indication of moisture. The oval shape also gives the impression of a subsurface channel heading towards the reader. Probe drilling was conducted at this profile to investigate the moist body and depth to bedrock (figure 4-28)
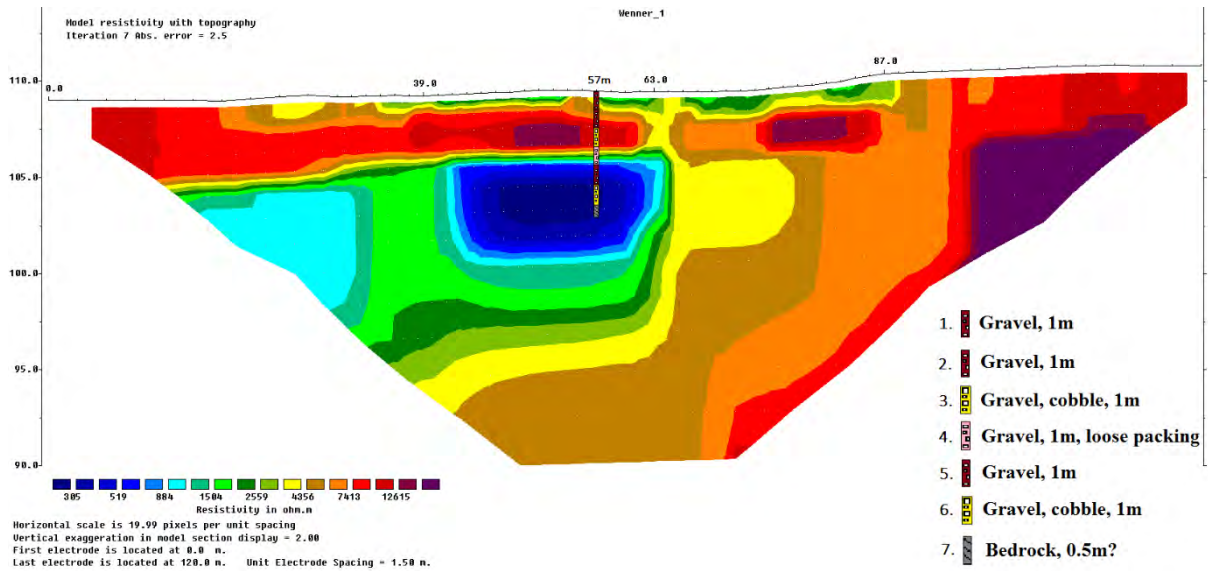
Figure 4-28. Inverted resistivity section of profile 6 with probe drilling at 57 m.

The probe-drilling hit what appeared to be bedrock in the middle of the moist body, which was sooner than expected based on the resistivity profile. What seems to have occurred, is what Solberg et al. (2011) refer to as the 3d-effect. The current has taken the path of least resistance, and spread out radially in three dimensions. This has caused the illusion of a larger moist body, and larger depth to bedrock on the resistivity profile. Based on the drilling results (table 7-7 in appendix 2), the deposit appears to be dominated by gravel. It is interesting to observe that loose packing is introduced at the point where the resistivity drops.

The radargram of profile 6 seems to support the pattern in the resistivity profile, where the bedrock appears to decline diagonally from right to left (figure 4-29). There is a significant loss of signal in the radargram, which seem to confirm bedrock domination.
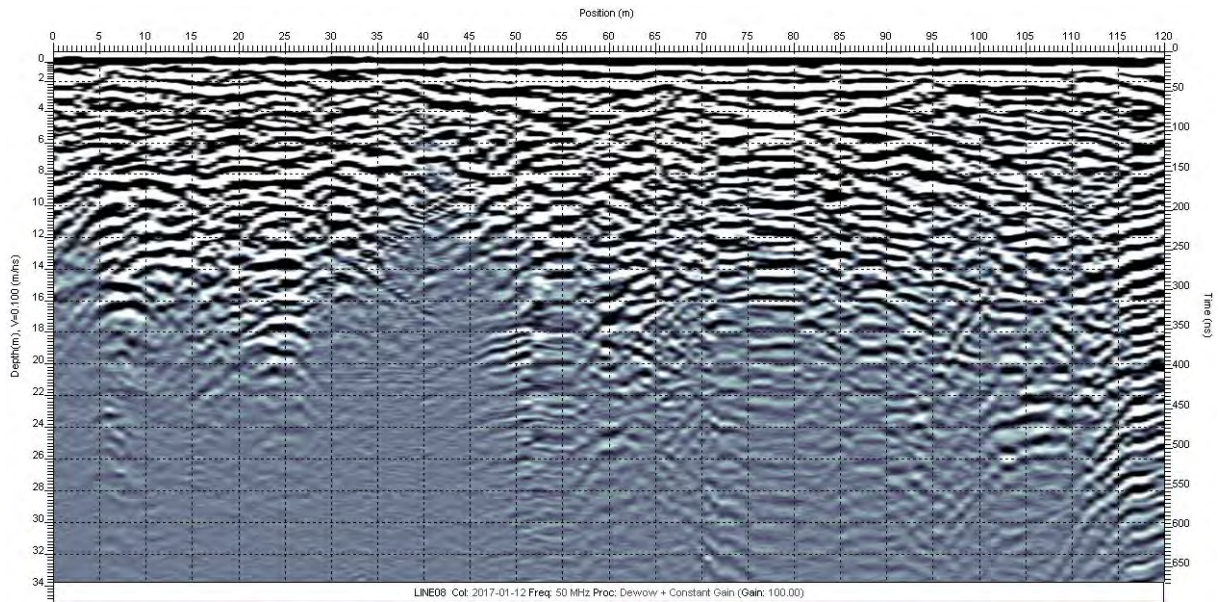
64

Figure 4-29. 50 MHz radargram of profile 6.

The reflections at the upper part appear hummocky and discontinuous, a pattern that is associated with alluvial fans with poorly bedded sand and gravel (Éckes & Hickin, 2001). Based on the probe drilling, it seems to be poorly bedded gravel and cobble in this case. Macro scale diffractions occur with increasing depth, which together with chaotic reflections can be associated with bedrock (Éckes & Hickin, 2001). Note the coherent line starting at 9 m depth, crossing the profile diagonally and ending at approximately 4 m depth at 120 m. Based on the resistivity result, this line seems to represent the bedrock surface. Annan (2003) shares a radargram where the bedrock is displayed in a comparable way (figure 4-30).
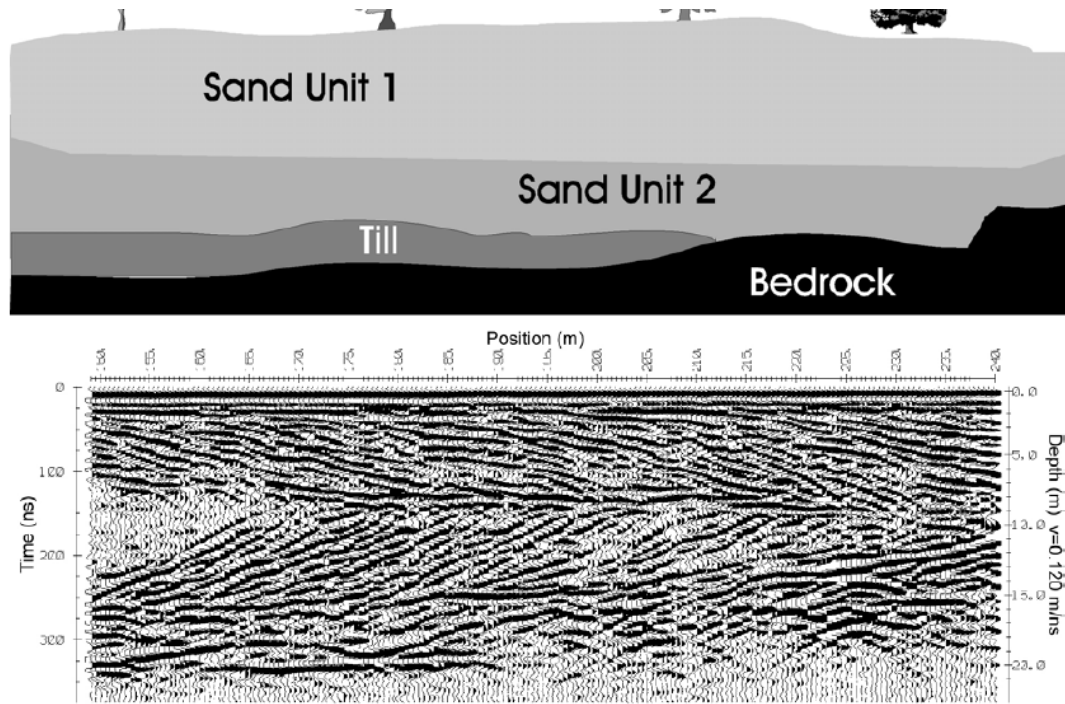
Figure 4-30. 100 MHz radargram of an area of glacial outwash deposits near Marathon, Ontario, Canada (Annan, 2003).

The bedrock is easier to distinguish in Annan's example as the layers above are bedded. Notice how the reflections below the bedrock surface are chaotic with diffractions. The radargram of profile 6 is much more chaotic overall, and without resistivity- and drilling data it would be harder to identify the bedrock.

After interpretation, it appears the probe drilling might not hit bedrock, but an impenetrable layer approximately 2 m above it (figure 4-31).
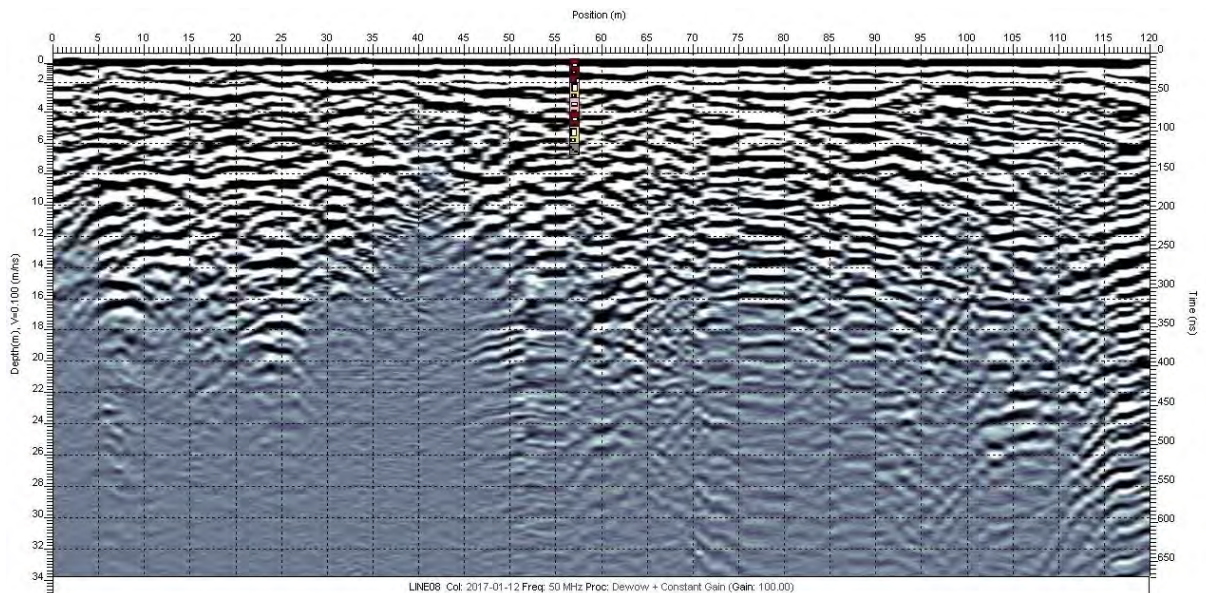
Figure 4-31. 50 MHz radargram of profile 6 with probe drilling at 57 m.

The drilling stops in a layer of diffractions, which could indicate part of the bedrock, or sediments with massive boulders (till/moraine ridge) (Beres & Haeni, 1991; Éckes & Hickin, 2001). However, the diffractions gave a velocity value of 0.146 m/ns, which does not correspond to either moraine or granite (Reynolds, 2011). It corresponds to unsaturated gravel and sand (Reynolds, 2011). Hence, a third option might be a hard-packed layer of sand and gravel.

From the results, it appears that this is an area dominated by bedrock and poorly bedded gravel and cobble (figure 4-32). Hence, it does not seem suitable for groundwater supply. However, more drillings should be made in order to verify the interpretation of the bedrock boundary.
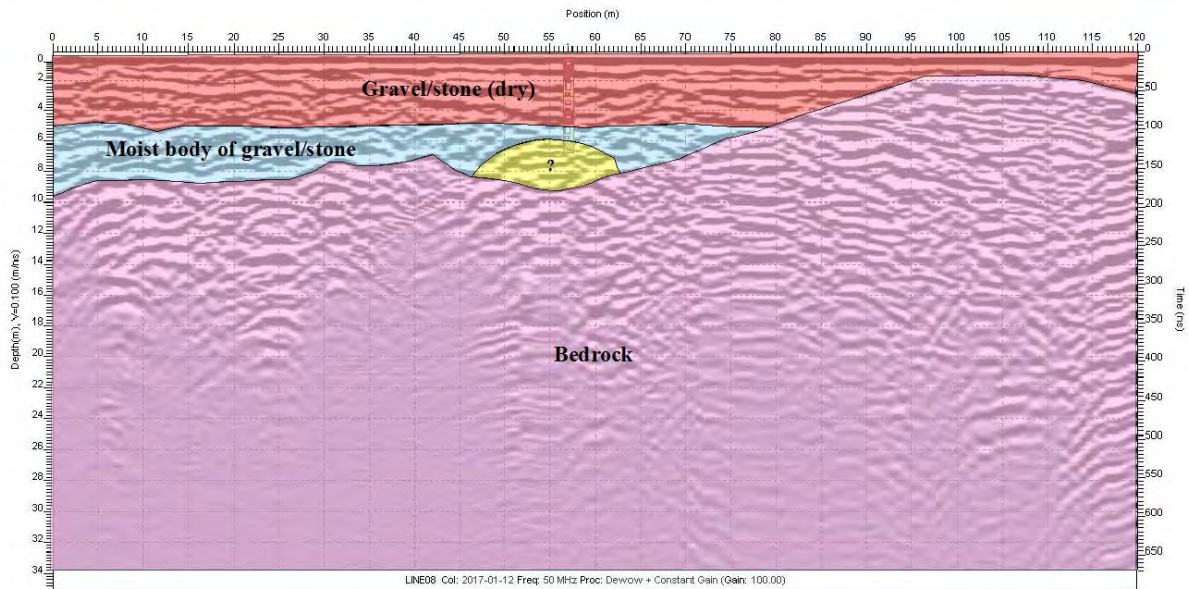
Figure 4-32. Interpreted radargram of profile 6. There is uncertainty about the layer that caused the probe drilling to stop. See table 7-13 in appendix 4 for the velocities of the relevant features

4.7 Profile 7: Bottom of the waterfall

Profile 7 is 80 m long, and is thus the resistivity profile with the highest resolution, but shortest penetration depth (figure 4-33). The profile is situated in fluvial deposits right below the water fall (Herrefoss).
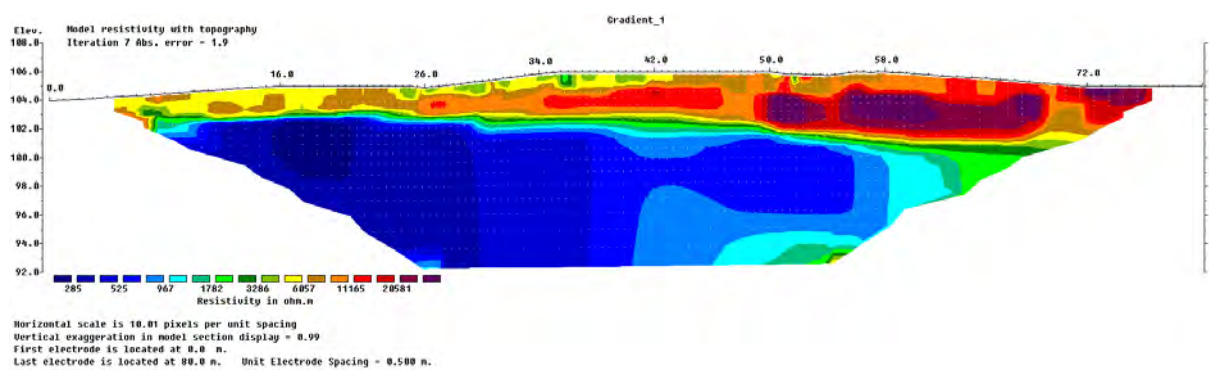

Figure 4-33. Inverted resistivity section of profile 7 (gradient).

Profile 7 looks very promising at first glance, as the bulk of the profile seems to be saturated. The water table appears to be clearly outlined with a significant resistivity contrast at

approximately 102 masl. This contrast does not follow a straight line, but decreases towards the right. It gives the impression of a confining layer covering the aquifer. The resistivity values for the saturated zone ranges from 285- to 1000 Ωm, which according to Jeppson & Dahlin (2016) is indicative of saturated sand.

The vadose zone appears divided in two parts: a low resistivity section to the left, and a high resistivity section to the right. The cause of this phenomenon is likely to be grain size as a significant contrast was observed in the field. An aggregate of boulders dominates the right section (figure 4-34), while sand and gravel dominate the left section.

Figure 4-34. The right section of profile 7. Boulders dominated this area, and it was a challenge to knock down the electrodes.

Hence, a probe drilling was conducted in the left section, as it seemed more promising in terms of water supply (figure 4-35). The drilling spot was chosen to be at 25 m, as it appeared to be a homogenous layer with low resistivity from 102 masl and below.
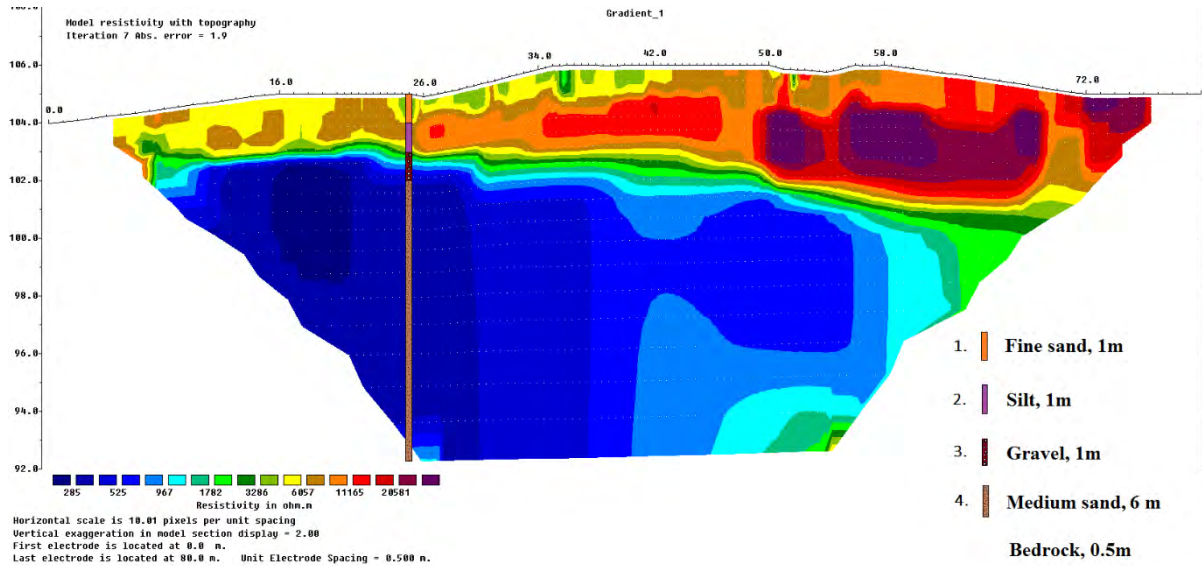
Figure 4-35. Inverted resistivity section of profile 7 with probe drilling at 25 m.

The drilling data matched the resistivity results accurately, and revealed the homogenous layer with low resistivity (300-500 Ωm) to be medium sand, just as Jeppson & Dahlin (2016) indicated. Silt occurs exactly at the contrasting layer observed in the resistivity profile, and could thus be responsible for the confining effect.

The drilling hits bedrock at 13.5 m, which is not an ideal thickness for an aquifer, but it fulfills the minimum surface casing suggested by Fetter (2001). The radargram of the profile confirms the presence of bedrock by loss of signal at approximately 13.5 m (figure 4-36).
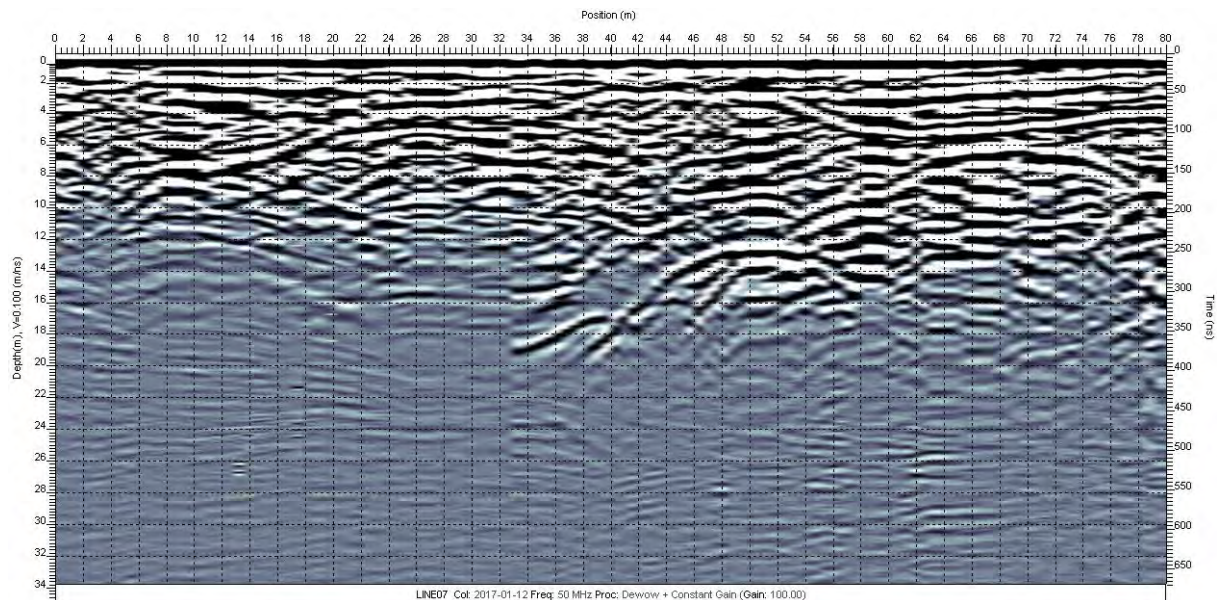
Figure 4-36. 50 MHz radargram of profile 7.

The bedrock appears to have a dominating presence in this area, as the loss of signal covers the bottom half of the radargram. Massive diffractions occur at the right half of the radargram, and they appear to stack on top of each other, creating a ridge form. Their velocity values are 0.08- and 0.085 m/ns, which corresponds to moraine (Reynolds, 2011). I.e. this could indicate a moraine ridge.

A coherent reflection appears at approximately 4 m depth at 80 m. It stretches along most of the profile and seems to represent the surface of the medium sand-layer (figure 4-37).

1. Fine sand, 1m   2. Silt, 1m   3. Gravel, 1m   4. Medium sand, 4 - 10.5m
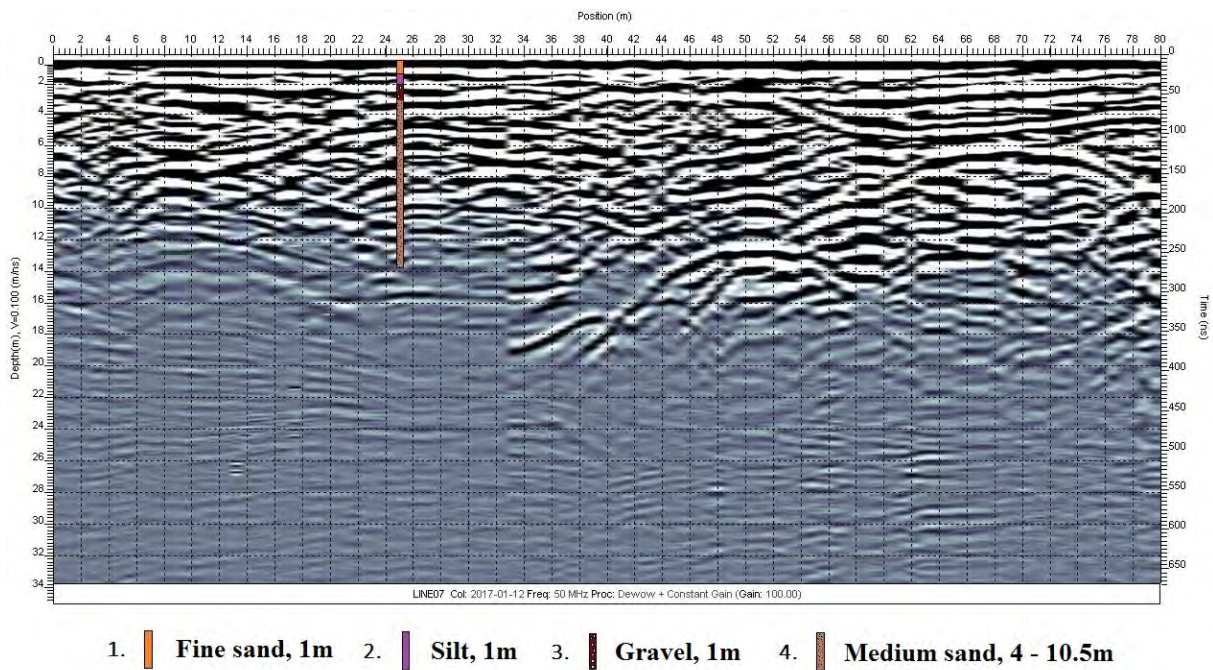
Figure 4-37. 50 MHz radargram of profile 7 with probe drilling at 25 m.

A diffraction within the medium sand-layer (50 m at 9 m depth) gives a velocity value of 0.07 m/ns, which corresponds to saturated sand (Reynolds, 2011). Hence, it seems the blue section of the resistivity profile consists mainly of saturated sand. Saturation was confirmed by the probe rods, which were soaked from 3 m depth and below. This matches the resistivity profile, and confirms a saturated layer of medium sand.

The potential confining layer of silt seems to start at 2 m depth, and extend almost horizontally until it aligns with the layer of medium sand at 37 m (figure 4-38).

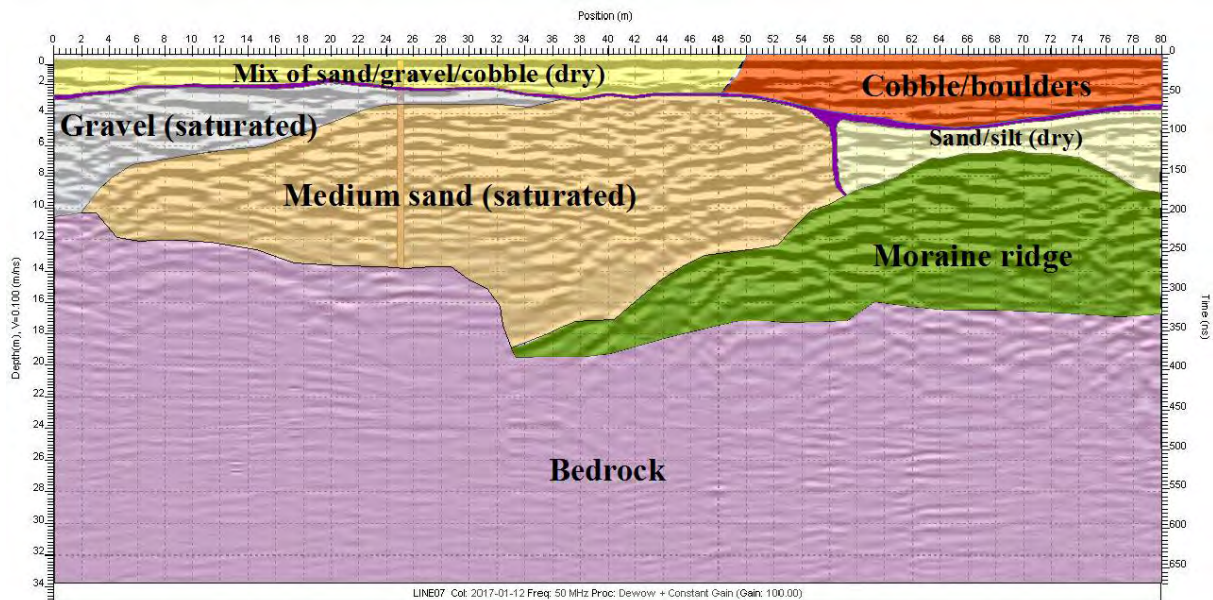*Figure 4-38. Interpreted radargram of profile 7 based on probe drilling and resistivity values. The thin purple layer represents the potential confining layer (silt). See table 7-14 in appendix 4 for the velocities of the relevant features*

The broadest diffraction (68 m at 7 m depth) gives a velocity of 0.174 m/ns, which corresponds to dry sand and dry silt. Thus, the potential confining layer should be located somewhere between 50 m (saturated sand) and 68 m.

If this is a confined aquifer, it could potentially be a sufficient location for groundwater supply. A greater thickness would be ideal, but a confining layer might make up for the lack of thickness. And besides, the aquifer does fulfill the minimum surface casing suggestion (Fetter, 2001). Medium sand possesses the highest specific yield (weight, 2008), but its hydraulic conductivity is less than for coarse sand and gravel (Fetter, 2001). Hence, a pumping test would be necessary to test the sufficiency of this potential aquifer.

5 Conclusion

Of the seven main profiles, profiles 4, 5 and 7 appeared to be potential candidates for groundwater supply. Profiles 4 and 5 had saturated zones with sections that could potentially contain sorted layers of sand and gravel. Profile 7 contained a thick saturated layer of medium sand, possibly covered by a confining layer. In addition, supplementary profile 8 also revealed a potential spot of a saturated delta foreset bed. Hence, it is a potential candidate. The rest of the profiles did not provide information that indicated sufficient subsurface conditions for groundwater supply.

This study can be improved by increasing the amount of profiles, and provide equal survey coverage for all. That would ensure a better overall interpretation of the area. Profiles 1, 2 and 3 were only covered by 2D-resistivity, which raises high uncertainty regarding the interpretation of them. Not all profiles had probe drilling data, which also add uncertainty to their interpretation.

A more accurate GPS will enhance the reliability of study locations. The inaccuracy of the Garmin Oregon 300 was 3-5 meters, which is not ideal when mapping potential spots for well placements.

The GPR profiles can be performed with more accuracy. They could have been performed by walking with a beeper-function instead of using a sled. It was difficult to keep a consistent pace when pushing the sled in challenging terrains. Topography should also have been added in the radargrams, as that would have simplified the comparison between the resistivity-profiles and the radargrams. All the profiles should also have been measured consistently from south to north in order to avoid confusion.

6 Reference list

ABEM Instrument AB. (2016). *Instruction manual. Terrameter LS* (pp. 46-49). Löfströms Allé 6A, S-172 66 Sundbyberg, Sweden.: ABEM Instrument AB.

Annan, P.A. (2009). Electromagnetic Principles of Ground Penetrating Radar. In H.M. Jol (Ed.), *Ground Penetrating Radar: Theory and Applications* (pp. 3-37). Oxford: Elsevier B.V.

Annan, P. A. (2003). Ground Penetrating Radar Principles, Procedures & Applications (pp. 278). doi:03-0003-00

Arvidson, R., & Torp, J. (2014). *User guide for ABEM terrameter for students at Høgskolen i Telemark* (pp. 12-20). Supervised assignment. Høgskolen i Telemark. Gullbringvegen 36, 3800 Bø.

Beres, M. & Haeni, F.P. (1991). Application of ground-penetrating-radar methods in hydrogeological studies. *Groundwater, 29*(3), 375-386.

Brown, G. O. (2002). Henry Darcy and the making of a law. *Water Resources Research, 38*(7). doi:Artn 110610.1029/2001wr000727

Cassidy, N.J. (2009). Electrical and magnetic properties of rocks, soils and fluids. In H.M. Jol (Ed.), *Ground Penetrating Radar: Theory and Applications* (pp. 3-37). Oxford: Elsevier B.V.

Éckes, C. & Hickin, E. J., (2001). Ground penetrating radar facies of the paraglacial Cheekye Fan, southwestern British Columbia, Canada. *Sedimentary Geology, 143*, 199 - 217.

Fetter, C. W. (2001). *Applied hydrogeology* (4th ed.). Upper Saddle River, N.J.: Prentice Hall.

From, J. (2010). *Kommunal teknikk* (4th ed.). St. Olavs plass, 0130 Oslo: Gyldendal Norsk Forlag AS.

Jansen, I. J. (1983). *Detaljkartlegging av sand- og grusressurser i Bø kommune, Telemark*. 3701 Skien: Miljøverndepertementet

Jørgensen, P., Sørensen, R. and Haldorsen, S. (2014). *Kvartær geologi.* 5068 Bergen: Fagbokforlaget Vigmostad & Bjørke AS.

Jeppsson, H., and Dahlin, T. (2016). *Geoelektriska metoder inom tillämpad geofysik*. Educational compendium. Geologiska institutionen. Lund, Sweden.

Klempe, H. (2011). *Grunnvannsforsyning til Bø kommune. Pumpeforsøk av ny brønn.* Hallvard Eikas plass, 3800 Bø I Telemark: Høgskolen i Telemark

Koziel, J., Mauring, E., Lauritzen, T., Rønning, J. S., & Tønnesen, J. F. (1995). *Målinger med georadar. Teori, anvendelse, teknikker og eksempler på opptak*. 7002 Trondheim: NGU

Larsen, B. E., Tønnesen, J. F. and Olsen, L. (2015). *GPR-undersøkelser ved Storås og Meldal, Meldal kommune, Sør-Trøndelag*. 7491 Trondheim: NGU

Loke, M. H. (2015). *2-D and 3-D ERT surveys and data interpretation*. Paper presented at the Piedmont Regional Order of Geologists, Pacific Hotel Fortino, Torino, Italy.

Loke, M. H. (2011). Electrical resistivity surveys and data interpretation. *Encyclopedia of Earth Sciences Series*, 46, pp. *276-283*. Doi: 10.1007/978-90-481-8702-7_46

Palacky, G.J. (1987). Resistivity characteristics of geological targets. In M. N. Nabighian (Ed.), Electromagnetic *Methods in Applied Geophysics: Theory* (pp. 53- 125). Tulsa: Society of Exploration Geophysicists.

Reynolds, J. M. (2011). *An introduction to applied and environmental geophysics* (2nd ed.). Chichester, West Sussex; Malden, Mass.: Wiley-Blackwell.

Sutphin, D. M., Drew, L. J., Fowler, B. K. and Goldsmith, R. (2002). *Techniques for assessing sand and gravel resources in glaciofluvial deposits-An example using the surficial geologic map of the Loudon quadrangle, Merrimack and Belknap counties, New Hampshire*. (U.S. Geological Survey Professional Paper 1627).
Retrived from https://pubs.usgs.gov/pp/p1627/p1627-tag.pdf

Solberg, I.-L., Hansen, L., Rønning, J. S., & Dalsegg, E. (2011). *Veileder for bruk av resistivitetsmålinger i potensielle kvikkleireområder*. 7491 Trondheim: NGU

Telford, W. M., Geldart, L. P., & Sheriff, R. E. (1990). *Applied geophysics* (2nd ed.). Cambridge England; New York: Cambridge University Press

Weight, W. D. (2008). *Hydrogeology field manual* (2nd ed.). New York: McGraw-Hill

7   Appendix

7.1 Appendix 1: GPR configurations

Table 7-1. Settings for GPR system parameters with 50 MHz antennas.

Antenna Frequency	50 MHz
Time Window	780.8 ns
	35.12 m
Sampling Interval	1.6 ns
Antenna Separation	2 m
Antenna Step Size	0.5 m
Radar Velocity	0.1 m/ns
System Stacking	32
Pulser Setting	PE100 400

Table 7-2. Settings for acquisition control with 50 MHz antennas.

Trigger Method	Free run
Beepet Activated	None
GPS Parameter Menu	
Odometer Setup Menu	
Fibre Optic Testing	
Free Run Tracedelay	0 s
Free Run Start Tracedelay	3 s
Free Run Pause Trace	None

Table 7-3. Settings for GPR system parameters with 100 MHz antennas.

Antenna Frequency	100 MHz
Time Window	420 ns
	18.89 m
Sampling Interval	0.8 ns
Antenna Separation	1 m
Antenna Step Size	0.250 m
Radar Velocity	0.1 m/ns
System Stacking	8
Pulser Setting	PE100 400

Table 7-4. Settings for acquisition control with 100 MHz antennas.

Trigger Method	Odometer
Beepet Activated	None
GPS Parameter Menu	
Odometer Setup Menu	
Fibre Optic Testing	
Free Run Tracedelay	0 s
Free Run Start Tracedelay	0 s
Free Run Pause Trace	None

Table 7-5. Settings for GPR survey parameters with 50 MHz antennas. With 100 MHz antennas, the Antenna Step Size is adjusted to 0.25 m.

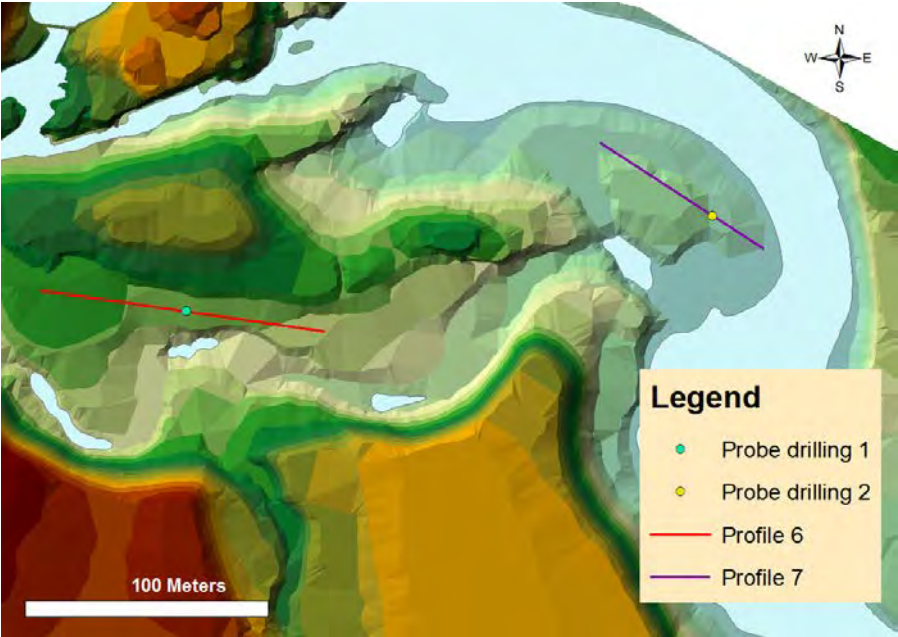| Start Position	0 m
Antenna Step Size	0.5 m
Positional Units	metres
Data Directory Number	17
Survey Type	Reflection
GPR Grid Type	X only
X Line Spacing	1 m
Y Line Spacing	N/A

7.2 Appendix 2: Probe drilling data

Figure 7-1. Probe drillings conducted by the author at profiles 6 and 7.

Table 7-6. Coordinates for probe drillings 1 and 2.

Probe drilling	Coordinate
1	32V 493077 6587433 UTM
2	32V 493293 6587473 UTM

Table 7-7. Recorded probe drilling information on profile 6.

Profile 6 – probe drilling (01.03.2017)			
Depth (m)	**Time** (min)	**Deposit**	**Comment**
0 - 1 m	3:55	Gravel	Frost
1 - 2 m	1:28	Gravel	
2 - 3 m	0:25	Gravel/cobble	
3 - 4 m	0:15	Gravel (LP)	
4 - 5 m	0:58	Gravel	Stopped slightly, then it went quick
5 - 6 m	0:40	cobble/gravel	
6 - 6.5 m	Bedrock		

Table 7-8. Recorded probe drilling information on profile 7.

Profile 7 – probe drilling (01.03.2017)			
Depth (m)	**Time** (min)	**Deposit**	**Comment**
0 - 1 m	1:14	Fine sand	Frost
1 - 2 m	0:07	Silt	
2 - 3 m	0:38	Gravel	Slight stop at 2.5 m
3 - 4 m	0:24	Medium sand	
4 - 5 m	0:30	Medium sand	
5 - 6 m	0:26	Medium sand	
6 - 7 m	0:33	Medium sand	
7 - 8 m	0:27	Medium sand	
8 - 9 m	0:56	Medium sand	Weak engine
9 - 10 m	0:34	Medium sand	
10 - 11 m	0:33	Medium sand	
11 - 12 m	0:22	Medium sand	
12 - 13 m	0:29	Medium sand	
13 - 13.5 m	Bedrock		

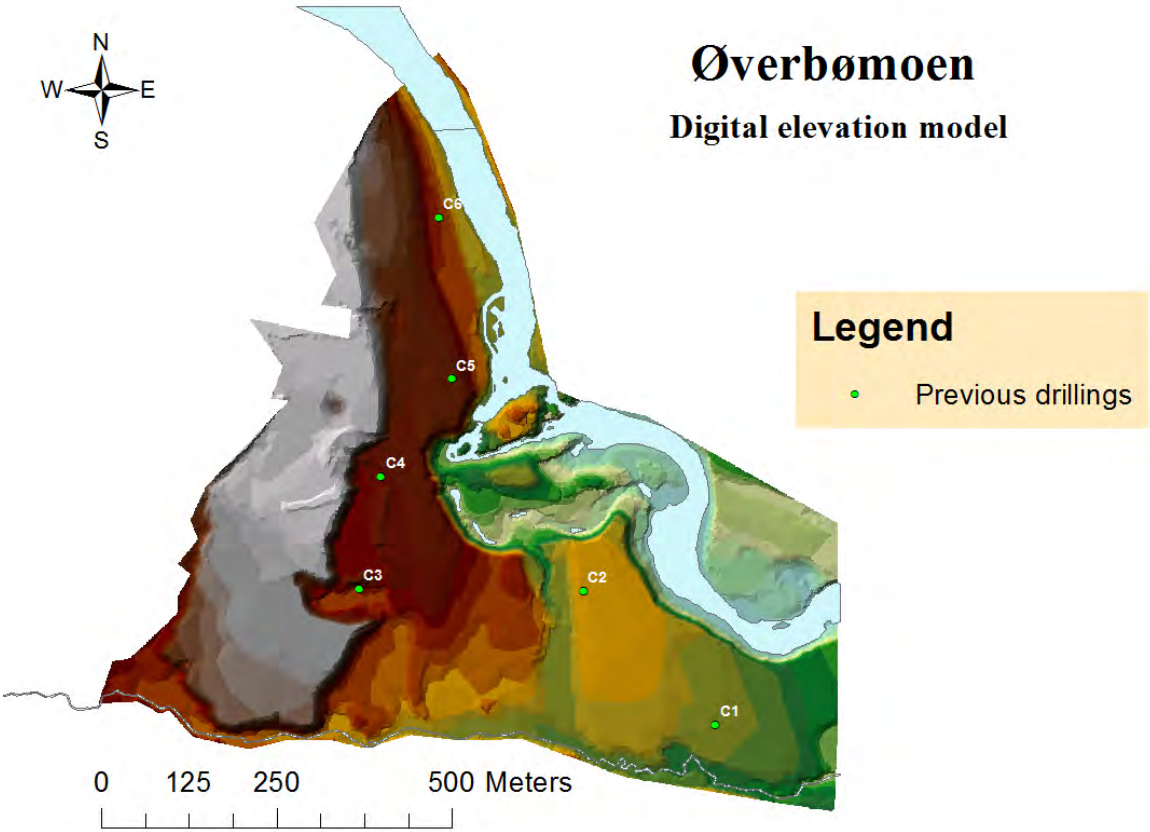## 7.3 Appendix 3: Previous drillings and excavations at Øverbømoen

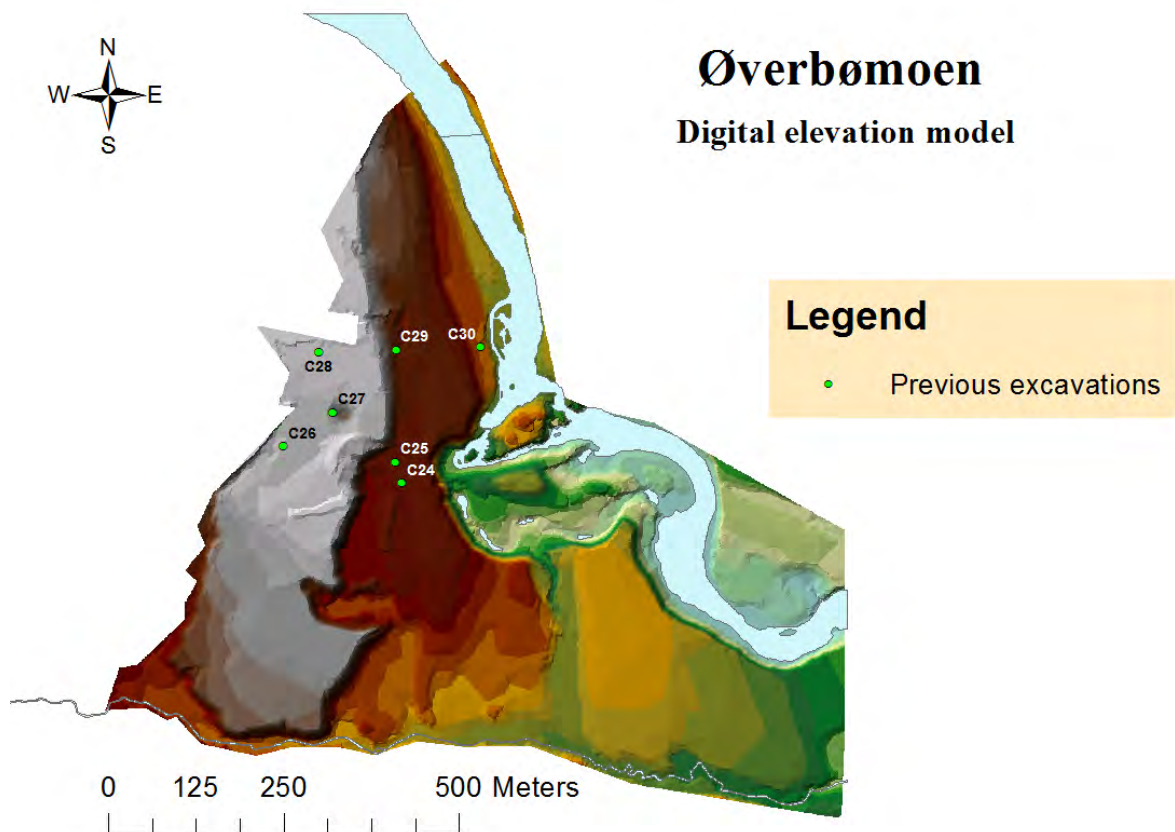*Figure 7-2. Previous drillings at Øverbømoen (Jansen, 1983).*

Figure 7-3. Previous excavations at Øverbømoen (Jansen, 1983).

Legend explanations for <u>drilling profiles</u>:

S = probe drilling.   U = survey drilling

F = bedrock, B = boulder, St = cobble, G = gravel, S = sand, Si = silt, L = clay

f = fine (Sf = fine sand), g = coarse (Sg = coarse sand),

lp = loose packing, hp = hard packing

Table 7-9. Previous drilling profiles at Øverbømoen (Jansen, 1983). The ground surface in this table differs slightly from the ground surface in the DEM.

Drilling nr	NGO-coordinates		S/U	Date	Ground surface. M.a.s.l.	Profile	Soil depth in m
	Y	X					
C 6	+27870	159190	s	10.1975	120	G, Sg, St, 2/ G, Sg, 1/ S, 1/ St, G, Sg, 6/ Sf, 1/ St, G, 7/ St, hp	>18
C 5	+27890	158960	s	11.1979	124	G, St, 2/ S, G, St ,1/ S, 1/ S, G, 3/ S, St, 4/ St, 0.4/ S, St, 7.6, hp/ St, hp	>19
C 4	+27790	158820	s	10.1979	125	St, G, 0.8, hp/ S, 1/ S,G,0.3/ S, 0.8/ S, St, 1.6/ F	4,5
C 3	+27760	158660	s	10.1979	123	Sg, G, 1/ Sg;G, St, 2/ Sg, G, 8/ S, G, Si, 17.2/ F	28,2
C 2	+28080	158660	s	10.1979	117	St, G, 1.7, hp/ S, St, 0.3, hp/ S, (Si), 4/ F	6
C 1	+28270	158470	s	10.1979	116	St, G, 1/ Si, L, Sf, 2	>3

Legend explanations for <u>digging profiles</u>:

In terms of soil/drainage:

H = high humic content

J = high iron content

D = well drained

F = boggy/poorly drained

Depth of sample is given in brackets under "samples".

Table 7-10. Previous digging profiles at Øverbømoen (Jansen 1983).

Profile nr	NGO-coordinates Y	NGO-coordinates X	Soil/ drainage	Samples (depth in m)	Profile	Soil depth in m
C 30	+27920	159015		C.30.1 (3)	G, S, St (large), 3 - medium well sorted	>3
C 29	+27800	159010		C.29.1 (2.5)	G, S, Si, St, 2.5 (15% silt content)	>2.5
C 28	+27690	159005	J, D	C.28.1 (2)	G, S (sorted layers), 2.5/ Sf, Si, 0.3	>2.8
C 27	+27710	158920	J, D	C.27.1 (3.2)	G, S, St, 3.12 – Well sorted	>3.2
C 26	+27640	158870	H, F	C.26.1 (2.2)	G, S, St (large), 2.2	>2.2
C 25	+27800	158850	J, D	C.25.1 (3)	S, Sg, 3 – Well sorted	>3
C 24	+27810	158820	D	C.24.1 (2)	G, S, St, 2	>2

7.4 Appendix 4: Velocities connected to the GPR interpretations.

Table 7-11. Velocities connected to features in Profile 8 (figure 4-5)

Feature	Velocity (m/ns) (hyperbola/diffractions)
Till	0.09, 0.107, 0.113, 0.118 and 0.120
Fracture (saturated)	0.031 and 0.034
Fracture (saturated sand)	0.054
Esker	0.127

Table 7-12. Velocities connected to features in Profile 4 (Figure 4-20)

Feature	Velocity (m/ns) (hyperbola/diffractions)
Ridge structures	0.081 and 0.107

Table 7-13. Velocities connected to features in Profile 6 (figure 4-32)

Feature	Velocity (m/ns) (hyperbola/diffractions)
?	0.146 (sand & gravel)
Bedrock (granitic gneiss)	0.077 and 0.089

Table 7-14. Velocities connected to features in Profile 7 (Figure 4-38)

Feature	Velocity (m/ns) (hyperbola/diffractions)
Moraine ridge	0.085 and 0.080
Sand/silt (dry)	0.174
Medium sand (saturated)	0.070

7.5 Appendix 5: GPR coverage of profile 4 and 5

GPR profiles 4 and 5 did not cover the entire resistivity profiles due to terrain difficulties (figure 7-4).
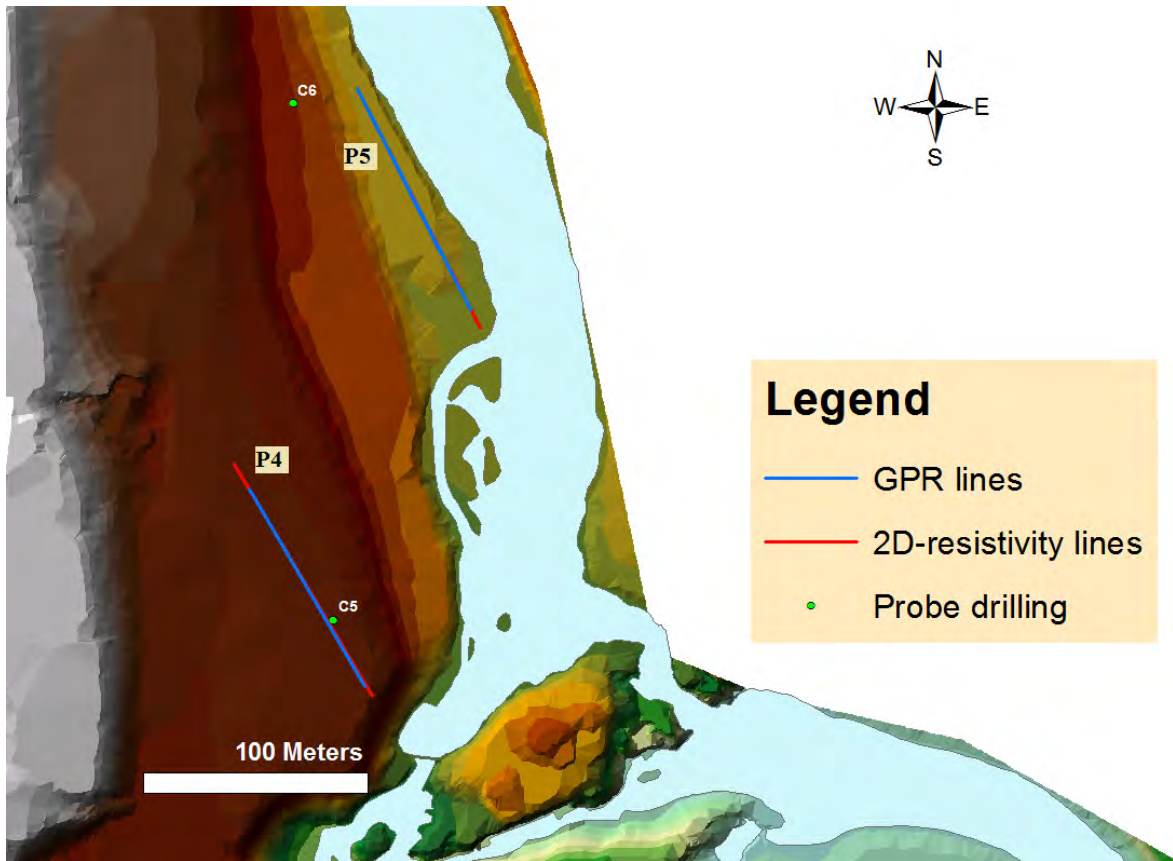
Figure 7-4. The extent of GPR coverage over resistivity profiles 4 and 5.

Table 7-15. GPS coordinates for GPR lines for profile 4 and 5.

Profile	Start point	End point
4	32V 492946 6587670 UTM	32V 492997 6587582 UTM
5	32V 493044 6587750 UTM	32V 492994 6587848 UTM

7.6 Appendix 6: Wenner profiles

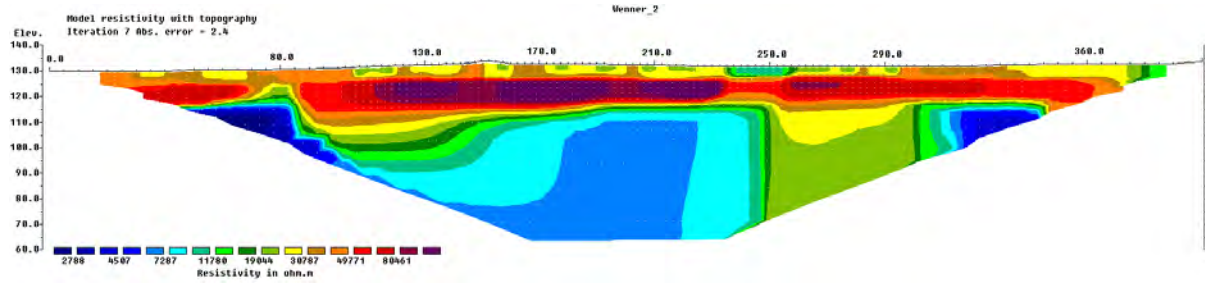Remark: Profile 6 shows *gradient* configuration, as the *wenner* profile was presented in the thesis.

Figure 7-5. Profile 1 presented by the wenner configuration.
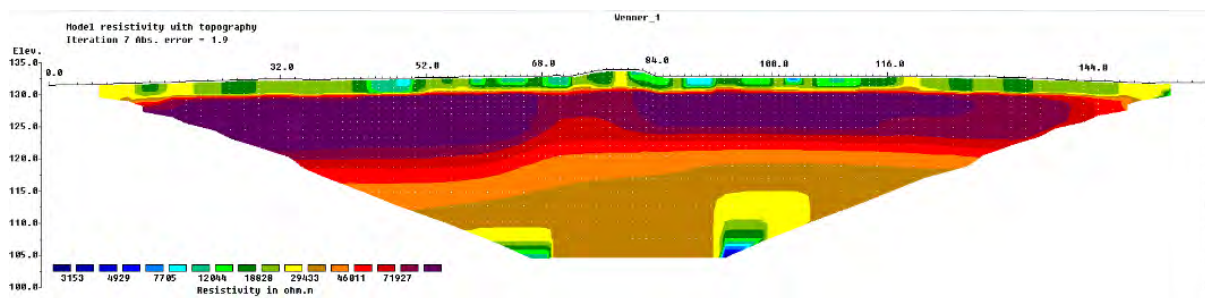
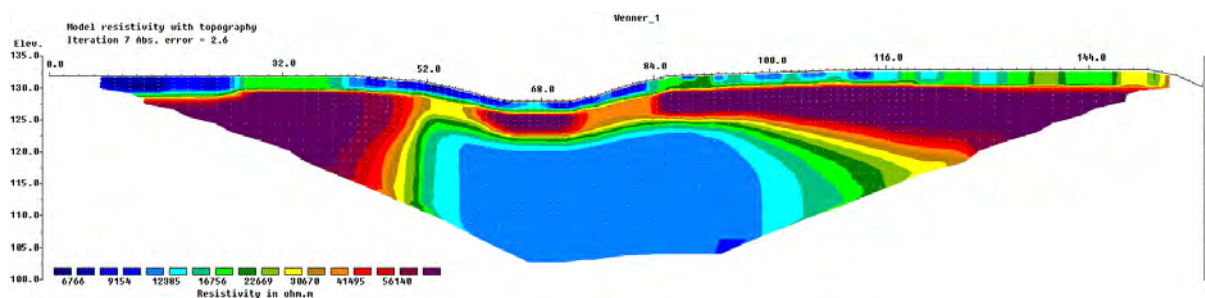*Figure 7-6. Profile 2 presented by the wenner configuration.*

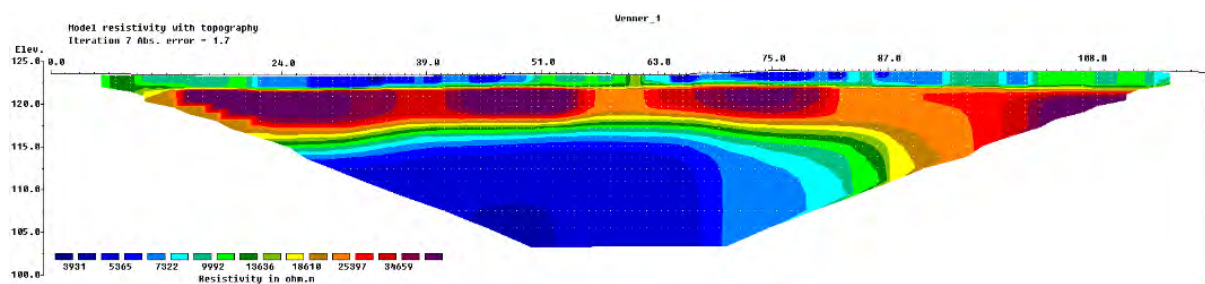
Figure 7-7. Profile 3 presented by the wenner configuration.

Figure 7-8. Profile 4 presented by the wenner configuration.
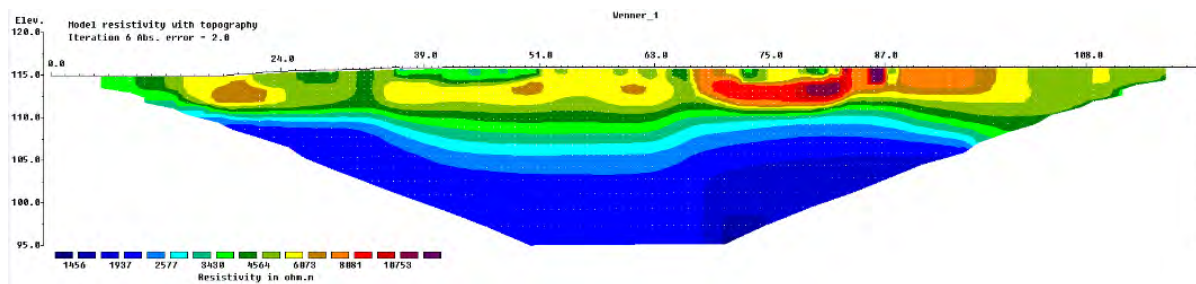

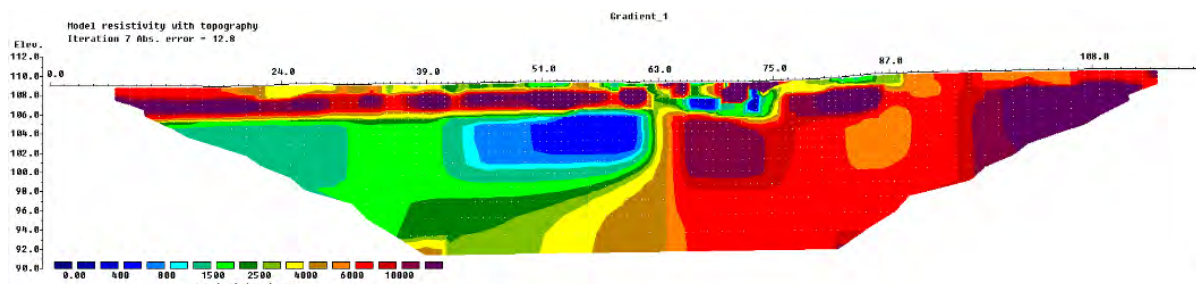*Figure 7-9. Profile 5 presented by the wenner configuration.*

Figure 7-10. Profile 6 presented by the gradient configuration.
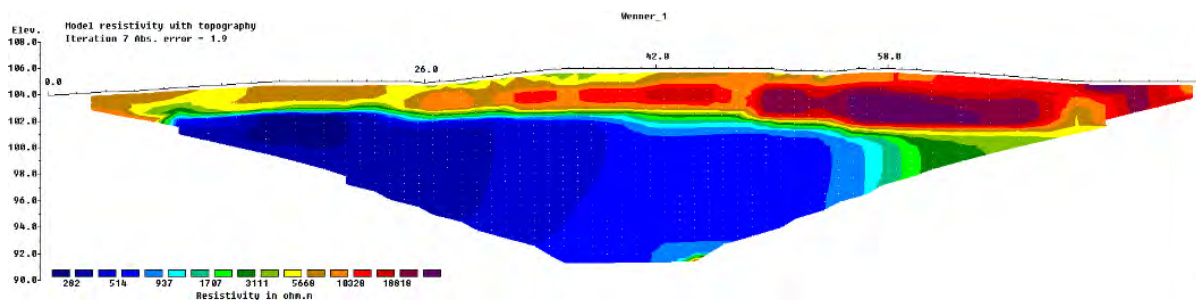

Figure 7-11. Profile 7 presented by the wenner configuration.

7.7 Appendix 7: Grain size scale

This thesis used a translated Wentworth scale collected from Norges Geologiske Undersøkelse (NGU) when describing sediments.

Table 7-16. The Wentworth scale used in this thesis.

Grain size scale

Navn (norsk)	Name (english)	Diameter (mm)
Leir	Clay	<0,002
Silt	Silt	0,002 - 0,063
Sand	Sand	0,063 - 2,0
Grus	Gravel	2,0 - 64
Stein	Cobble	64 - 256
Blokk	Boulder	>256

NGU. (n.d.). Classification of sediments based on grain size composition (Folk, 1954, modified). Retrieved May 13, 2017, from http://www.ngu.no/Mareano/Grainsize.html